63-3-3

RADC-TDR-63-1, Vol. I

School of Electrical Engineering
CORNELL UNIVERSITY
Ithaca, New York

RESEARCH REPORT EE 555

THEORETICAL AND EXPERIMENTAL INVESTIGATION OF LINEAR BEAM MICROWAVE TUBES

Final Report, Vol. I

1 October 1961 to 30 September 1962

Approved by

G. Conrad Dalman
Lester F. Eastman
Paul R. McIsaac

Griffiss Air Force Base, New York
Rome Air Development Center, Air Research and Development Command
Prepared under Contract No. AF30(602)-2573

ASTIA Notice

Qualified requestors may obtain copies of this report from the ASTIA Document Service Center, Dayton 2, Ohio. ASTIA Services for the Department of Defense contractors are available through the "Field of Interest Register" on a "need-to-know" certified by the cognizant military agency of their project or contract.

RADC-TDR-63-1, Vol. I

74

School of Electrical Engineering
CORNELL UNIVERSITY
Ithaca, New York

RESEARCH REPORT EE 555

THEORETICAL AND EXPERIMENTAL INVESTIGATION OF LINEAR-BEAM MICROWAVE TUBES

Final Report, Vol. I 1 October 1961 to 30 September 1962

Approved by

G. Conrad Dalman
Lester F. Eastman
Paul R. McIsaac

Prepared under
Contract No. AF30(602)-2573, Project No. 5573, Task No. 557303
Rome Air Development Center, Air Research and Development Command
Griffiss Air Force Base, New York

CONTENTS OF FINAL REPORT

ABSTRACT

In the study of beam-circuit interaction, a description is given of the radio-frequency current distributions in a Brillouin-focused electron beam that has been velocity modulated by a gridless-gap cavity. Results of small- and large-signal experiments are given and small-signal theory is reviewed. A trapezoidal approximation to the beam profile is shown to agree with the beam behavior. Large-signal results showed average beam defocusing and focusing effects as well as harmonic currents. The plasma-frequency reduction factors for the wave components of the fundamental and the harmonic current were found to agree extremely well with those computed from small-signal theory.

An investigation of the laminarity of electron flow in the unmodulated beam from the STL-100 electron gun provided insight into the behavior of a medium-power Brillouin beam and served as a basis for interpreting the r-f results obtained. It was shown that the beam can display a high degree of laminarity at a beam voltage of 5000 v. The trajectory equation of the outer edge electron in the laminar model of the beam was linearized and shown to give results in good agreement with the experimental observations near Brillouin flow. In particular, it was shown that the beam may be focused at the calculated Brillouin field within the limits of experimental error. The differences between the theoretical predictions and the experimental observations are discussed, and the effects of thermal velocities, particularly at low beam voltages, are considered.

The effect of ion neutralization in the electron beam used for the

experimental studies with the beam analyzer are reported. The creation of positive ions in the beam partially neutralized the space-charge forces. This caused the current density on the beam axis to increase during the pulse and caused the edge of the beam to move inward toward the axis. The presence of icns in the beam also increased the degree of nonlaminarity of flow.

Equations are derived in which the effects of relativistic velocities are accounted for in high-voltage diodes and klystron gaps. The computations made are limited to a maximum value of 211 kv beam voltage. Beam loading and beam detuning are gradually lowered as the velocity of the electron beam becomes relativistic.

This report discusses an experimental and theoretical investigation into the possibility of obtaining an increase in efficiency by applying power to the middle cavity of a three-cavity klystron. The experimental work was performed upon a Sperry SAS-61 S-band pulsed klystron. This work indicates that, within the limits imposed by the tube used, no increase in efficiency can be obtained by middle-cavity drive that could not be obtained equally well by optimum uptuning of the middle cavity of the klystron.

Equipment has been developed for quickly measuring the fringing (interaction) fields in linear beam circuits.

An analysis has been formulated for a klystron system consisting of two drift spaces and three gaps. The dirst drift space and the first two gaps serve as a two-cavity klystron, and the final drift space and gap serve as a velocity filter. Solutions to the resulting equations have been obtained on a Burroughs Datatron 220 digital computer.

A new approach to the reduction of harmonically related spurious

outputs of high-power klystrons is studied. The approach used is to control the design of the output cavity of a klystron amplifier so as to retain the desired fundamental frequency while the higher-order resonances are spaced between the harmonic frequencies.

INTRODUCTION

The broad objective of this research project was to investigate both experimentally and theoretically, factors that are important in determining the performance capabilities of high-power linear beam microwave tubes and to find means of improving the performance of such tubes. The specific tasks were to consist of basic studies of beam-circuit interaction (including electron beams and interaction circuits), response of microwave tubes to nanosecond pulses, velocity filtering of spent beams using a-c electric fields, and the suppression of harmonic spurious outputs.

This final report consists of a collection and discussion of five technical reports and four interim reports, which have been issued as part of the contract in the year from September 30, 1961 to September 30, 1962. In the section following, brief discussions of the work of the reports are given. These are followed by conclusions for the work completed on the contract during the past year.

DISCUSSION

A. BEAM-CIRCUIT INTERACTION STUDIES

One of the most important aspects of linear beam microwave tube performance is the interaction between the electron beam and the coupling circuits. It is the objective of the present study to establish the effects of interaction that limit this harnessing of the electron beam and to extend the investigation to means of reducing these limiting effects.

A carefully developed experimental research program has been undertaken to study, understand, and improve the interaction in linear beam tubes. Experimental studies have been emphasized this past year in order that experimental methods in the laboratory might match the extensive theory at this laboratory and elsewhere, and so allow testing of these theories.

1. Beam-Circuit Test Vehicle

The keystone of this experimental research program was the development of a precision, demountable, beam-circuit-interaction test vehicle, which was reported by this laboratory in earlier reports.* The test vehical was developed by perfecting and establishing the reliability of each component or technique in a step-by-step process. A separately pumped gun with a vacuum ball valve between the gun and the drift region was constructed

---

*1. A. S. Gilmour, Jr., "A Beam Tester for Studying the Characteristics of D-C and Velocity-modulated Electron Beams," Res. Rep. EE 495, (May 1961).

2. A. S. Gilmour, Jr., "The Velocity Distribution in a Velocity-Modulated Electron Beam from a Shielded Pierce Gun," Res. Rep. EE 507, (August 1961).

to allow safe maintenance or storage of the gun at a pressure of 10^{-9} mm Hg between experiments with the test vehicle. As a result, the rest of the test vehicle could be demounted and altered without changing the performance of the gun. The beam generated by the gun was perfected so that ultimately it gave a beam of perveance 1×10^{-6} with 1 – 10 kw of pulsed beam power for use in interaction studies up to S-band frequencies. The final state of the beam was documented by making rapid scanning measurements of the current density and longitudinal velocity of the electron beam. The perfected beam was virtually guaranteed by the separate vacuum system and sealing technique and could easily be checked by the rapid-scanning device.

Previously, the measurements that could be made were (1) the d-c current density at any position in the beam and (2) the peak velocity at any position in the beam, either the d-c velocity alone or the a-c velocity superimposed on the d-c velocity. These measurements were reported in previous reports. During this past year, equipment was developed to make scanned measurements of the a-c current density. This made it possible to measure a-c current density and other effects as a function of the drive parameter throughout the beam. This experimental study is reported in Research Report EE 546 (A. S. Gilmour, Jr. and L. F. Eastman, "The Current Distributions in a Velocity-modulated, Brillouin-focused Electron Beam"). In the Brillouin beam case considered, the fundamental a-c current density was predominantly an a-c beam surface current that showed good space-charge-wave behavior. As the drive parameter was increased, nonlinear effects in the a-c current density were clearly traced, and the average spreading and contracting of the beam was traced simultaneously.

The beam-scanning equipment developed this past year was constructed so as to measure the a-c current density with a nonresonant circuit configuration, allowing for harmonic a-c current-density measurements in the beam also. These measurements of the density of the harmonic current showed a predominant beam surface current in each case. They also showed irregular variations with axial position caused by the beating of a wave launched by the localized nonlinear cavity drive and a wave driven by the distributed nonlinear beam drive.

The experimental results establish a reliable foundation for study of the harnessing of perfected power-perveance electron beams in a klystron configuration. This information gives many direct clues for better beam formation, maintenance, and modulation, as well as for methods of extending the knowledge of linear beam microwave tubes and improving their performance.

In addition to the interaction study, work has continued on the formation of an electron beam. Research Report EE 539 (D. D. Hallock, "An Investigation of the Laminarity of Flow in a Magnetically Confined Electron Beam") reports the results of an investigation of laminarity in the power-perveance beam used for interaction studies in this laboratory. This study resulted in a better understanding of the beam as well as means of perfecting the beam further. The effects of beam-generated ions on the performance of this pulsed Brillouin beam were also noted and are presented in Research Report EE 545 (A. S. Gilmour, Jr. and D. D. Hallock, "Ion Effects in a Brillouin Beam"). The effects for the beam-current density used in this study appeared to be small for pulse lengths of 10 microseconds or less, if the pressures were less than 1×10^{-7} mm Hg.

2. Circuit Tester

For both theoretical and experimental studies of interaction between electron beams and microwave circuits, an accurate and detailed knowledge is needed of the electromagnetic fields that may be present in the microwave circuit. For a few simple geometries, the fields can be calculated analytically, but in most of the cases of interest, the geometry is such as to make the analytical determination of the electromagnetic fields (even using high-speed computers) too costly. The experimental determination of the fields can be performed much more efficiently and with more flexibility.

The most attractive method of exploring electromagnetic fields in microwave structures is to use the perturbation technique for resonant structures. This relates the fractional change in resonant frequency of a cavity, $\Delta f/f_o$, caused by a perturbing bead to the ratio of the square of the electric field (at the bead location) to the total stored energy in the cavity, E^2/W. By using suitably shaped perturbing beads and orienting them in space, the electric field components may be measured in various directions.

This technique has been used to build apparatus for measuring the electric field in a resonant microwave structure as a function of bead position. This equipment provides recorder plots of E^2/W versus bead location within the structure. The electric field pattern can therefore be determined at a glance, and by proper calibration, the electric-field magnitudes desired can be read off the plots. The apparatus has been used in the frequency range from 500 Mc/s to 4000 Mc/s, but with appropriate signal sources, it could be used at both lower and higher frequencies.

3. Multiple Drive of a Klystron

Research Report EE 544 (D. Reynolds, "Investigation of the Effects of Driving the Middle Cavity of a Three-Cavity Klystron") is a report on a program which investigated the possible improvement in efficiency of a three-cavity klystron resulting from the applications of drive power to the middle cavity. The tube under test was an SAS-61 klystron. Measurements were made of the output power as a function of first-cavity drive power for a middle-cavity drive power of zero, one kilowatt in the most favorable phase, and one kilowatt in the most unfavorable phase with middle-cavity tuning as a parameter.

4. Gap Interaction with Relativistic Electron Beam

The operating voltage of modern pulsed high-power linear beam microwave tubes is so high that relativistic effects occur. It is necessary, therefore, to investigate the changes in the behavior of electron beams as the operating voltage rises, in particular, the beam-loading and beam-detuning effects with the beam electrons moving at relativistic velocities. In Research Report EE 525 (C. Sun, "A Relativistic Study of the Llewellyn Electronic Gap and Its Applications"), the detailed relativistic beam admittance presented at a gap have been analyzed from a space-charge-wave approach. The conductance and susceptance of the beam, compared to the d-c conductance, are shown to be lower as one approaches the beam voltage equivalent to the rest mass of an electron (511 kv). When beam conductance is compared to the d-c conductance for the gap transit angle in the region of 0 to π radians, it shows about 30 per cent reduction from its low-voltage value, when the beam voltage is one-fourth the rest mass equi-

valent. These results are necessary to understand the changes required in the external coupling of the klystron cavity as electron beams are accelerated to higher relativistic velocity. The results are also useful in the design of very high pulsed-power klystrons.

B. NANOSECOND PULSE STUDY

This project is concerned with the evaluation of the capability of high-power microwave amplifiers to process short-signal pulses; for example, pulses of the order of ten r-f cycles of the carrier frequency (this would be a one-nanosecond pulse length at a carrier frequency of 10 kMc/s).

There are two major problems associated with short-pulse amplification. The first is the finite, and usually rather narrow, bandwidth of high-power amplifiers. Short pulse lengths imply wide bandwidths associated with the frequency spectrum of the signal, and the amplifier must have sufficient bandwidth to amplify signals over the frequency spectrum of the signal (Research Report EE 541, P. R. McIsaac, "Influence of Cavity Q on Nanosecond Pulses"). The second problem is associated with the nonlinear properties of high-power amplifiers. These amplifiers must usually be operated in the nonlinear region for efficiency. Nonlinear operation can lead to distortion of the signal through harmonic generation as well as intermodulation distortion for signals with broad frequency spectra; therefore, the dependence of the distortion on the operating level of the amplifier is of interest.

This project has dealt with an introductory study of the short-pulse problem, which is described in Research Report EE 542 ("Response of Klystrons to Nanosecond Pulses," by N. Bose). A theoretical study has been

made using a simplified model of a high-power klystron in order to obtain preliminary and qualitative results. Since the bandwidth problem can be treated by conventional analysis, attention has been directed largely to the nonlinear problem. Either a ballistic theory or a nonlinear space-charge wave theory could be employed. The results of a ballistic-theory analysis are discussed in this report (an analysis using nonlinear space-charge wave theory has been initiated). Throughout this study, it is assumed that the signal is in the form of a constant-carrier frequency signal with a Gaussian envelope. This form of signal is not only convenient for analysis, but is also of considerable practical importance, since it is closely attainable in practice and has desirable properties for optimizing the range and resolution in radar.

This project has extended the nonlinear analysis of microwave amplifiers to the area of nonsinusoidal signals, where the signals are aperiodic and in the form of short pulses. It has immediate application to modern radar technology and may have to future communications technology.

C. VELOCITY FILTERS

The spent beam emerging from the second gap of a two-cavity klystron contains sufficient electrons with high velocities to cause appreciable X-ray radiation. A possible means of reducing the peak velocities, and thus the X-ray radiation, is to add a drift space and gap beyond the second cavity to act on the spent beam.

An analysis was formulated for a klystron system consisting of two drift spaces and three gaps. The first drift space and the first two gaps serve as a two-cavity klystron and the final drift space and gap serve as a

velocity filter. This analysis is a continuation of the work reported in an earlier technical report, and is presented in Research Report EE 547 (I. Turkekul, "Ballistic Analysis of Modulated Electron Beams"). Solutions to the resulting equations have been obtained on a Burroughs Datatron 220 digital computer. The data has been reduced to give the optimum length of the second drift space and the operating parameters of (1) the catcher gap of a two-cavity klystron for maximum output power, and (2) the velocity-filter gap for maximum reduction in the X-ray radiation. This analysis also showed that a r-f gap can be adjusted to interact with a bunch of electrons having a specific velocity.

D. REDUCTION OF HARMONICALLY RELATED SPURIOUS OUTPUTS

The generation by high-power radars of signals at frequencies other than those desired is an important radio-frequency compatibility problem. These undesired signals, or spurious outputs, can interfere with the parent radar receiver and other radar receivers in the vicinity, especially if the other receivers are operating at a frequency close to one of the spurious outputs. The usual technique used to prevent this problem is the addition of a filter at the output of the radar system. Another solution, apparently not considered up to now, is to design a final r-f amplifier that will limit the production of spurious outputs.

The portion of this problem undertaken by this task is the investigation of the design of a high-power klystron amplifier directed at reducing the harmonically related spurious outputs. The principal part of this design is associated with the output cavity of a high-power klystron, since it is this cavity that acts as a transformer to couple the r-f power developed by the

klystron interaction to an external transmission line. Harmonic power is developed in the electron beam of a klystron by the nature of its interaction and must be coupled through the output cavity if it is to appear in the external transmission line. The design problem, then, is to maximize the coupling of this transformer to the fundamental power and simultaneously to minimize the coupling to the harmonic powers. Since the output cavity is a multiresonant circuit, i.e., it has higher resonant modes as well as the fundamental mode, the design method is to control the higher resonant modes such that their frequency is well removed from the harmonic frequencies.

This task considers the design of the output cavity of a high-power klystron both theoretically and experimentally. The theoretical design provides the fundamental and higher-order resonances as a function of the geometrical parameters. Consequently it is possible to specify the fundamental frequency and to adjust the higher-order resonances, so that these occur between the harmonic frequencies.

A design of an output cavity based on these ideas is being tested experimentally under simulated operating conditions. The original output cavity of a commercial high-power S-band klystron has been removed and a new section is being attached. With this technique, a direct comparison of the harmonically related spurious outputs can be made for the "before" and "after" cases.

These experiments are not finished, but they are expected to be completed within several months. At that time, a separate report will be issued and will include full details of the results. An interim report

(Research Report EE 540, "Reduction of Spurious-Output Signals in High-Power Klystrons," by A. Ray Howland, Jr.) showing the progress to date is included.

CONCLUSIONS

The results of the research program on linear-beam tubes have shown that close linking of basic experimental studies of interaction with theoretical studies is a very fruitful approach to a better understanding of the performance of linear beam microwave tubes.

A. BEAM-CIRCUIT INTERACTION

It can be concluded that the theory for the small-signal Brillouin beam accurately describes the r-f forces in the beam, because the r-f current-density profile determined experimentally displays the surface current shell predicted by theory, and the measured plasma-frequency reduction factor is nearly identical to the predicted value. From the large-signal measurements, it is apparent that the effects of nonlinear forces arising in the driven and drifting beam are not well understood and that continued efforts are needed to formulate a satisfactory nonlinear theory.

It may also be concluded that a model in which the beam flow is laminar is very good for beams with voltages of several kilovolts or more, since the linearized theory of the laminar beam accurately predicts the behavior of these beams near Brillouin flow, even when a small amount of magnetic flux threads the cathode.

Also beam-generated ions do not seriously alter pulsed Brillouin beams of $2a/cm^2$ current density unless the pulse lengths exceed $10\ \mu sec$ for 1×10^{-7}mm Hg pressure. This limit may be scaled by keeping the product of the three factors constant.

Apparatus for plotting the electric field, which is suitable for exploring the fields in resonated microwave structures, has been assembled.

With this apparatus, the electromagnetic-field patterns in microwave interaction structures such as klystron cavities, extended interaction cavities, traveling-wave-tube circuits, and others, can be determined quickly and easily in graphic form. Numerical values for the electric-field components can be read off the recorder plots by using a calibration procedure.

From the experiment involving drive in a three-cavity klystron, one can conclude that, for fixed first-cavity drive power, the power output can be improved by driving the middle cavity in the most favorable phase, if the middle cavity is tuned below the frequency for optimum power output in the absence of middle-cavity drive. This increase however, is no greater than that which can be achieved by optimum tuning of the middle cavity with no middle-cavity drive power.

It may be concluded from the theoretical study of interactions of gaps that beam loading and detuning are reduced considerably as the velocity of the electron beam becomes relativistic.

B. NANOSECOND PULSE STUDY

This study has provided an initial, qualitative examination of the problems associated with short-pulse amplification in microwave amplifiers, especially those associated with nonlinear effects and finite bandwidth. At least a rough estimate of the relative importance of these two causes of distortion can be made. The nonlinear study gives an indication of the drive level at which distortion will become apparent and the rate of increase. These studies will form a basis for further, more detailed, studies of the influence of nonlinear interaction effects on the response of microwave amplifiers to short pulses.

C. VELOCITY FILTERS

Although the work on the velocity filter problem has not been completed, it appears that reduction of X-ray radiation in high-power klystrons can be achieved by acting on the spent beam with a drift space and cavity.

D. REDUCTION OF HARMONICALLY RELATED SPURIOUS OUTPUTS

It is feasible to design an output cavity for a high-power klystron amplifier that will theoretically minimize the spurious outputs at harmonic frequencies, although it is not yet known if the newly designed output cavity will reduce the spurious outputs in practice. This experiment is being undertaken now, and the results will be published. It is also feasible to design a transition from the output transmission line to the output cavity that loads the cavity in a symmetrical manner.

THE CURRENT DISTRIBUTIONS IN A VELOCITY-MODULATED BRILLOUIN-FOCUSED ELECTRON BEAM

A. S. Gilmour, Jr. and L. F. Eastman

School of Electrical Engineering
CORNELL UNIVERSITY
Ithaca, New York

RESEARCH REPORT EE 546

THE CURRENT DISTRIBUTIONS IN A VELOCITY-MODULATED BRILLOUIN-FOCUSED ELECTRON BEAM

A. S. Gilmour, Jr. and L. F. Eastman

LINEAR BEAM MICROWAVE TUBES

Technical Report No. 23 20 October 1962

Published under Air Force Contract No. AF30(612)-2573
Rome Air Development Center, Griffiss Air Force Base, New York

CONTENTS

ABSTRACT

This report describes the radio-frequency current distributions in a Brillouin-focused electron beam that has been velocity-modulated by a gridless-gap cavity. The report gives a review of the small-signal theory of ideal Brillouin beams in addition to small- and large-signal experimental results. An approximation is made to predict the r-f current contours in a Brillouin beam whose d-c current-density profile resembles a trapezoid. The predictions of this theory are found to agree well with actual beam behavior in that both the thickness and the amplitude of the r-f current density ring around the beam vary with the depth of modulation α when α is very small. For values of α above 0.1, the amplitude of the current-density ring becomes constant while the thickness of the ring continues to vary.

The large-signal results show that an average nonlinear force is present, which causes the average diameter of the modulated beam to be smaller at some axial positions than the diameter of the d-c Brillouin beam. In addition, the large-signal results show that at least two second- and two third-harmonic waves are present on the beam. One of these in each case is the component arising from the square-wave current-density wave at the edges of the beam. The other wave in each case is thought to have arisen from the nonlinear drive in the high alternating fields in the cavity gap. Plasma-frequency reduction factors for these nonlinearly launched harmonic waves are found to agree extremely well with those computed from the small-signal theory.

I. INTRODUCTION

The work accomplished to date on the beam analyzer program at Cornell has dealt mainly with the characteristics of d-c Brillouin beams,[1,2] and with the velocity distribution in the velocity-modulated Brillouin beam.[3] This work is very briefly reviewed in the Appendix. The purposes of this report are (1) to review the small-signal theory of the velocity modulation of ideal Brillouin beams, (2) to modify this theory for application to actual beams and compare its predictions with the small-signal r-f current contours found in the velocity-modulated beam described, and (3) to describe qualitatively the large-signal data obtained for fundamental and harmonic currents using the equipment described in the Appendix.

II. BRILLOUIN BEAM WITH SMALL-SIGNAL MODULATION

A. THEORY FOR IDEAL BRILLOUIN BEAM

In this section a general review is given of the small-signal theory of r-f disturbances on nonscalloping d-c Brillouin beams. Shown in Figure 1 is a sketch of the system to be analyzed. The review is divided into two main parts: The first is a description, originally presented by Rigrod and Lewis,[4] of the waves on a Brillouin beam; the second part deals with the modulation of a Brillouin beam by a gridless-gap cavity.

1. Wave Propagation on Brillouin Beams

For an electron beam with no angular variation in charge density, fields, etc., the Lorentz force equation is

$$\ddot{r} - r\dot{\theta}^2 = -\eta(E_r + B_z r\dot{\theta}) \quad , \tag{1}$$

$$\frac{1}{r}\frac{d}{dt}(r^2\dot{\theta}) = \eta B_z \dot{r} \quad , \tag{2}$$

$$\ddot{z} = -\eta E_z \quad , \tag{3}$$

where r, θ, and z are the co-ordinates of an electron in the beam. The d-c solutions to these equations, which are valid for nonscalloping Brillouin flow can be found in many references[5, 6, 7] and are

$$\dot{r} = 0 \ , \qquad \dot{\theta} = \omega_L = \frac{\eta B_B}{2} \ , \qquad \dot{z} = u_o \quad ,$$

$$\eta E_r = r\omega_L^2 \ , \qquad E_z = 0 \ , \qquad \rho_o = \frac{2\epsilon_o \omega_L^2}{\eta} \quad . \tag{4}$$

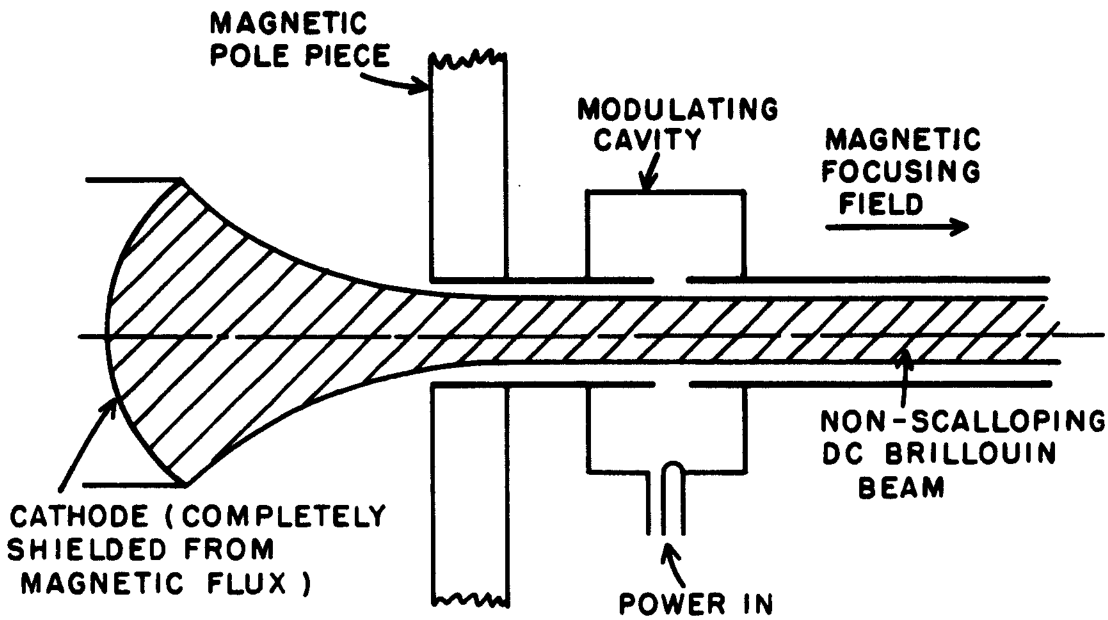

Figure 1. Diagram of Brillouin Beam and Modulating Cavity.

The important things to remember about the nonscalloping Brillouin beam are: (1) that the axial velocity is constant throughout the beam even though effects of depression in potential are accounted for, and (2) that in practice, beams closely approximating Brillouin beams can be formed.[1, 2] It is expected, therefore, that measurements made on the nearly ideal beam should agree well with predictions of the behavior of a Brillouin beam.

If the initial positions of an electron in the Brillouin beam are designated as r_o, θ_o, and z_o, then at time t, the co-ordinate of the electron will be r_o, $\theta_o + \omega_L t$, and $z_o + u_o t$. When the Brillouin beam is velocity modulated at small-signal levels, these co-ordinates and the axial and radial electric fields are perturbed. For nonrelativistic velocities, effects that are due to a-c magnetic fields are small and may be neglected.

Since it is assumed that no flux is present in the cathode region, Equation (2) may be integrated to show that $\dot{\theta} = \omega_L$, even when r-f disturbances are present. Equation (1) may therefore be written as

$$\ddot{r} + r\omega_L^2 = -\eta E_r \quad . \tag{5}$$

If it is assumed that the perturbed co-ordinates and fields are written as $r_o + r_1$ and $E_{r_o} + E_{r_1}$, where the subscript o identifies a d-c quantity and the subscript 1 identifies a r-f quantity; then Equation (5) may be written as

$$\ddot{r}_1 + (r_o + r_1)\omega_L^2 = -\eta(E_{r_o} + E_{r_1}) \quad , \tag{6}$$

and Equation (3) as

$$\ddot{z}_1 = -\eta E_{z_1} \quad . \tag{7}$$

It must be remembered that if the radial position of an electron in the beam varies, then the electron experiences a d-c electric field of magnitude,

$$-\eta E_{r_o} = \omega_L^2 (r_o + r_1) \quad . \tag{8}$$

Equation (8) is not valid for those electrons moving outside the outer diameter of the d-c Brillouin beam. This is because, as is shown in Figure 2, the radial electric field outside the beam is inversely proportional to radial position rather than directly proportional to it, as is the case inside the beam. If it is assumed that this error is small for small values of r_1, then Equation (6) becomes

$$\ddot{r}_1 = -\eta E_{r_1} \quad . \tag{9}$$

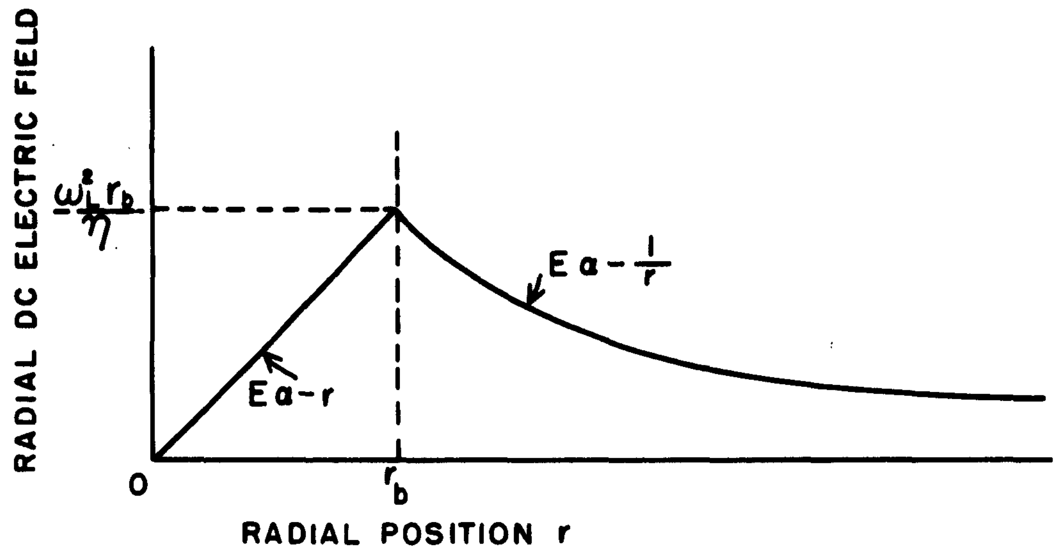

Figure 2. Radial Electric Field as Function of Radial Position for D-C Brillouin Beam (r_b = Outer Radius of D-C Brillouin Beam).

If it is assumed that all r-f quantities are small and that they vary as $e^{j(\omega t - \gamma z)}$, then

$$\frac{d}{dt} = j u_o (\beta_e - \gamma) \quad ,$$

where $\beta_e = \frac{\omega}{u_o}$, so that

$$\dot{r}_1 = j \frac{\eta}{u_o(\beta_e - \gamma)} E_{r_1} \quad , \tag{10}$$

and

$$\dot{z}_1 = j \frac{\eta}{u_o(\beta_e - \gamma)} E_{z_1} \quad . \tag{11}$$

The continuity equation may be written as

$$\underline{\nabla} \cdot (\rho \underline{u}) = - \frac{\partial \rho}{\partial t}$$

or as

$$\rho_o \underline{\nabla} \cdot \underline{u}_1 = - \frac{\partial \rho_1}{\partial t} - u_o \frac{\partial}{\partial z} \rho_1 = - \frac{d}{dt} \rho_1 \quad ; \tag{12}$$

so that

$$\rho_1 = j \frac{\rho_o}{u_o(\beta_e - \gamma)} \underline{\nabla} \cdot \underline{u}_1 \quad , \tag{13}$$

where

$$\underline{u_1} = \underline{\dot{r}_1} + \underline{\dot{z}_1} \quad .$$

Combining Equations (10), (11), and (13) gives the following equation for the r-f charge density:

$$\rho_1 = - \frac{\rho_o \eta}{u_o^2 (\beta_e - \gamma)^2} \underline{\nabla} \cdot \underline{E}_1 = - \frac{\beta_p^2}{(\beta_e - \gamma)^2} \rho_1 \quad , \tag{14}$$

since

$$\beta_p^2 = \frac{\omega_p^2}{u_o^2} = \frac{\eta \rho_o}{u_o^2 \epsilon_o} \quad .$$

Equation (14) has two solutions:

$$\beta_\rho^2 = (\beta_e - \gamma)^2 \quad , \tag{15}$$

and

$$\rho_1 = 0 \quad . \tag{16}$$

Equation (15) leads to $\gamma = \beta_e \pm \beta_\rho$, which is the result found for infinite planar flow. This result cannot be accepted, since it is expected that the over-all behavior of a Brillouin beam should not differ appreciably from

the behavior of the beam with confined flow. That is, it is expected that $\gamma = \beta_e \pm F\beta_p$, where F is the plasma-frequency reduction factor; and that $F \cong F_c$, where F_c is the reduction factor for a beam with confined flow. Equation (16) states that the charge density within the modulated beam is ρ_o. This means, of course, that the r-f convection current must result mainly from changes in the beam radius, as is shown in Figure 3.

With the preceding information about the motion of electrons in the Brillouin beam, it is possible next to set up and solve the wave equations for the electric and magnetic fields in the beam. The reason for doing this is, of course, to determine the reduction factor F for the plasma oscillations in the beam. To facilitate the solving of the wave equations and to make the matching of boundary conditions simpler, it is convenient to make an approximation at the edge of the beam. This approximation in effect simply re-

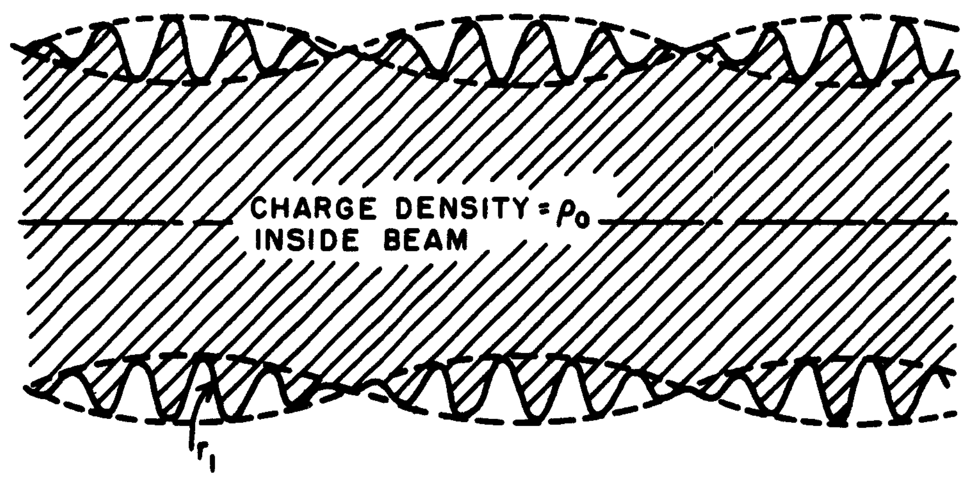

Figure 3. Diagram Showing R-F Modulation on Brillouin Beam. (Radius r_1 varies as $e^{j(\omega t - \gamma z)}$ where it is expected that $\gamma = \beta_e \pm F\beta_p$).

places the rippling edge of the beam by the equivalent surface-current density,

$$G_z = \rho_o r_1(r_o) u_o \quad , \tag{17}$$

where $r_1(r_o)$ is the value of the variable component of the radius evaluated at the d-c Brillouin beam radius. With this approximation, the beam may be considered to be a smooth cylinder surrounded by a shell of surface current.

From Maxwell's equations, now, the equations for the transverse-magnetic fields in the beam are found to be

$$\frac{1}{r}\frac{\partial}{\partial r}\left(r\frac{\partial E_{z1}}{\partial r}\right) - (\gamma^2 - k^2)\, E_{z1} = j\omega\mu J_{z1} \quad , \tag{18}$$

$$\left(1 - \frac{k^2}{\gamma^2}\right) E_{r_1} = \frac{j}{\gamma}\frac{\partial E_{z1}}{\partial r} - j\frac{\omega\mu}{\gamma^2} J_{r_1} \quad , \tag{19}$$

and

$$H_{\theta_1} \quad \frac{j}{\gamma} J_{r_1} + \frac{\omega\epsilon_o}{\gamma} E_{r_1} \quad , \tag{20}$$

where $k^2 = \omega^2\mu\epsilon_o$. Since a nonrelativistic beam is being considered, $k^2/\gamma^2 << 1$. In addition $J_z = \rho_o \dot{z}_1$, and $J_r = \rho_o \dot{r}_1$, so from Equations (10) and (11), it is seen that

$$J_{z_1} = j\frac{\epsilon_o u_o \beta_\rho^2}{(\beta_e - \gamma)} E_{z_1} \quad , \tag{21}$$

and

$$J_{r_1} = j\frac{\epsilon_o u_o \beta_\rho^2}{(\beta_e - \gamma)} E_{r_1} \quad . \tag{22}$$

By substituting Equations (21) and (22) into Equations (18), (19), and (20) and by neglecting relativistic terms, one can obtain the following equations for the transverse-magnetic fields inside the beam:

$$\frac{1}{r}\frac{\partial}{\partial r}\left(r\,\frac{\partial E_{z_1}}{\partial r}\right) - \gamma^2 E_{z_1} = 0 \quad , \tag{23}$$

$$E_{r_1} = \frac{j}{\gamma}\frac{\partial E_{z_1}}{\partial r} \quad , \tag{24}$$

$$H_{\theta_1} = \frac{\epsilon_o u_o}{\gamma}\left[\beta_e - \frac{\beta_\rho^2}{(\beta_e - \gamma)}\right] E_{r_1} \quad . \tag{25}$$

Equation (23) (which is the same as the equation for the z-component of the electric field in a charge-free region), is as expected, since it was shown earlier that $\rho_1 = 0$. The solution to Equation (23) inside the beam must be $E_{z_1} = AI_o(\gamma r)$, since the electric field must be finite at $R = 0$. In the region outside the beam, where Equation (23) applies,

$$E_{z_{1\,out}} = B\,I_o(\gamma r) + C\,K_o(\gamma r) \quad . \tag{26}$$

The magnetic field inside the beam can be found from Equations (24) and (25) and is

$$H_{\theta_1} = j\,\frac{\epsilon_o u_o}{\gamma}\left[\beta_e - \frac{\beta_\rho^2}{(\beta_e - \gamma)}\right] A I_1(\gamma r) \quad . \tag{27}$$

The magnetic field outside the beam is

$$H_{\theta_{1\,out}} = \frac{j\beta_e \epsilon_o u_o}{\gamma} \left[B I_1(\gamma r) - C K_1(\gamma r)\right] \quad . \tag{28}$$

In order to determine the constants A, B, and C, it is necessary to consider the boundary conditions at the drift-tube wall and at the edge of the beam. At the wall, where $r = r_c$, the z-directed electric field is zero, so

$$B = -C \frac{K_o(\gamma r_c)}{I_o(\gamma r_c)} \quad . \tag{29}$$

At the edge of the beam, the z-directed electric fields inside and outside of the beam must be equal, therefore

$$A I_o(\gamma r_b) = B \left[I_o(\gamma r_b) + C K_o(\gamma r_b)\right] \quad . \tag{30}$$

In addition, the magnetic field inside the beam plus the surface-current density at the edge of the beam must be equal to the magnetic field outside the beam. The surface-current density was $G_z = \rho_o r_1(r_b) u_o$, or with the aid of Equations (10) and (24),

$$G_z = j \frac{\beta_\rho^2 \epsilon_o u_o}{(\beta_e - \gamma)^2} A I_1(\gamma r_b) \quad . \tag{31}$$

Thus at the boundary where $H_{\theta_1} - G_z = H_{\theta_{1\,out}}$,

$$j \frac{\epsilon_o u_o}{\gamma} \left[\beta_e - \frac{\beta_\rho^2}{(\beta_e - \gamma)}\right] A I_1(\gamma r_b) - j \frac{\beta_\rho^2 \epsilon_o u_o}{(\beta_e - \gamma)^2} A I_1(\gamma r_b)$$

$$= \frac{j \beta_e \epsilon_o u_o}{\gamma} B \left[I_1(\gamma r_b) - C K_1(\gamma r_b)\right] \quad . \tag{32}$$

Now, by eliminating the constants A, B, and C, one obtains the following equation:

$$\left(1 - \frac{1}{F_B^2}\right)\frac{I_1(\gamma r_b)}{I_o(\gamma r_b)} = \frac{I_1(\gamma r_b) + K_1(\gamma r_b)\,\dfrac{I_o(\gamma r_c)}{K_o(\gamma r_c)}}{I_o(\gamma r_b) - K_o(\gamma r_b)\,\dfrac{I_o(\gamma r_c)}{K_o(\gamma r_c)}} \quad , \tag{33}$$

where $F_B^2 = (\beta_e - \gamma)^2/\beta_\rho^2$ is the reduction factor to be determined. By using the Wronskian relation,

$$I_o(\gamma r_b)\,K_1(\gamma r_b) + I_1(\gamma r_b)\,K_o(\gamma r_b) = \frac{1}{(\gamma r_b)} \quad ,$$

one can rewrite

$$F_B^2 = \gamma r_b I_1(\gamma r_b)\left[K_o(\gamma r_b) - \frac{I_o(\gamma r_b)\,K_o(\gamma r_c)}{I_o(\gamma r_c)}\right] . \tag{34}$$

Shown in Figure 4 are the plots of the plasma-frequency reduction factor F_B as a function of γr_b for various ratios of the diameter of the drift tube to the beam diameter. It is interesting that the reduction factors are smaller than for confined-flow beams, and that the asymptotic value for F at large values of γr_b is $1/\sqrt{2}$ instead of unity, which is the value for the confined-flow beam. The reason for the low values of F is apparent when the fields at the edge of the beam are examined. As is shown in Figure 5, the axial r-f fields in the Brillouin beam are weakened by bulging both into and out of the beam. In the confined-flow beam, the axial fields near the edge of the beam are weakened by bulging outward, whereas the fields near the axis are only slightly weakened. Thus the net axial field causing plasma

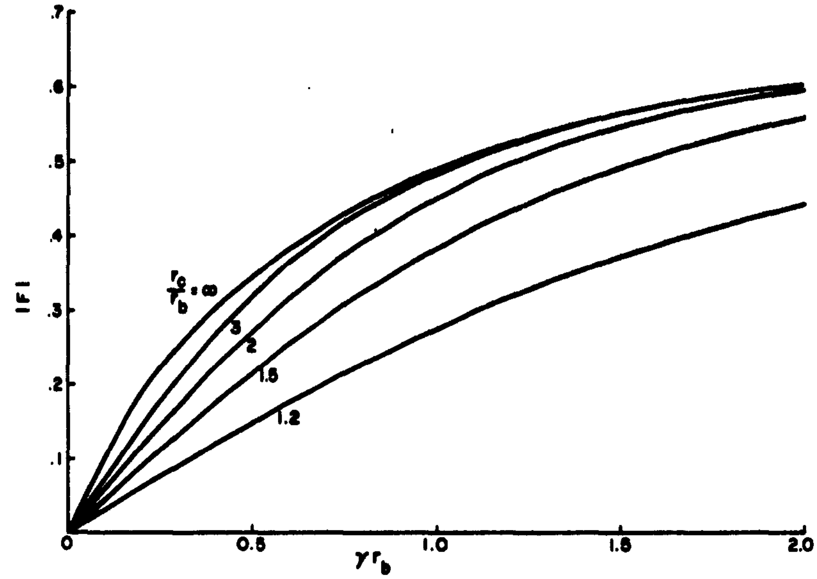

Figure 4. Plasma-Frequency Reduction Factors for Nonscalloping Brillouin Beams.

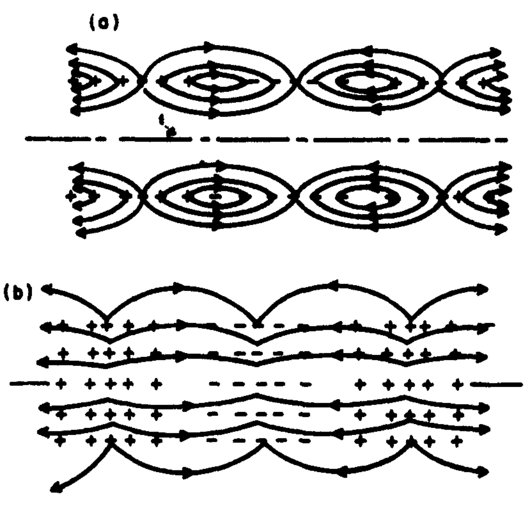

Figure 5. Diagram Showing Bulging of Electric Field Lines in (a) Brillouin Beam and (b) Confined Beam.

oscillations in the Brillouin beam is weaker than the one causing these oscillations in the confined beam, so that the reduction factor for the Brillouin beam is smaller than for the confined beam.

2. Velocity Modulation of Brillouin Beams

This part deals with the modulation of a Brillouin beam by a gridless-gap cavity and closely follows the work of Chodorow and Zitelli.[8] A sketch of a typical gridless-gap cavity and its orientation with respect to the beam is shown in Figure 1. Before computing the actual velocity modulation produced by the fields in the gap, we show that modulation by a gridless-gap cavity does launch the waves with zero r-f charge density, which were described in Section A1.

In the gap region, Equations (7) and (9) may be rewritten as

$$\ddot{r}_1 = -\eta(E_{r_1} + E_{c_r}) \quad , \tag{35}$$

and

$$\ddot{z}_1 = -\eta(E_{z_1} + E_{c_z}) \quad , \tag{36}$$

where E_{c_r} is the radial and E_{c_z} the axial component of the electric field produced by the cavity. Since Equations (35) and (36) are two components of a vector equation, and since under small-signal conditions, the operators d/dt and $\underline{\nabla}$: are interchangeable, one obtains

$$\frac{d}{dt}\ \underline{\nabla} \cdot \underline{u}_1 = -\eta\underline{\nabla} \cdot (\underline{E_{r_1}} + \underline{E_{z_1}}) = \frac{\eta}{\epsilon_o}\ \rho_1 \quad . \tag{37}$$

But from Equation (12),

$$\rho_o\ \underline{\nabla} \cdot \underline{u}_1 = -\frac{d}{dt}\ \rho_1 \quad ; \tag{38}$$

therefore by combining Equations (37) and (38), one obtains

$$\frac{d^2}{dt^2} \rho_1 + \omega_p^2 \rho_1 = 0 \quad . \tag{39}$$

Equation (39) states that a small volume of charge moving through the gap region must either vary in density as $e^{j\omega_p z}$ or must not vary at all. Again, $e^{j\omega_p z}$ variations must be rejected for the same reason that Equation (15) was rejected, and it is assumed that $\rho_1 = 0$.

If the gap dimensions are small compared to the free-space wavelength, the r-f electric fields in the gap region may be approximated by

$$E_{c_r} = j\, e^{j\omega t} \int_{-\infty}^{\infty} \frac{I_1(hr)}{I_o(hr_c)} A(h)\, e^{-jhz}\, dh \quad , \tag{40}$$

and

$$E_{c_z} = e^{j\omega t} \int_{-\infty}^{\infty} \frac{I_o(hr)}{I_o(hr_c)} A(h)\, e^{-jhz}\, dh \quad , \tag{41}$$

where h is a dummy variable of integration, and A(h) is a function to be determined by the boundary conditions at the drift-tube walls. A reasonable approximation to the field configuration at the drift-tube wall is that it is nearly the same as that between two knife edges; therefore

$$A(h) = \frac{V}{2\pi} J_o\ (hd/2) \quad , \tag{42}$$

where V is the peak value of the gap voltage, and d is the distance between the gap edges.

The equation for the beam velocity in the gap,

$$\dot{\underline{u}}_1 = -\eta(\underline{E_1} + \underline{E_c}) \quad ,$$

can be written as

$$\frac{\partial}{\partial z}\underline{u_1} + j\gamma\underline{u_1} = -\frac{\eta}{u_o}\underline{E_c} \quad , \tag{43}$$

where the effects of the electric fields originating from electron motions E_1 is approximated by changing $j\beta_e$ to $j\gamma$; therefore

$$\dot{r}_1 = -je^{j\omega t_o}\frac{\eta}{u_o}\int_{-\infty}^{\infty} e^{j\gamma z}\left\{\int_{-\infty}^{\infty}\frac{A(h)\,I_1(hr)}{I_o(hr_b)}\,e^{-jhz}\,dh\right\}dz$$

$$= ju_o\,\frac{a}{2}\left[J_o\left(\gamma\frac{d}{2}\right)\frac{I_1(\gamma r)}{I_o(\gamma r_c)}\right]e^{j\omega t_o} \quad , \tag{44}$$

and

$$\dot{z}_1 = -e^{j\omega t_o}\frac{\eta}{u_o}\int_{-\infty}^{\infty} e^{j\gamma z}\left\{\int_{-\infty}^{\infty}\frac{A(h)\,I_o(hr)}{I_o(hr_c)}\,e^{-jhz}\,dh\right\}dz$$

$$= u_o\,\frac{a}{2}\left[J_o\left(\gamma\frac{d}{2}\right)\frac{I_o(\gamma r)}{I_o(\gamma r_c)}\right]e^{j\omega t_o} \quad , \tag{45}$$

where, as usual, a is the depth of modulation and is equal to V/V_o. The time t_o is the time at which the electrons pass the position $z = 0$ at the center of the gap. Now the velocities given by Equations (41) and (42), and the zero r-f charge density and zero radial displacement at $z = 0$ are the

initial conditions for the waves described in Section A1. From Equations (10) and (11), and from the known variations of the electric fields with radius, it is seen that the magnitude of the radial and axial velocities after modulation can be written as

$$\dot{r}_1 = -\frac{\eta}{u_o(\beta_e - \gamma)} A\, I_1(\gamma r) \quad ,$$

and

$$\dot{z}_1 = j\frac{\eta}{u_o(\beta_e - \gamma)} A\, I_o(\gamma r) \quad ;$$

or as

$$\dot{r}_1 = j\left[\nu_1 e^{-j\beta_q z} + \nu_2 e^{j\beta_q z}\right] I_1(\gamma r)\, e^{j(\omega t - \beta_e z)} \quad , \tag{46}$$

and

$$\dot{z}_1 = \left[\nu_1 e^{-j\beta_q z} + \nu_2 e^{j\beta_q z}\right] I_o(\gamma r)\, e^{j(\omega t - \beta_e z)} \quad , \tag{47}$$

since both $\dot{r}_1$ and $\dot{z}_1$ vary as $e^{j(\omega t - \gamma z)}$, where $\gamma = \beta_e \pm F\beta_p = \beta_e \pm \beta_q$. At $z = 0$, Equations (46) and (47) can be equated to Equations (44) and (45), so that

$$\nu_1 + \nu_2 = u_o \frac{\alpha}{2} \frac{J_o\left(\gamma \frac{d}{2}\right)}{I_o(\gamma r_c)} \quad . \tag{48}$$

Not only must the velocities in the drift tube and the gap be equal at $z = 0$, but the displacement of the electrons from their d-c positions must also be equal. In the drift tube, the radial displacement is

$$r_1 = -\frac{1}{\beta_q u_o}\left[\nu_1 e^{-j\beta_q z} - \nu_2 e^{j\beta_q z}\right] I_1(\gamma r)\, e^{j(\omega t - \beta_e z)} \quad . \tag{49}$$

If it is assumed that no radial displacement of the electrons takes place in the gap, then at $z = 0$, one obtains $r_1 = 0$, and so $\nu_1 = \nu_2$. Finally, then, the equations for the electron velocities and for the r-f component of the beam radius become

$$\dot{r}_1 = j u_o \frac{a}{2} J_o(\gamma \frac{d}{2}) \frac{I_1(\gamma r)}{I_o(\gamma r_c)} \cos \beta_q z\, e^{j(\omega t - \beta_e z)} \quad , \tag{50}$$

$$\dot{z}_1 = u_o \frac{a}{2} J_o(\gamma \frac{d}{2}) \frac{I_o(\gamma r)}{I_o(\gamma r_c)} \cos \beta_q z\, e^{j(\omega t - \beta_e z)} \quad , \tag{51}$$

and

$$r_1 = j \frac{1}{\beta_q} \frac{a}{2} J_o(\gamma \frac{d}{2}) \frac{I_1(\gamma r_b)}{I_o(\gamma r_c)} \sin \beta_q z\, e^{j(\omega t - \beta_e z)} \quad . \tag{52}$$

Equations (50), (51), and (52), and the condition that $\rho_1 = 0$ show that there are two components of r-f current density in the axial direction. The first, a volumetric current density, is simply the product $\rho_o \dot{z}_1$. The second is a surface-current density that results from the rippling of the beam edge. If a Fourier analysis is made of the current density at r_b, which is the radius of the d-c beam, it is evident that odd harmonics of current density are present, as well as the fundamental component, since the current density is a square wave. In fact, a complete expression for the surface current density is

$$J_z = J_o\left(\frac{1}{2} - \frac{1}{\pi}\sin^{-1}\delta\right) + \frac{2J_o}{\pi}\sum_{n=\mathrm{odd}}^{\infty}\frac{\cos(n\sin^{-1}\delta)}{n}\sin n\beta_e z$$

$$-\frac{2J_o}{\pi}\sum_{n=\mathrm{even}}^{\infty}\frac{\sin(n\sin^{-1}\delta)}{n}\cos n\beta_e z \quad , \tag{53}$$

in which $-1 \leq \delta \leq 1$ is a measure of the radial position r_δ, at which J_z is to be evaluated and can be determined from

$$r_\delta = r_b + \delta A \sin\beta_q z \quad , \tag{54}$$

where

$$A = \frac{1}{\beta_q}\frac{a}{2} J_o\left(\gamma\frac{d}{2}\right)\frac{I_1(\gamma r_b)}{I_o(\gamma r_c)} \quad . \tag{55}$$

Now, from Equation (53) and from $\rho_o \dot{z}_1$, the various components of the current in the modulated beam can be determined to be as shown in Figures 6 and 7. The curves in Figure 6 show the average, fundamental, 2nd-harmonic, and 3rd-harmonic current distributions as a function of the radial position in the beam for two drive levels. It is important to remember that the integral across the beam of any harmonic-current component vanishes. For the second harmonic component, for example, the current peak inside r_b is 180° out of phase with the current peak outside r_b, so that the net second-harmonic current is zero. Thus, only the fundamental current component can induce currents in an external circuit. The curves in Figure 7 show the average and fundamental currents as functions of the horizontal

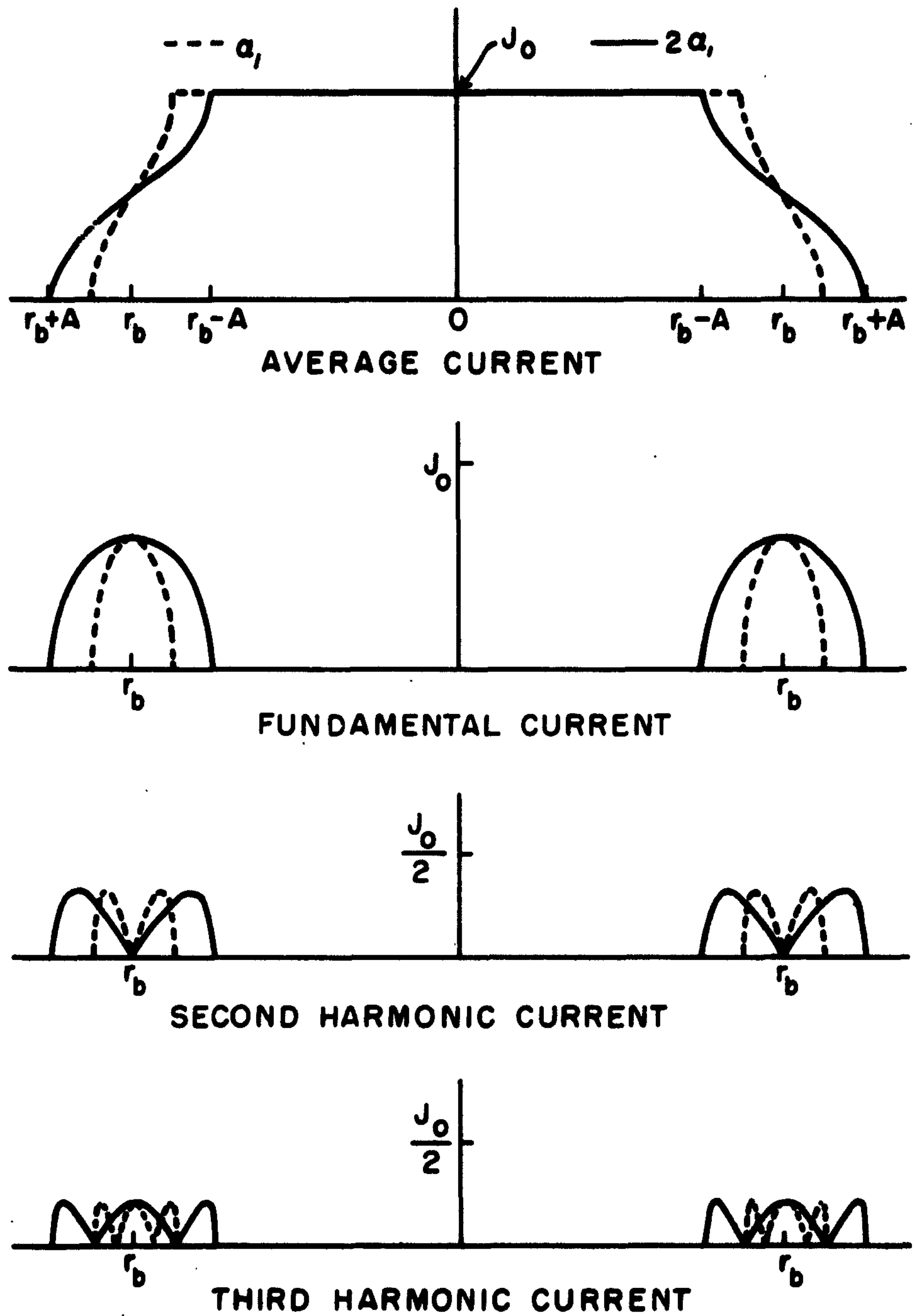

Figure 6. Components of Current in Brillouin Beam, Velocity-modulated at Small-Signal Levels.

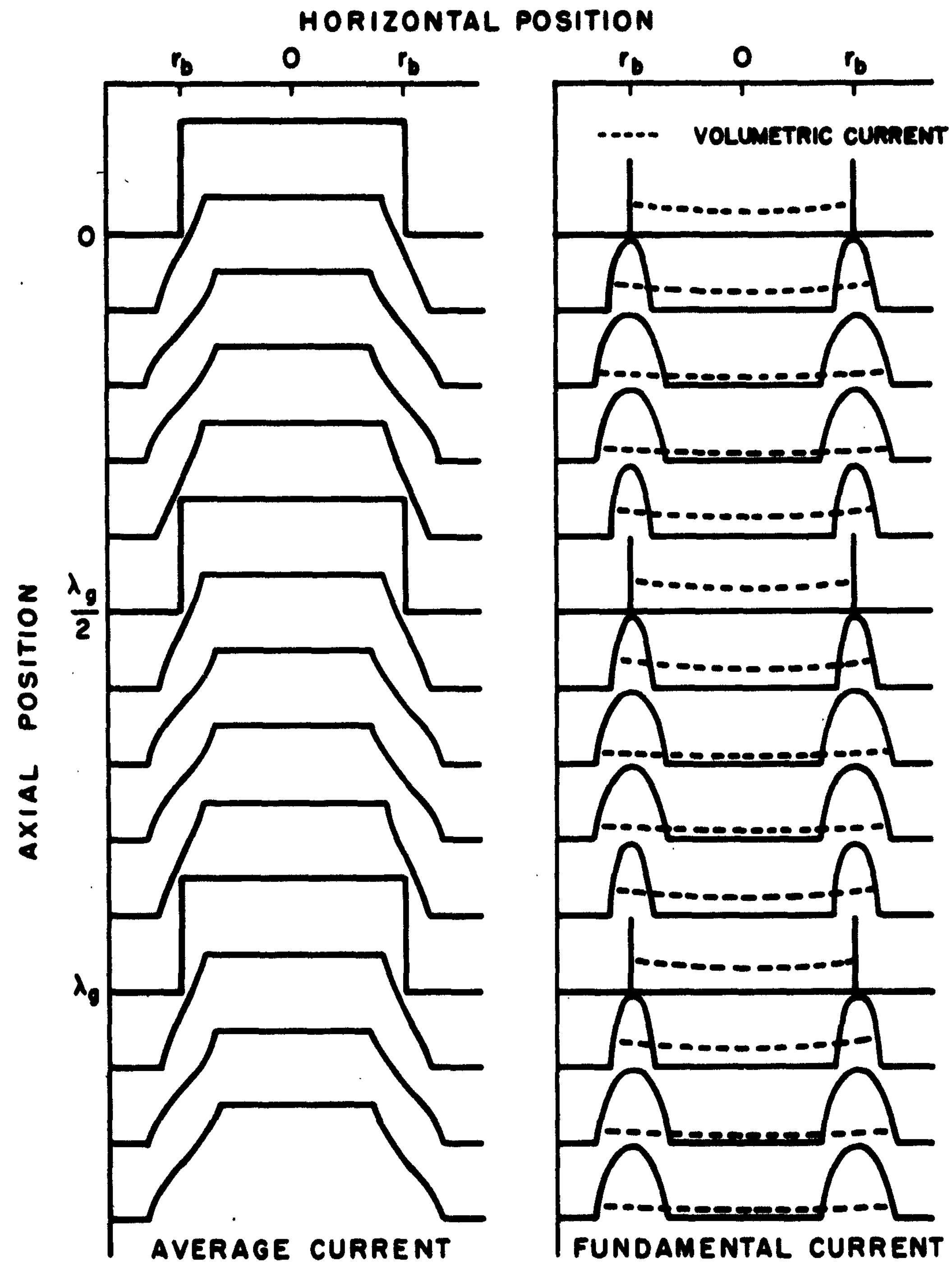

Figure 7. Average and Fundamental Currents as Functions of Horizontal and Axial Positions.

and axial positions in the beam. The zero position is where the modulating cavity is assumed to be. Note that exaggerated curves in the volumetric current are included in the plot of fundamental current. Note also that the volumetric current goes to zero at horizontal positions that are $\lambda_q/4$ from the zeros of the surface current.

The magnitude of the volumetric current in the beam is simply the integral of $\rho_o \dot{z}_1$ across the beam and is therefore

$$I_\nu = \int_0^{r_b} \rho_o \dot{z}_1 \, 2\pi r dr \quad ,$$

or

$$I_\nu = \frac{2\pi r_b J_o}{\gamma} \frac{a}{2} J_o \left(\gamma \frac{d}{2}\right) \frac{I_1(\gamma r_b)}{I_o(\gamma r_c)} \cos \beta_q z \, e^{j(\omega t - \beta_e z)} \quad . \tag{56}$$

The surface current is $2\pi r_b \rho_o u_o r_1$; therefore

$$I_s = j \frac{2\pi r_b J_o}{\beta_q} \frac{a}{2} J_o \left(\gamma \frac{d}{2}\right) \frac{I_1(\gamma r_b)}{I_o(\gamma r_c)} \sin \beta_q z \, e^{j(\omega t - \beta_e z)} \quad . \tag{57}$$

The ratio of the maximum value of I_ν to the maximum value of I_s is therefore seen to be β_q/γ; therefore the volumetric current can normally be neglected.

B. EXPERIMENTAL RESULTS WITH NONIDEAL BEAM

This section consists of two parts. The first presents modification of the ideal beam theory, which takes into account the fact that the curve of charge density as a function of radius in actual beams is more nearly

trapezoidal than rectangular in shape, as shown in Figure 8. (This distortion of the ideal beam is due mainly to the thermal velocities of the electrons.) The second part of this section presents a comparison of the predictions of the first part with data taken on a nearly ideal Brillouin beam. A very brief description of this beam and of the equipment used to obtain it is given in the Appendix. More complete descriptions are included in reports by Gilmour[1, 3] and Hallock[2].

1. Approximations to Trapezoidal Beam

Since the part of the d-c trapezoidal beam where the charge density is constant behaves like a Brillouin beam, it can be assumed that there is no r-f space-charge density. This means, of course, that when the beam tends to bunch in the axial direction, an expansion in the radial direction occurs, which is sufficient to prevent bunching. Under small-signal conditions, if the distance in which the charge density drops from ρ_o to zero is small compared to the radius r_b, it may be assumed that the radial excursion of all parts of the sloping beam edge is the value of $r_1(b)$ given in Equation (52) for the beam with vertical edges. Therefore, as is shown in Figure 9, when the depth of modulation α is very small, the r-f current density waveform at $r(b)$ is a sinusoid. For the beam with vertical edges, it was shown that this waveform is a square wave. As α is increased, the excursions of the beam edge become large enough to cause the peaks of the sine wave to become clipped. Finally for a reasonably large α, the current density waveform closely approximates a square wave.

Shown in Figure 10 are curves of the fundamental current density as a function of radius for various drive levels. Notice that for small drive

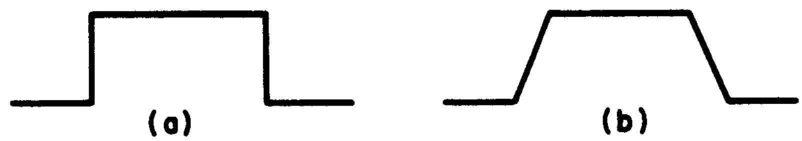

Figure 8. Charge Density as a Function of Radial Position for (a) Ideal Beam, (b) Practical Beam.

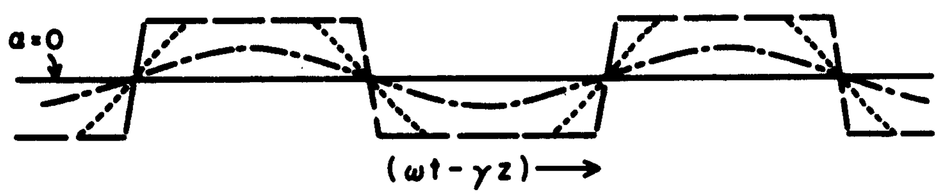

Figure 9. R-F Current Density Waveform at r(b) as a Function of (ωt - γz) for Various Drive Levels.

KEY FOR FIGS. 9 AND 10
LARGE a
MEDIUM a
SMALL a

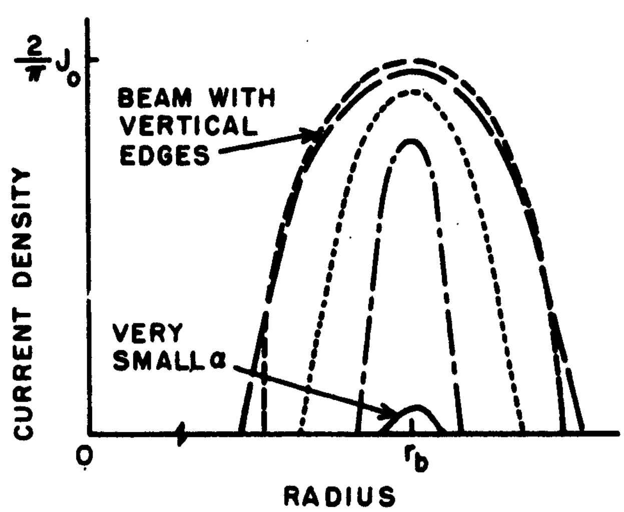

Figure 10. Curves of Fundamental Current Density as a Function of Radius for Various Drive Levels.

levels, both the amplitude and the width of the current profile change; whereas at large signal levels, the amplitude is nearly constant, but the width of the profile changes. For the beam with vertical edges, it should be remembered that the amplitude of the current-density profile is always $\frac{2}{\pi} J_o$ and that only the width of the profile changes with α. Approximate curves of the average and fundamental current densities as functions of the horizontal and axial positions in the beam for a reasonably large value of α (still within the small-signal range) are shown in Figure 11.

No mention has been made yet of the harmonic current densities generated by small-signal modulation of the trapezoidal beam. It was shown in Figure 9 that at the radial position $r(b)$, no harmonic signals are generated as long as the α is small enough to prevent clipping of the sinusoid. Harmonics are still generated at radii greater and smaller than $r(b)$, where clipping of the sinusoid does take place, but, these are much smaller than those generated in the case of the beam with vertical edges. How much the harmonic amplitude in the trapezoidal beam decreases depends, of course, upon the slope of the edge of the beam.

2. Comparison of Experimental Results with Approximations to Trapezoidal Beam

Shown in Figure 12 are plots of the average and fundamental currents taken at a small-signal level with the apparatus described in the Appendix and elsewhere[1, 2, 3]. The current data are plotted as a function of the horizontal position for various axial positions along the beam. Notice that the average current profiles indicate that this beam closely approximates the trapezoidal beam described in the previous section. The drive level in Figure 12 is low enough so that the difference between the average current

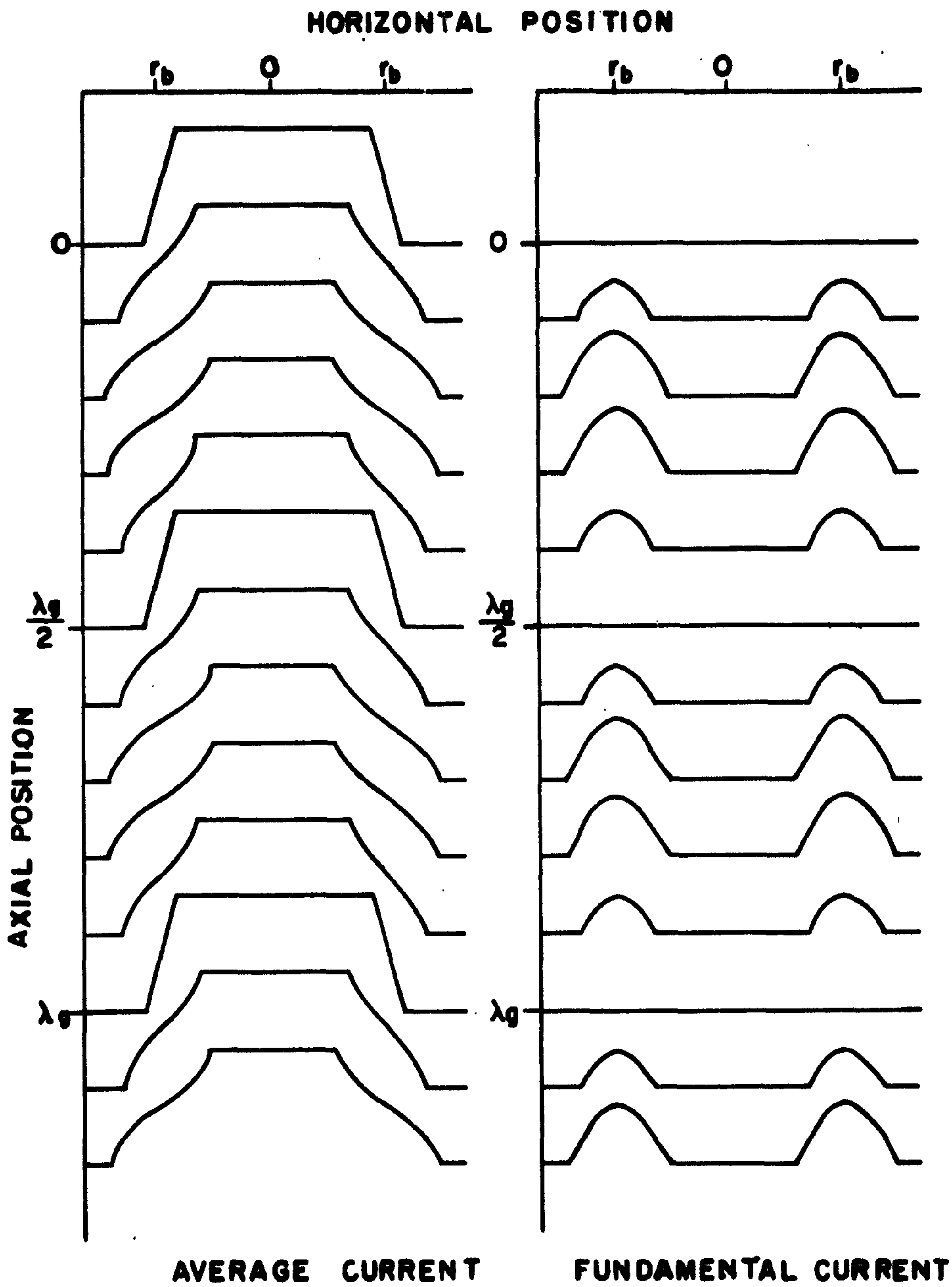

Figure 11. Approximate Current Densities as Functions of Horizontal and Axial Positions in Trapezoidal Beam.

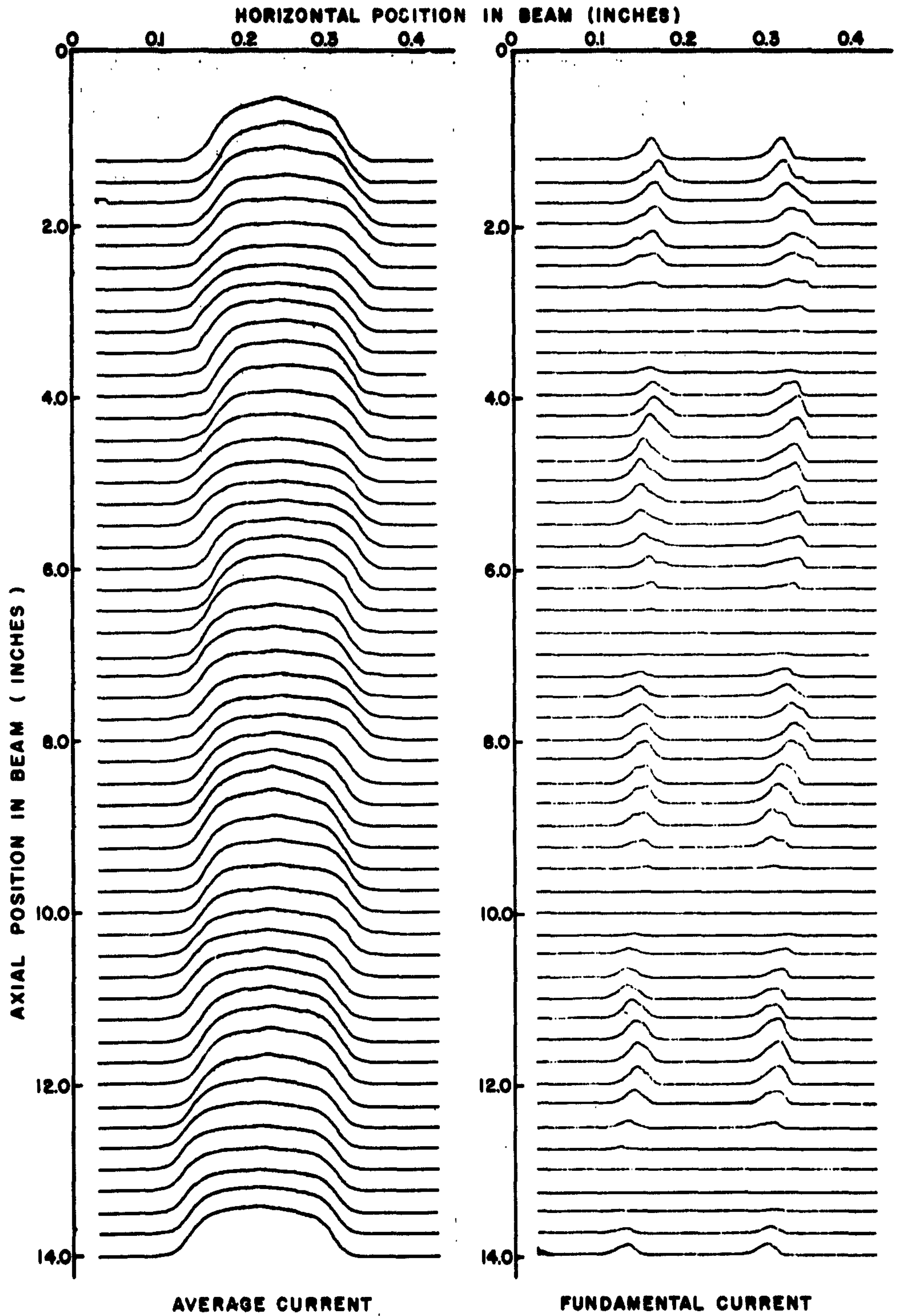

Figure 12. Average and Fundamental Current-Density Plots as Functions of Horizontal and Axial Positions in Beam for an α of .041.

profiles and the profiles of the d-c Brillouin beam are not apparent. Except for irregularities caused for higher-order effects at the edge of the d-c beam, the fundamental current pattern is very much like that shown in Figure 11. Notice that both the width and the amplitude of the current peaks vary with distance. This same effect has been reported by Winslow.[9] Unfortunately, no calibration of the r-f current probe was possible, so that the amplitudes of the fundamental current curves must not be compared with the amplitudes of the average current curves in Figure 12 or in succeeding figures in this report.

Shown in Figure 13 are plots of the peak velocity of the beam as a function of axial position for the α of .041 of Figure 12 as well as for several other values of α. For the two lowest values of α, these curves are seen to be nearly as predicted by theory. The main deviations have been pointed out in the literature[3] and are: (1) that the nulls do not reach the d-c beam level, and (2) that the maxima decrease slightly with distance. A possible explanation of this behavior is given in an earlier paper.[3] It should be mentioned here that the experimental value of the plasma-frequency reduction factor determined on the basis of data given in Figures 12 and 13, as well as in an earlier study,[3] is 0.42. This agrees extremely well with the value of 0.413 obtained from Equation (34) in Figure 4.

Shown in Figure 14 are plots of the average and fundamental currents; these, however, are for $\alpha = .083$. Notice that both the amplitudes and the widths of the fundamental current peaks are greater than those given in Figure 12. No harmonic data are available at the drive levels of Figure 12 and 14 because the harmonic currents were found to be partially or totally masked by the noise of the receiver system used for current measurements..

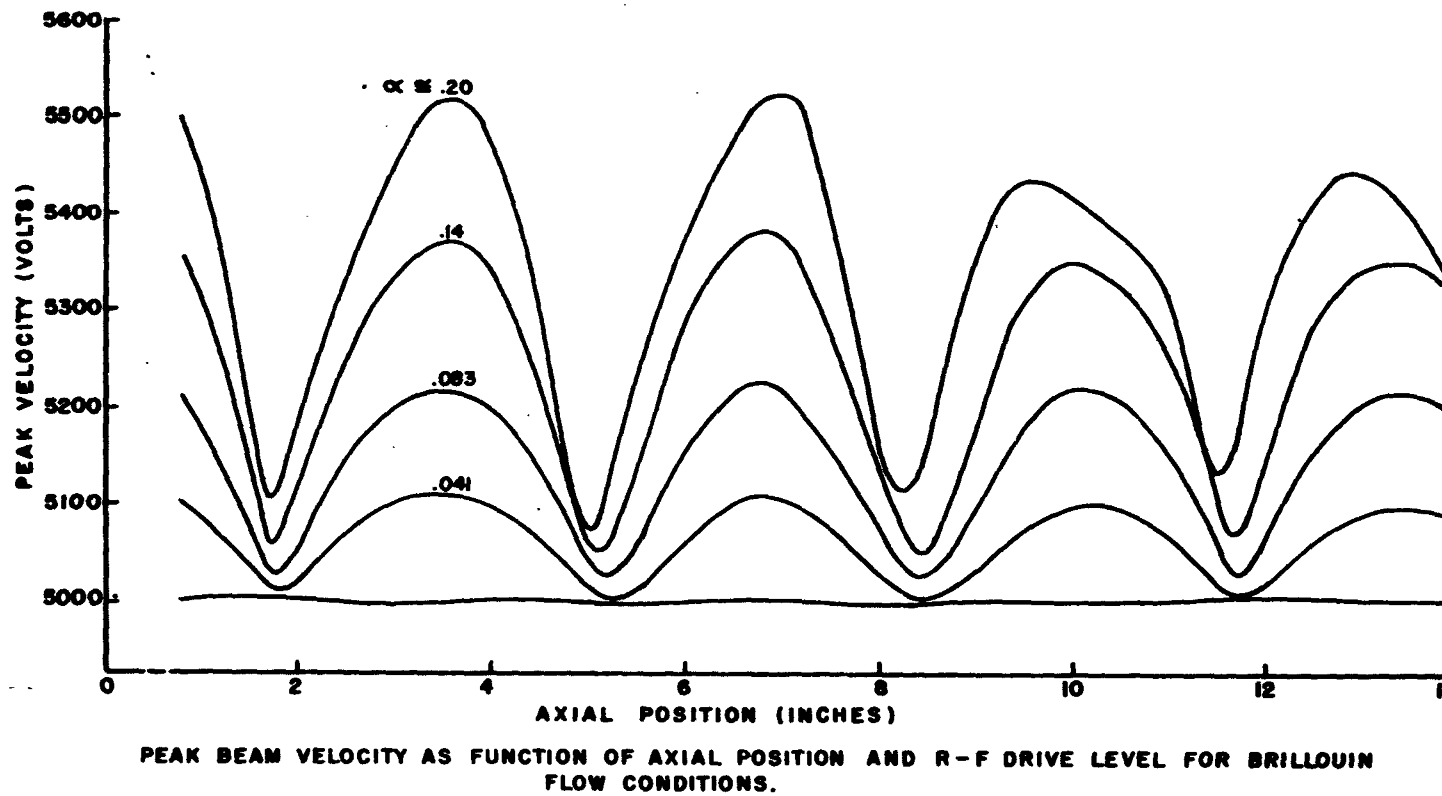

Figure 13. Peak Beam Velocity as Function of Axial Position and R-F Drive Level for Brillouin Flow Conditions.

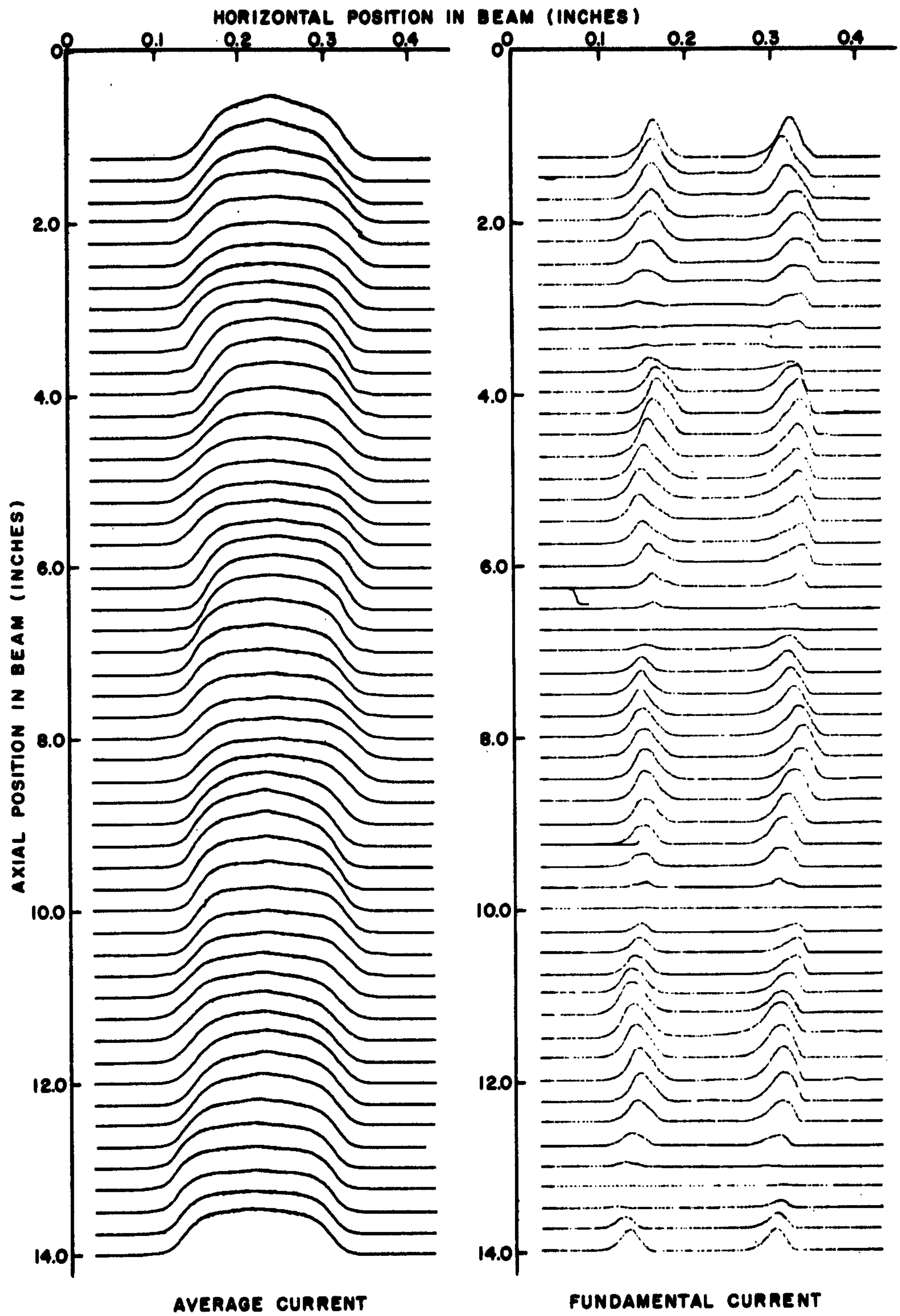

Figure 14. Average and Fundamental Current-Density Plots as Functions of Horizontal and Axial Positions in Beam for an α of .083.

III. BRILLOUIN BEAM WITH LARGE-SIGNAL MODULATION

Although considerable effort has been devoted to the large-signal analysis of Brillouin beams, a satisfactory theory has not yet been formulated; therefore, this section contains experimental results of large-signal Brillouin beam and a qualitative rather than quantitative discussion of the results.

Shown in Figures 15 and 16 are curves of the average and fundamental currents for values of α of 0.14 and 0.20. The $\alpha = 0.14$ curves show that the amplitudes and widths of the fundamental current peaks have increased when α was increased. The curves of $\alpha = 0.20$, however, show a further increase in the width of the current peaks, but, little or no increase in the amplitude of peaks. Thus the development shown in Figure 10 for large values of α has been reached.

Spreading of the average current profiles where maxima in the fundamental current profiles occur is evident in Figures 15 and 16. These average current profiles are similar to those predicted in Figure 11. The main differences are due to the d-c beam profile not being quite trapezoidal but having rounded corners instead. This means, of course, that the average current profiles should not have the sharp corners shown in Figure 11. One important nonlinear effect that is most easily noticeable in Figure 16 is the narrowing of the average current profiles to diameters smaller than the d-c Brillouin beam diameter. Because of the enlarged radial motions near the surface, an average nonlinear force arises, which is directed radially inward. This causes a sharp beam focus one-quarter of a reduced plasma wavelength from the fundamental current maxima. For drives as large and

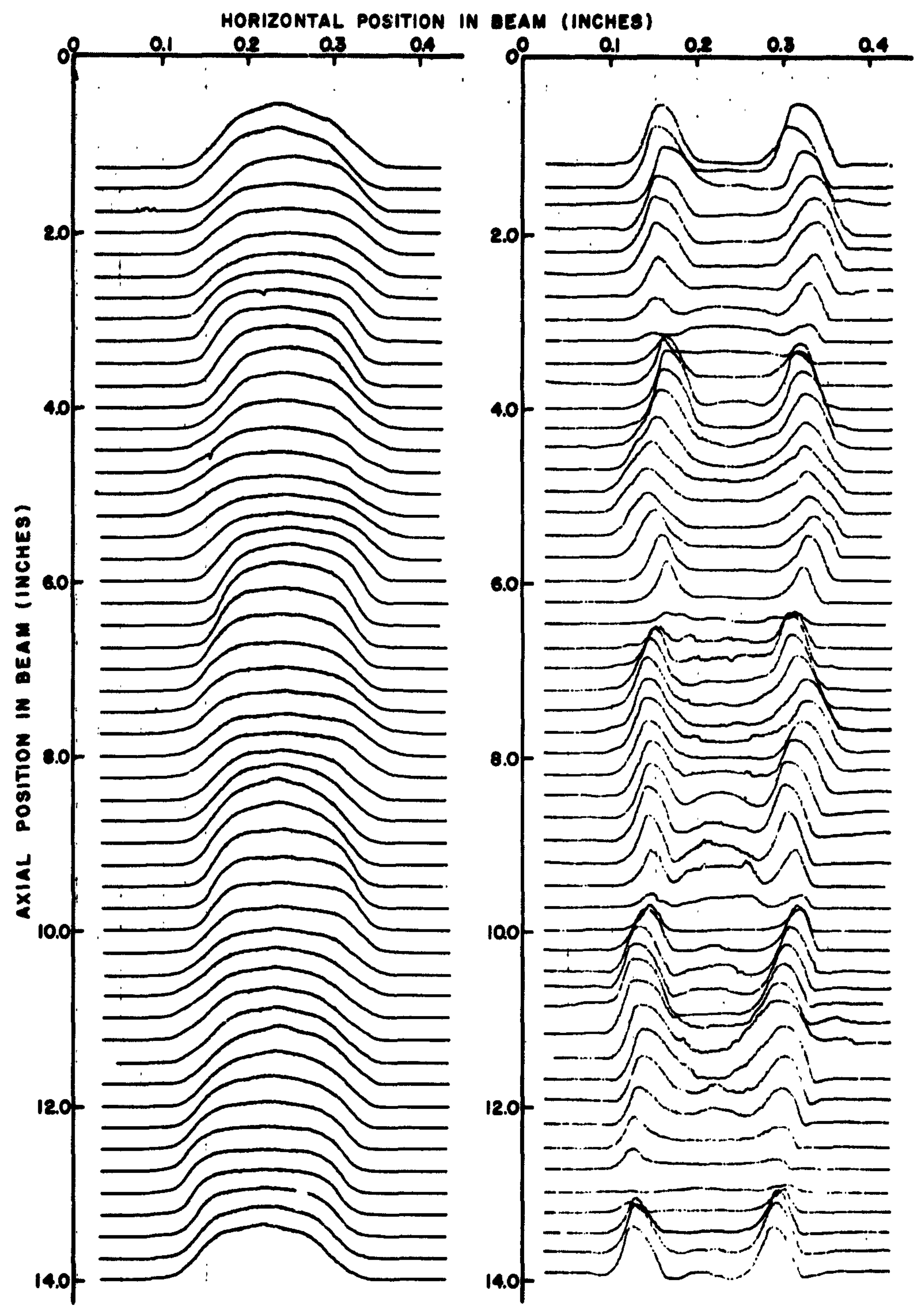

Figure 15. Average and Fundamental Current-Density Plots as Functions of Horizontal and Axial Positions in Beam for an α of 0.14.

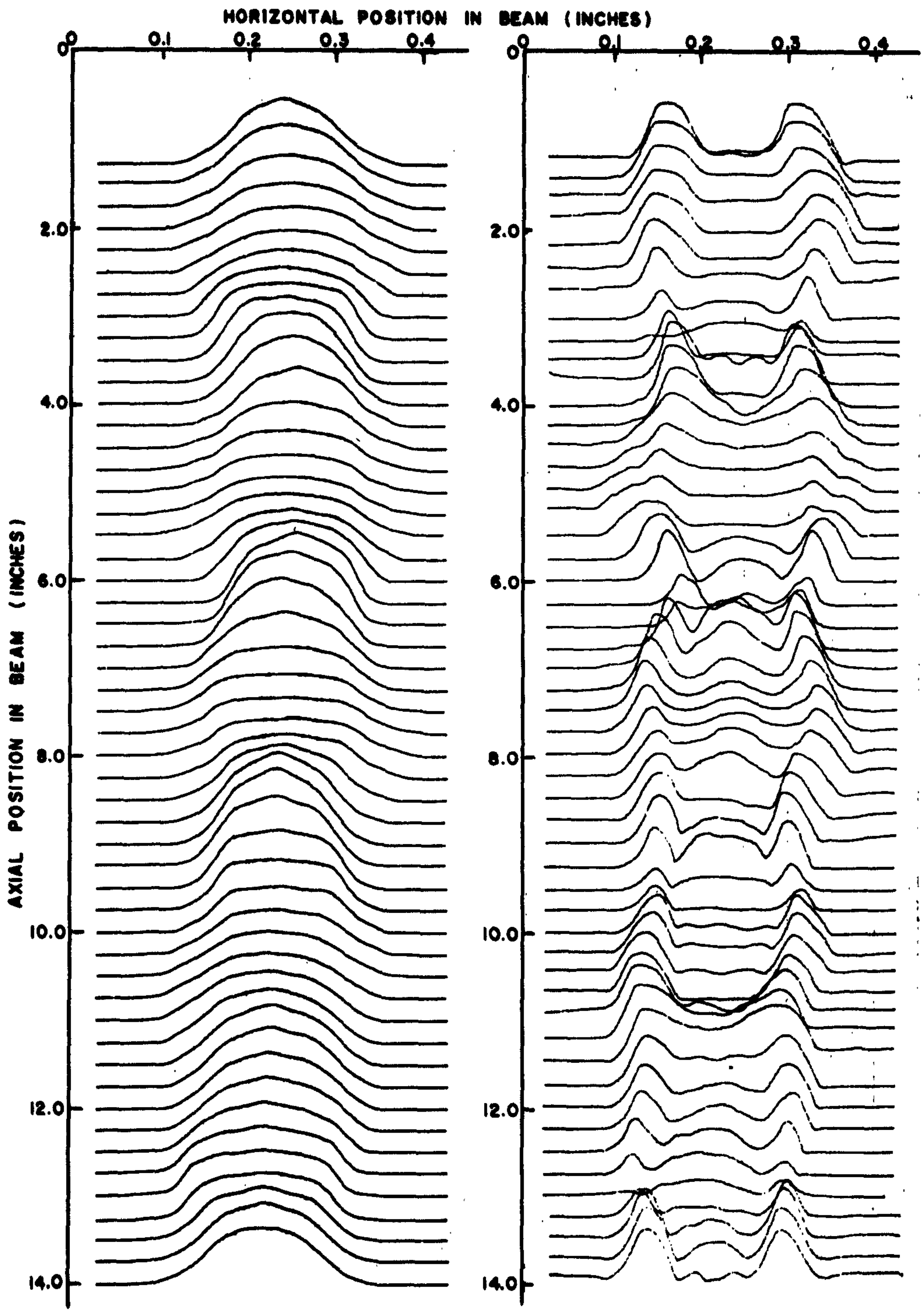

Figure 16. Average and Fundamental Current-Density Plots as Functions of Horizontal and Axial Positions in Beam for an α of 0.20.

larger than the one used in Figure 16, the average current density at the beam center is altered, and severe alteration of beam spreading and beam focusing are noticeable with distance. This is especially evident in Figure 16 after the second null in the surface current.

It may be noticed that a small amount of volumetric fundamental current density has arisen in Figures 15 and 16, especially at larger drift distances. A portion of this current density is clearly the $\rho_o \dot{z}$ component, which is predicted by the small-signal Brillouin beam theory. A second portion of this current density arises from nonlinear effects and is relatively irregular and never large when reasonable wave-like behavior is observed.

Second-harmonic current-density profiles for drive levels of $\alpha = .14$ and $\alpha = .20$ are shown in Figure 17. These are considerably lower in amplitude than the fundamental current densities for the same drive levels and remain mainly as surface currents. Since no calibration of the circuit for the second-harmonic current was possible when the second harmonic data was taken, no comparison of absolute amplitudes of fundamental and second-harmonic currents is possible. There appear to be at least two current waves present in the data shown in Figure 17. The first is the component arising from the square-wave current-dentisy wave at the edges of the beam. This component was predicted in Section II. A second component is present, which is thought to have arisen from a wave at the second-harmonic frequency launched at the cavity by the nonlinear drive in the high alternating fields in the gap. This wave has its own standing-wave period along the beam, which is considerably less than that for the fundamental frequency because of a larger plasma-frequency reduction factor at the

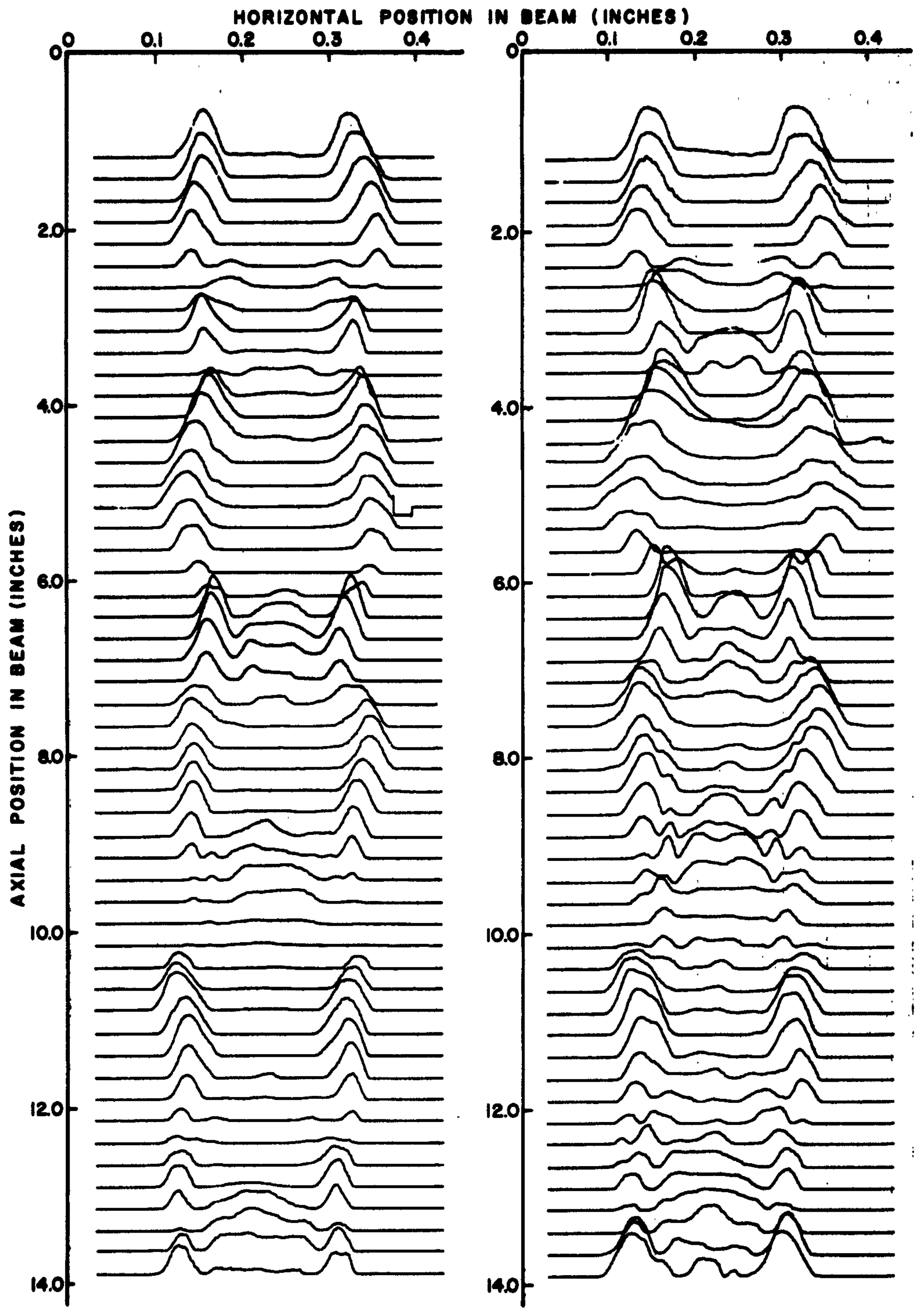

Figure 17. Second-Harmonic Current-Density Plots as Functions of Horizontal and Axial Positions in Beam for a = .14 (left) and a = .20 (right).

second-harmonic frequency. The ratio of the second-harmonic to the fundamental frequency-reduction factor determined from Figures 17 and 13 is approximately 1.27 and that obtained from Figure 4 is 1.33, which supports the idea that a second-harmonic signal is launched by the cavity.

It can be seen that when this short-period component with a single maximum in radius goes to zero, the long-period component with its double maximum in radius remains. Note also that the longitudinally spaced zeros of the second-harmonic current density are less regular than those of the fundamental current density. This is due to the two waves with different reduced plasma wavelengths beating with each other with distance.

Third-harmonic current-density contours across the beam as a function of drift distance for the drive level $\alpha = .14$ are shown in Figure 18. As in the second harmonic case, the current is predominantly at the surface and is quite small, no comparison of absolute amplitudes can be made, and a component launched by the nonlinear field in the gap is present but now the magnitude of this component is not too much larger than the component resulting from large alternating positions at the fundamental frequency. The component caused by the nonlinear field has an even shorter period than that of the second harmonic, because it is a third-harmonic wave, having a still larger plasma-frequency reduction factor than the second-harmonic wave. In this case, the experimental ratio of the reduction factor of the third harmonic to fundamental frequency is about 1.53, and the predicted ratio is 1.47, indicating very good agreement. The irregular longitudinal spacings of the zeros is present as in the second harmonic, but is complicated by a small, comparable, body current density.

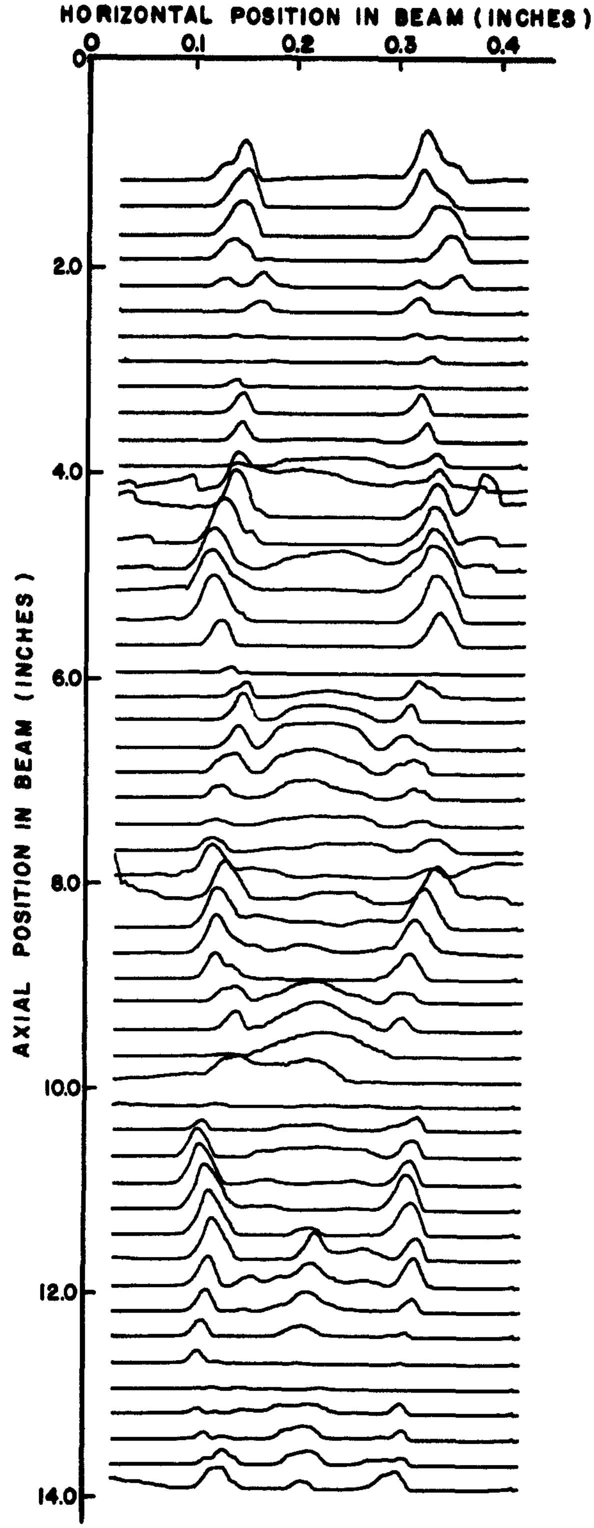

Figure 18. Third-Harmonic Current-Density Plots as Functions of Horizontal and Axial Positions in Beam for a = .14.

IV. CONCLUSIONS AND RECOMMENDATIONS

In conclusion, it may be said that the small-signal theory of the Brillouin beam accurately describes the r-f forces in the beam because (1) the r-f current-density profiles determined experimentally display the shell of surface current predicted by the theory and (2) the measured plasma-frequency reduction factor is nearly identical to the predicted value. In addition, it appears that the modification made in the theory for beams with trapezoidal cross sections is valid, since the shapes of the experimental r-f current contours agree well with those predicted by theory.

From the discussion of the large-signal effects, it is apparent that the nonlinear forces arising in the beam are not well understood, and it is recommended that continued efforts be devoted to the formulation of a satisfactory nonlinear theory.

APPENDIX: PROBE CIRCUITRY FOR MEASURING R-F CURRENT

The beam analyzer used in obtaining the r-f current data presented in this report is the one described by Gilmour[1,3] and Hallock[2]. The important features of this analyzer, and the r-f current-measuring probe and circuitry, are described here. The parts of the analyzer essential to the r-f current measurements are shown in Figure A-1. The electron beam, on which measurements were made, was generated by the shielded Pierce gun shown at the right side of the figure. This gun was normally pulse operated at 5000 volts and had a microperveance of 1.15. The area compression of the beam was 50 : 1, and the magnetic field required for Brillouin flow (less than 2 per cent scalloping) was 285 gauss.

As is shown in Figure A-1, a ball valve was positioned between the gun and the drift region which contained a doubly re-entrant cavity and a beam-analyzing mechanism. This valve is considered to be one of the most important parts of the analyzer because when it is closed, the drift tube can be opened to atmospheric pressure while the cathode remains in a region evacuated to a pressure of about 10^{-9} mm Hg. When the drift tube is evacuated, the valve is opened and the beam from the gun passes through the aperature in the ball to the beam-modulating and beam-analyzing region.

A. PROBE

The beam-analyzing mechanism shown at the left of Figure A-1 is shown again in Figure A-2 and also in the photograph in Figure A-3. Most of the electron beam was collected by the beam-collecting plate, which was carbonized to reduce the secondary electron ratio. A small portion, however,

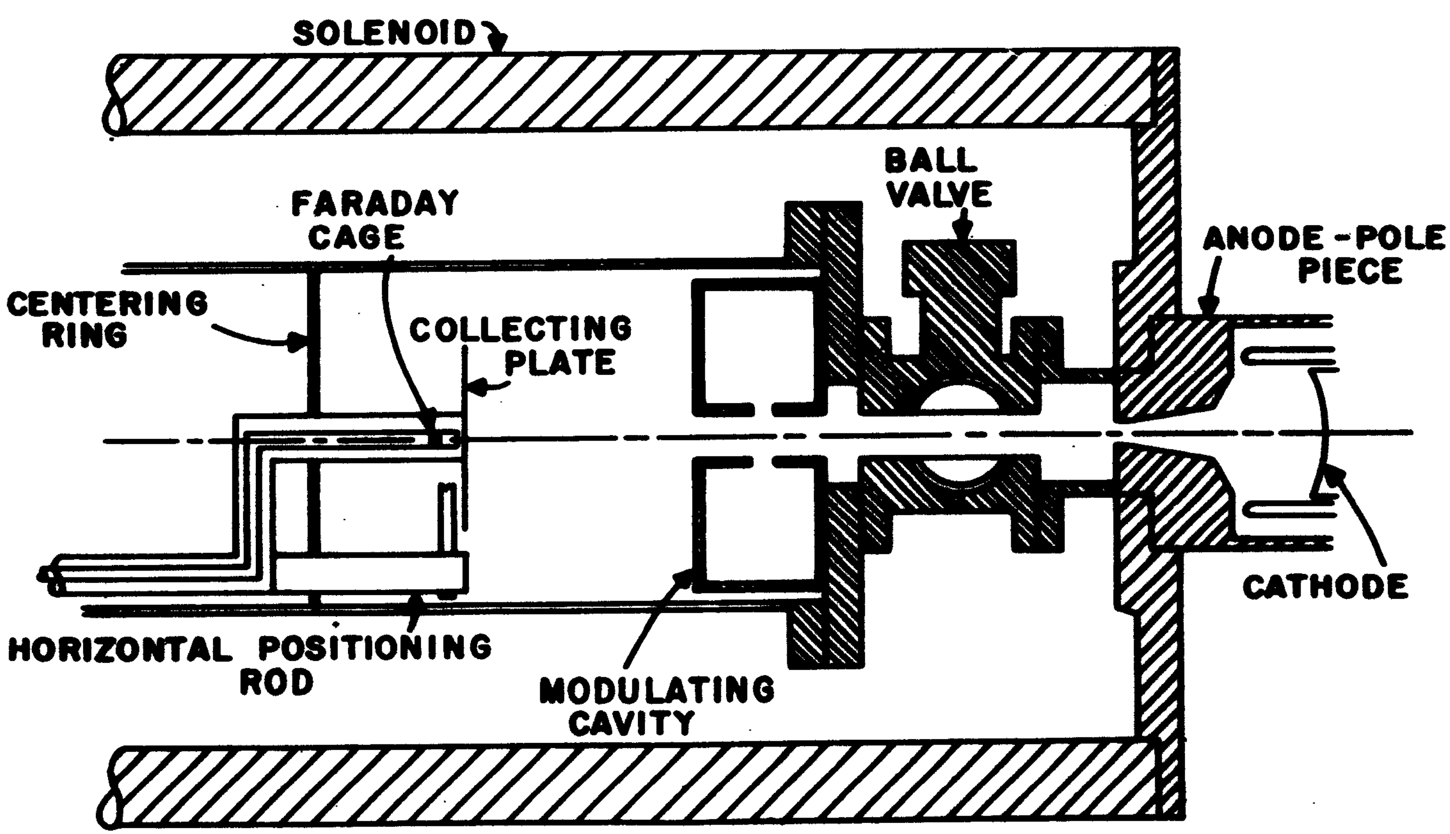

Figure A-1. Simplified Sketch of Beam Analyzer.

was allowed to pass through the 0.010-inch aperture in the center of the plate to a Faraday cage. The Faraday cage, in turn, was attached to the end of the center conductor of a nonresonant coaxial line, which proved to be valuable in measuring currents at frequencies from d-c to 6000 Mc/s. Since the distance between the Faraday cage and the beam-collecting plate was about 0.030 inch, the electron transit angle between the plate and the cage was less than 0.25 radians under normal operating conditions. The gap-coupling coefficient for the current under these conditions was unity, for all practical purposes, and that for velocity was zero. As is shown in Figure A-2b, a short portion of the coaxial line directly behind the beam-collecting plate was flexible, so that the plate could be moved with respect to the fixed part of the coaxial line. The reason for moving the plate was, of course, to make beam measurements at any point in a plane perpendicular to the axis of the beam.

The electron current from the cage went out through a coaxial feed-through in the bottom control rod to an indicating device outside the analyzer. The collecting plate was positioned in the plane perpendicular to the axis of the solenoid by rotations of the two control rods. As is shown in Figure A-2b, the plate could be moved horizontally by rotating the bottom rod. Vertical motion was produced in a similar manner by rotating the side rod. Teflon bearings, which were used to prevent binding between stainless steel parts, were attached to the back of the plate and slid on the lever arms attached to the side and bottom rods during horizontal and vertical motion. Although rotational motions were converted to translational motions in positioning the cage, they could be considered to be linear, since the distances moved were small compared to the length of the lever arms.

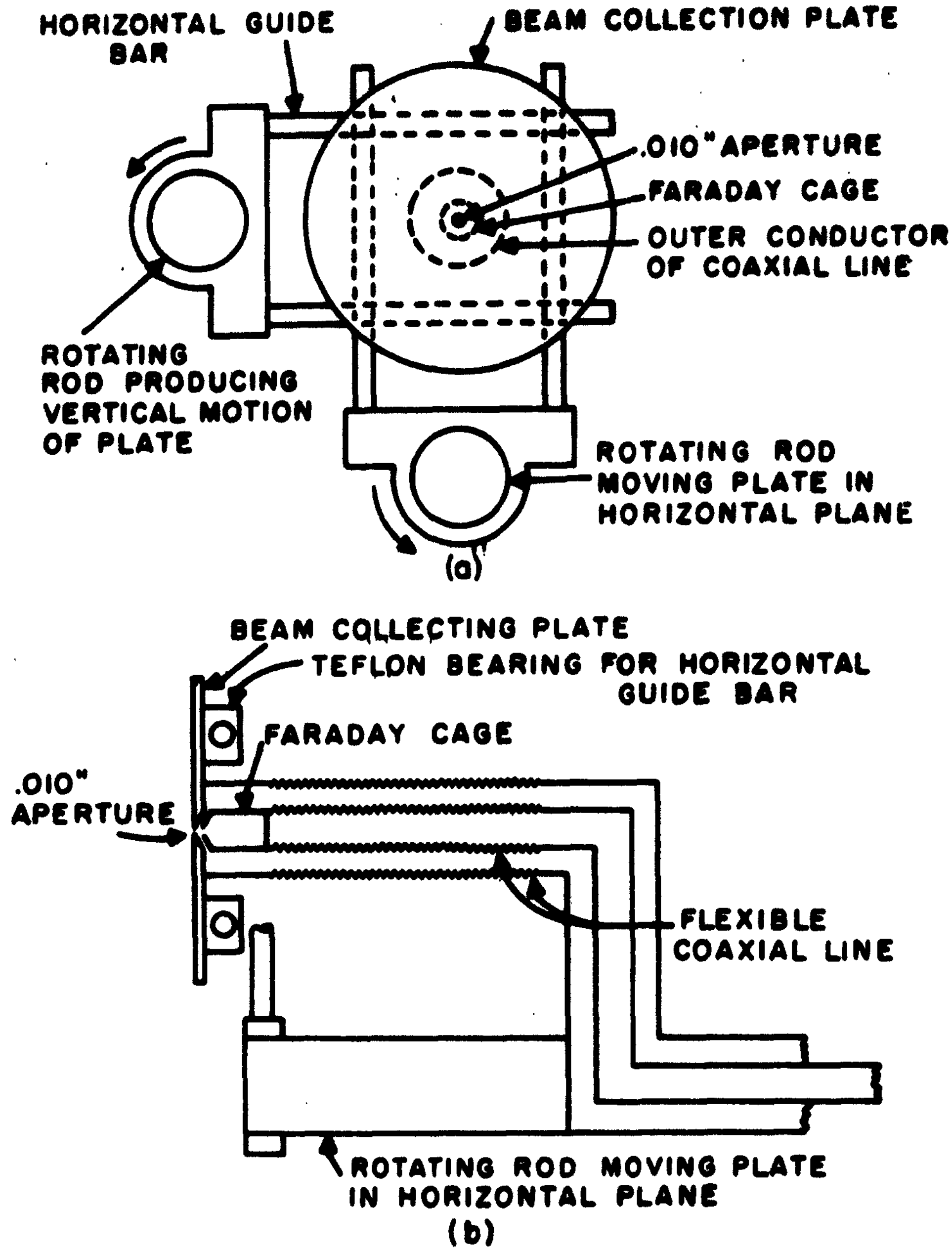

Figure A-2. (a) Simplified Sketch of Beam Scanner. (b) Simplified Sketch of Faraday Cage and Flexible Coaxial Line.

Figure A-3. Beam-scanning Mechanism.

The collecting plate and positioning rods are illustrated in Figure A-3. The disk shown behind the collecting plate and the lever arms was used to center the entire mechanism in the drift tube. Axial motion of the cage assembly was produced by moving the control rods through Veeco quick couplings.

Figure A-4 shows the control mechanism for the positioning rods. The scanning mechanism was moved axially by using the gear and rack arrangement shown in the figure. The angular position of the rods was adjusted by means of micrometers, the micrometer that set the horizontal position of the Faraday cage being equipped with a motor drive. Reversing switches caused the motor to sweep the cage back and forth across the beam automatically. To provide a voltage proportioned to the horizontal position of the cage, a ten-turn helipot was geared to the motor. This voltage was applied to the X input of an X-Y recorder and a voltage proportional to the r-f current component selected by the Faraday cage circuit was applied to the Y input of the X-Y recorder so that automatic plotting of current amplitudes as a function of position in the beam was possible.

B. CIRCUITRY

A block diagram of the circuit used for measuring the r-f currents received by the Faraday cage is shown in Figure A-5. The modulated beam was sampled by the beam-collecting plate with a .010-inch aperture in the center. The current passing through the aperture was collected by the Faraday cage and was taken out of the analyzer through the nonresonant coaxial line. At this point, a filter was used to select the harmonic to be analyzed. After the filtering process, a path was provided for d-c current to return

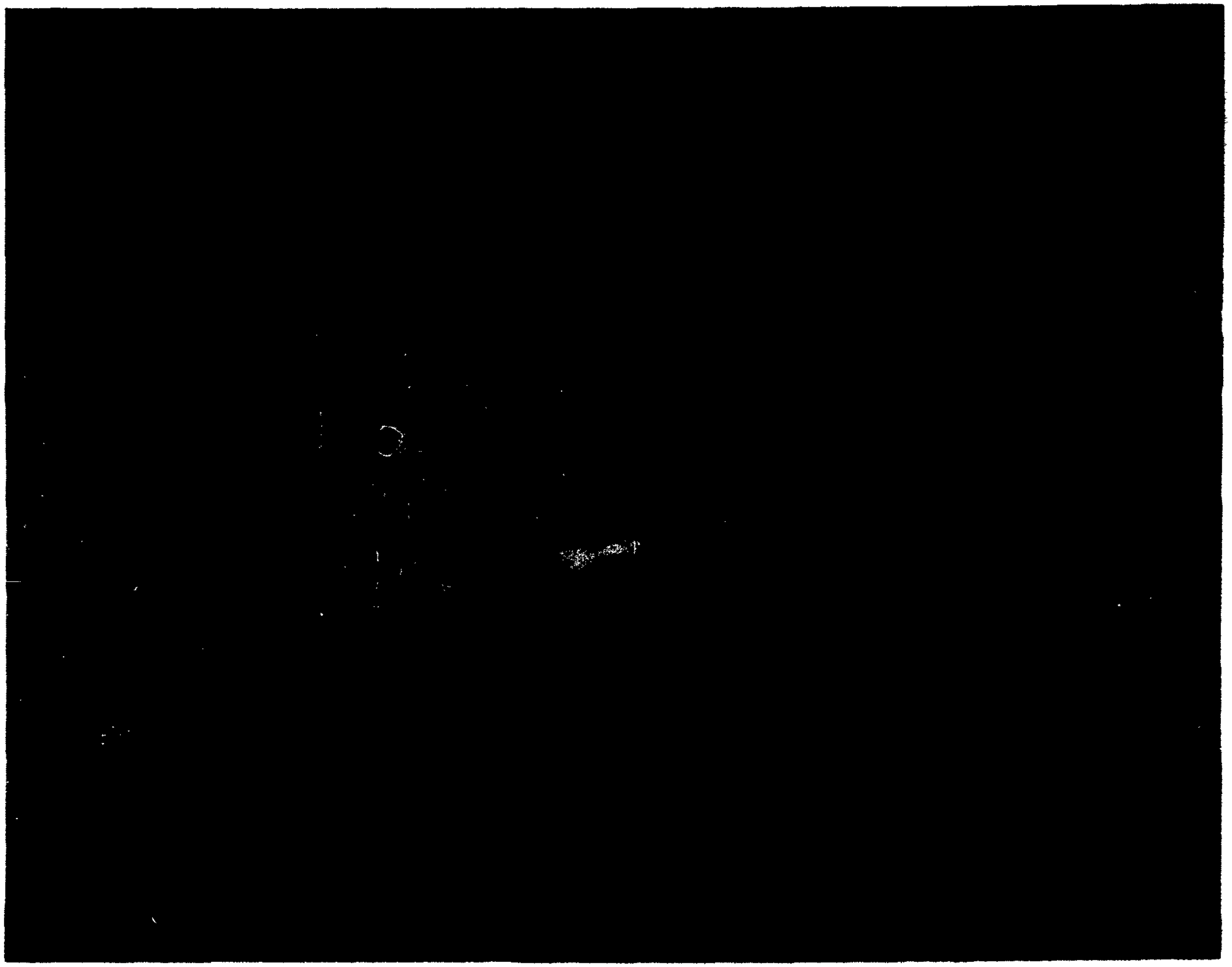

Figure A-4. Control-Rod Positioning Mechanism.

to ground, and in fact, a recorder was normally included in this circuit when measurements were being made of the fundamental r-f current component so that the shape of the average-current profile in the beam could be obtained simultaneously. Following the d-c current connection, a capacitor was inserted in the line to eliminate parallel d-c current paths, and a variable impedance was inserted to optimize the r-f signal amplitudes arriving at the crystal mixer.

A local oscillator is shown in the lower left-hand corner of Figure A-5 and was used to obtain a 30-Mc/s intermediate frequency from the crystal mixer. A filter and an isolator were used in the local-oscillator circuit to prevent interference from local-oscillator harmonics and to isolate the local oscillator from impedance changes occurring in the r-f current-sensing circuit.

A General Radio Type 1216-A unit i-f amplifier was used to amplify the 30 Mc/s intermediate frequency generated by the crystal mixer. Since the output voltage from the i-f amplifier was not directly proportional to the amplitude of the 30 Mc/s signal fed into the amplifier, a nonlinear circuit was devised, which compensated for the nonlinearities in the i-f amplifier. The amplitude of the output pulse from this linearizing circuit was therefore proportional to the amplitude of the 30 Mc/s signal and also proportional to the r-f current signal from the beam, since the crystal mixer was operated in a linear range.

Finally, the pulse from the linearizing circuit was amplified and fed into a circuit which generated a d-c voltage equal to the peak pulse voltage. This d-c voltage, which was then proportional to the r-f current signal from the beam, was amplified by a General Radio Type 1230-A d-c ampli-

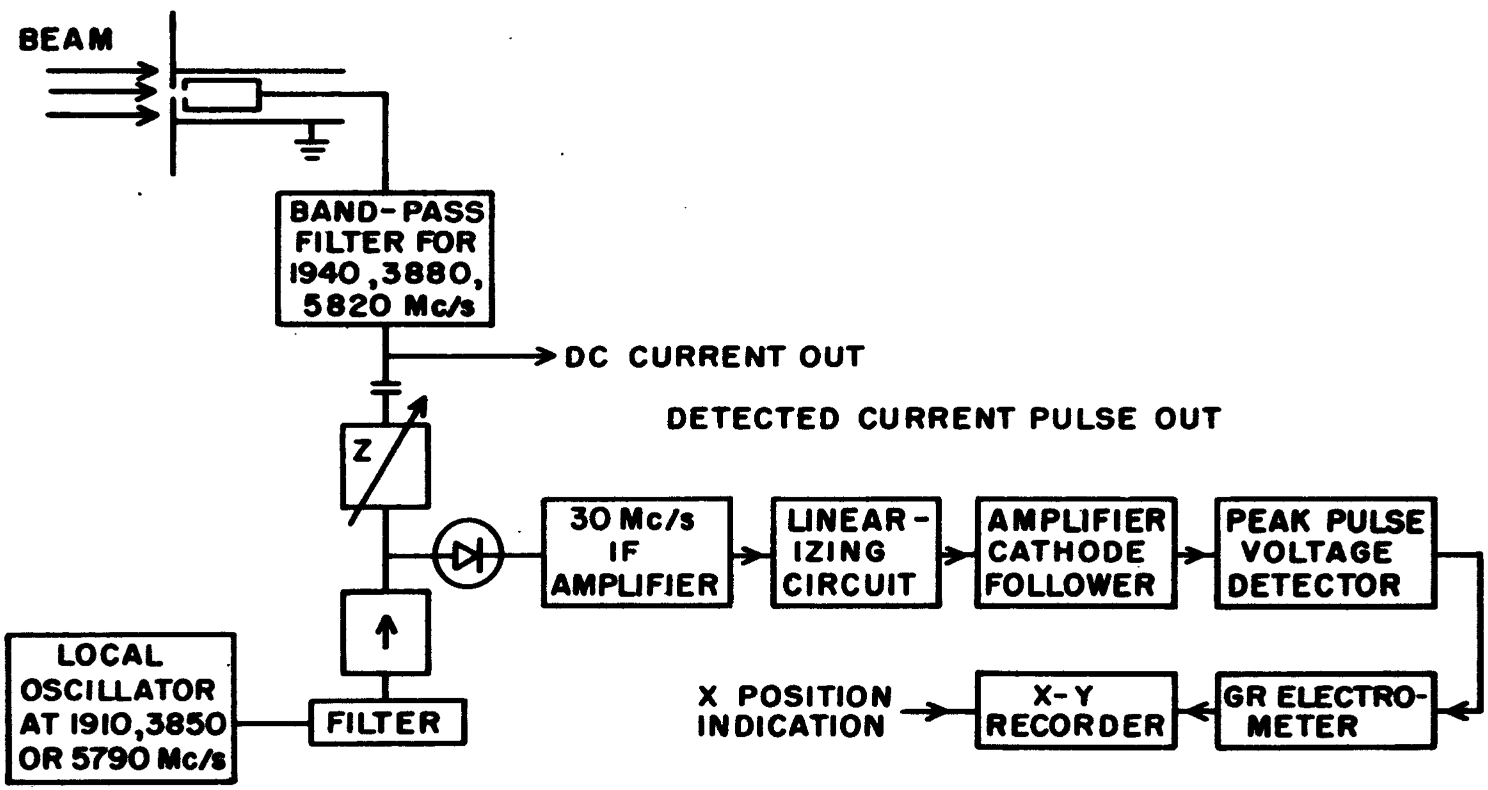

Figure A-5. Circuit Used in Detecting and Recording R-F Currents in Modulated Electron Beam.

fier and was applied to the Y input of an X-Y recorder. The voltage applied to the X input of the recorder was, as usual, proportional to the X position of the Faraday cage in the electron beam. As a result, by using the circuit shown in Figure A-5, the amplitude of the r-f current density in the beam could be recorded directly as a function of position in the beam.

GRAPHIC SYMBOLS FOR MICROWAVE SCHEMATIC DIAGRAMS

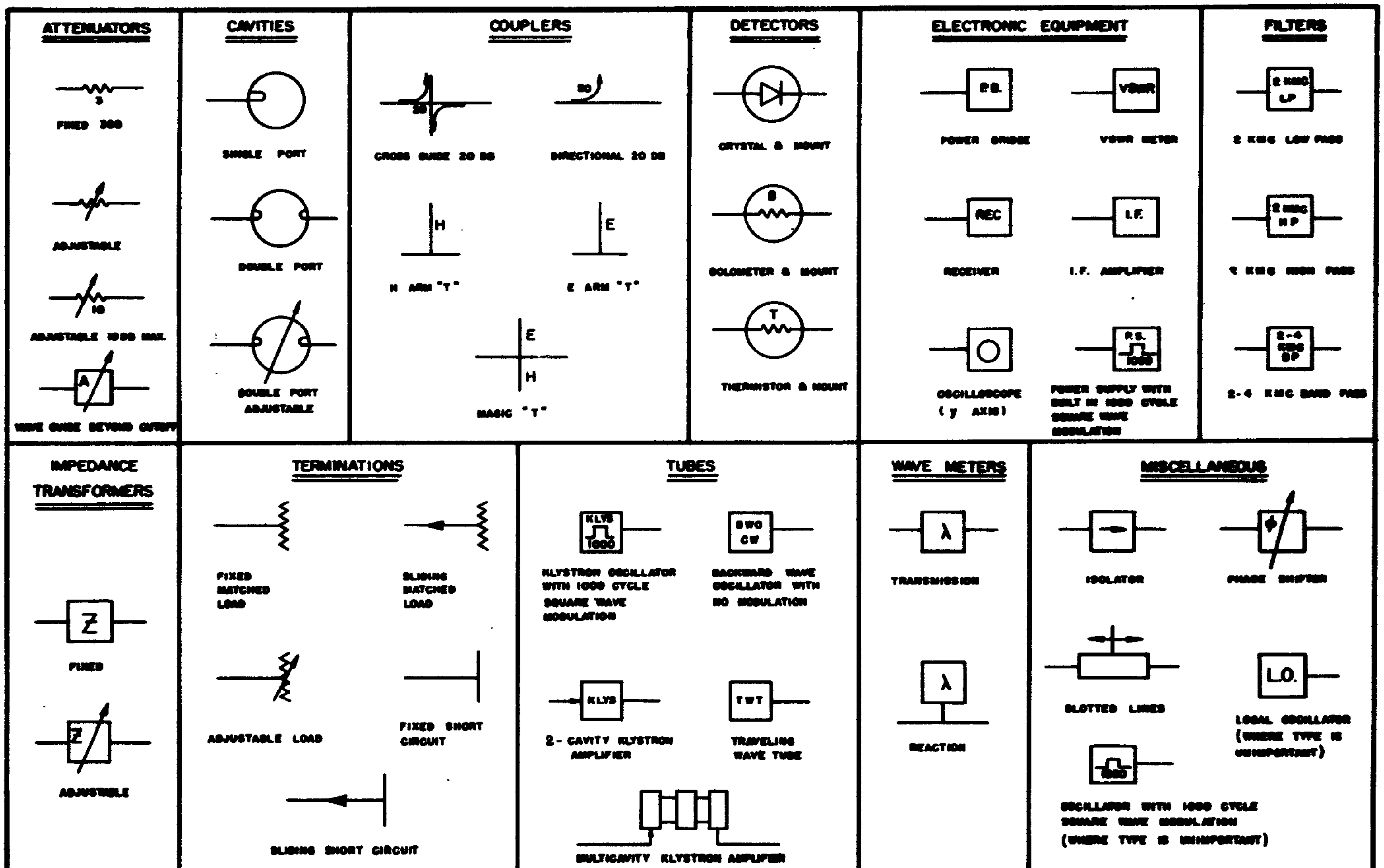

REFERENCES

1. A. S. Gilmour, Jr., "A Beam Tester for Studying the Characteristics of D-C and Velocity-modulated Electron Beams," Research Report EE 495, Cornell University, 1961.

2. D. D. Hallock, "Investigation on the Laminarity of Flow in a Magnetically Confined Electron Beam," Research Report EE 539, Cornell University, 1962.

3. A. S. Gilmour, Jr., "The Velocity Distribution in a Velocity-modulated Electron Beam from a Shielded Pierce Gun," Research Report EE 507, Cornell University, 1961.

4. W. W. Rigrod and J. A. Lewis, "Wave Propagation along a Magnetically Focused Cylindrical Electron Beam," Bell Sys. Tech. Jour., 33 (1954), pp. 399-416.

5. L. Brillouin, "A Theorem of Larmor and its Importance for Electrons in Magnetic Fields," Phys. Rev., 67 (1945), p. 260.

6. A. L. Samuel, "On the Theory of Axially Symmetric Electron Beams in an Axial Magnetic Field, Proc. I.R.E., 37 (1949), p. 1252.

7. C. C. Wang, "Electron Beams in Axially Symmetrical Electric and Magnetic Fields," Proc. I.R.E., 38 (1950), pp. 135-147.

8. M. Chodorow and L. T. Zitelli, "The Radio-Frequency Current Distribution in Brillouin Flow," I.R.E. Trans., ED-6 (1959), pp. 352-357.

9. D. K. Winslow, "The Current Distribution in Magnetically Focused Modulated Electron Beams," Rep. No. 380, Stanford Univ., Microwave Laboratory, Stanford, Cal., April 1957.

AN INVESTIGATION OF THE LAMINARITY
OF FLOW IN A MAGNETICALLY CONFINED ELECTRON BEAM

D. D. Hallock

School of Electrical Engineering
CORNELL UNIVERSITY
Ithaca, New York

RESEARCH REPORT EE 539

AN INVESTIGATION OF THE LAMINARITY OF FLOW IN A MAGNETICALLY CONFINED ELECTRON BEAM

D. D. Hallock

LINEAR BEAM MICROWAVE TUBES

Technical Report No. 19 — 15 September 1962

Published under Contract No. AF30(602)-2573
Rome Air Development Center, Griffiss Air Force Base, New York

ACKNOWLEDGMENTS

The author would like to thank Prof. G. C. Dalman for suggesting and directing this study, and particularly Prof. A. S. Gilmour, Jr., who offered many suggestions and helped provide an insight into the dynamics of electron beams.

He would like to acknowledge the technical assistance of Messrs. P. A. Lumbard and J. D. Berry; the photographs used in this report were taken by Mr. Lumbard. He also thanks Mr. M. M. McCarty for the skillful machining of the parts used in this experiment.

The support of the Air Force for this research under contract #AF30 (602)-2573 is acknowledged.

CONTENTS

ABSTRACT

A study of the electron flow in a Brillouin beam was made, which yielded information that provided an insight into the electron behavior in a medium-power Brillouin beam. It was shown that the beam can display a high degree of laminarity at a beam voltage of 5000 v.

The trajectory equation of the outer edge electron in the laminar model of the beam was linearized and shown to give results in good agreement with the experimental observations, when the focusing field was less than twice the Brillouin field. It was also shown that the beam can be focused at the calculated Brillouin field within the limits of experimental error. The differences between the theoretical predictions and the experimental observations, which arose from limitations either of the experimental apparatus or the theory, are discussed. The effects of thermal velocities are considered, particularly at low beam voltages.

I. INTRODUCTION

Since the advent of the linear beam microwave tube in World War II, the motion of electrons in cylindrical electron beams has been the subject of several theoretical and experimental studies, because a knowledge of the electron motion in the beam is important in formulating a r-f theory for the modulated beam. The simplest theories describing the velocity-modulated beam assume a beam that is laminar, free from any d-c axial variation, and with constant charge density in the radial and angular directions. While this is a highly idealized model of the beam, it is very simple and has led to theoretical predictions which have been subsequently verified experimentally.[1]

The purpose of this study was to determine the degree of laminarity of the beam from an STL-100 electron gun.* This would serve as a basis for interpreting future r-f measurements made with this beam and provide a basic insight into the electron behavior in a medium-power beam from a shielded Pierce gun. Although much work has been done on electron beams, most of it has been under at least one of the following restrictive conditions: (1) focus fields much higher than the calculated Brillouin[2] field, (2) low beam voltage, (3) low current density. Very few detailed studies have been made of the electron flow in the medium- and high-power beams, which are coming into more general use in present-day linear beam tubes. Some work in this direction was done by Gilmour,[3] who reported that the STL-100 beam seemed to show a high degree of laminarity. He discovered certain anomalies, however, which he could

*This was one of five donated to the School of Electrical Engineering by the Sperry Gyroscope Company.

not explain. His studies served as a basis for this investigation, and an explanation of these anomalies is offered in this report.

Chapter II gives the trajectory equation of the outer-edge electron in a laminar beam. The region of interest in this study was a beam focused by a magnetic field near the calculated Brillouin flow value. Since, in this region the beam scalloping was moderate, it was possible to linearize the trajectory equation to obtain a solution that was much more amenable to calculation than the original equation.

The method of measuring the data is described in Section III A. It is shown that the most rapid method of determining the scallop wavelength is from measurements of the variation in current density on the beam axis. In Sections III B-III E the experimental results are compared with the predictions of the linearized laminar theory. The close agreement between the calculated and observed values of the beam characteristics is pointed out.

In Section III F the effect of thermal velocities on the beam are discussed. These effects account for the diffuse beam edge, but are otherwise of no great importance.

The beam analyzer used in this investigation is described in Appendix A. While this analyzer has been described by Gilmour,[3] a description is included here for completeness and to describe improvements that have been made in the system since his description.

An attempt was made to track electrons in the beam by perturbing the trajectories of certain electrons at the cathode to "label" them. Because the detection apparatus was not sensitive enough, the goals of this study were not met. Many observations were made and a fuller under-

standing of the problem was obtained, however. A discussion of the perturbation experiment, and an analysis of the results are given in Appendix B.

II. THEORETICAL ANALYSIS

The theory of the electron motion in a laminar electron beam is presented as a basis for discussion of the experimental observations. In general the approach used follows the one used by Wang.[4]

A. DERIVATION OF TRAJECTORY EQUATION

In the laminar model the electron beam is described as an infinite number of concentric, cylindrical shells. An electron is injected into a given shell at the plane of origin (the cathode) and remains in that shell until the beam is terminated. Under these conditions any electron trajectory may be described in cylindrical co-ordinates by

$$r_i(z) = \mu\, r(z) \quad , \tag{1}$$

where r is the radius of the outer-edge electron shell as shown in Figure 1, and r_i is the radius of any internal electron shell. Since for laminar flow, μ is a constant, only the trajectory of the outer edge electron shell need be determined to describe the electron motion in the beam completely.

The Hamiltonian function in cylindrical co-ordinates is;

$$H = \frac{1}{2} m \left(\dot{r}^2 + \dot{z}^2 + r^2 \dot{\theta}^2\right) - e\phi = 0 \quad , \tag{2}$$

which expresses the fact that the system is conservative. The equation of motion for the electron beam can be obtained by using the three Hamiltonian equations:

$$\frac{dP_r}{dt} = -\frac{\partial H}{\partial r} \quad , \qquad \frac{dP_z}{dt} = -\frac{\partial H}{\partial z} \quad , \qquad \frac{dP_\theta}{dt} = -\frac{\partial H}{\partial \theta} \quad , \tag{3}$$

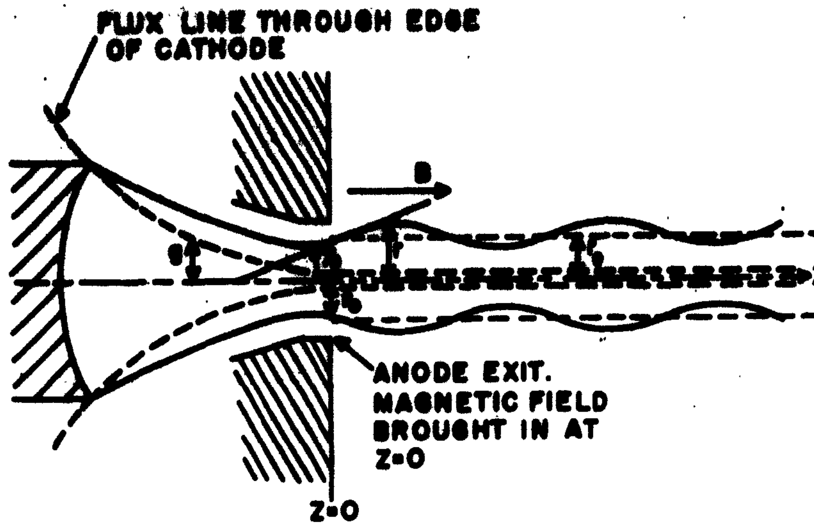

Figure 1. Diagram of Electron Beam Showing Some of Parameters Used in Deriving Laminar Theory.

where P_r, P_z, and P_θ are the generalized moments.

Since B, the magnetic field, is represented by a solenoidal vector, it can be expressed as the curl of a magnetic vector potential, A. Because of the axial symmetry of the magnetic field, only the A_θ component of the vector potential is required. The magnetic field components may be written as

$$B_z = \frac{1}{r} \frac{\partial_r A_\theta}{\partial r} \quad , \quad B_r = - \frac{\partial A_\theta}{\partial z} \quad . \tag{4}$$

The velocities may be eliminated from H by using

$$P_r = m\dot{r} \ , \tag{5a}$$

$$P_z = m\dot{z} \ , \tag{5b}$$

$$P_\theta = m r^2 \dot{\theta} - e r A_\theta \ . \tag{5c}$$

The Hamiltonian then becomes

$$H = \frac{1}{2m} \left[P_r^2 + P_z^2 + \left(\frac{P_\theta}{r} + e A_\theta \right)^2 \right] - e\phi = 0 \ . \tag{6}$$

The operations indicated in Equation (3) are performed on this equation to obtain the following equations of motion:

$$r = r\,\dot{\theta}^2 - \eta r\,\dot{\theta}\,B_z + \eta\,\frac{\partial\theta}{\partial r} \quad , \tag{7a}$$

$$z = \eta r\,\dot{\theta}\,B_r + \frac{\eta\partial\phi}{\partial z} \quad , \tag{7b}$$

$$\frac{d}{dt}\,(r^2\,\dot{\theta} - \eta r\,A_{\theta}) = 0 \quad , \tag{7c}$$

where η is the electron charge-to-mass ratio, and where it has been assumed that the potential ϕ is axially symmetric ($\partial\phi/\partial\theta = 0$). Equation (7c) may be integrated directly to yield

$$r^2\,\dot{\theta} = \eta\,(r\,A_{\theta} - r_c\,A_{\theta_c}) \quad , \tag{8}$$

where A_{θ_c} is a measure of flux through the cathode. For the case studied, the magnetic field was independent of r and z in the drift region; therefore

$$A_{\theta} = \frac{r}{2}\,B_z \tag{9}$$

from Equation (4), and Equation (8) becomes

$$\dot{\theta} = \omega_L\left(1 - \frac{g^2}{r^2}\right) \quad , \tag{10}$$

where $\omega_L = \eta B/2$, the Larmor angular frequency, and g is the radius of the flux line through the edge of the cathode at the plane where θ is to be determined as shown in Figure 1.

The term $\partial\phi/\partial r$ of Equation (7a), which is the radial component of the electric field in the presence of space charge, must still be determined. From Poisson's equation,

$$\text{div}\,E = \frac{1}{r}\,\frac{d(r\,E_r)}{dr} = \frac{\rho}{\epsilon_0} \quad , \tag{11}$$

the radial field strength E_r within the beam ($\mu \leq 1$) is obtained. This is based on the assumption that the axial field that is due to axial variations in charge density arising from scalloping of the beam can be disregarded. Since $B_r = 0$ for this case, this assumption also means that $\ddot{z}$ will be very small and need not be considered.

Integrating Equation (11) yields

$$E_r = \frac{\rho r}{2\epsilon_0} \quad . \tag{12}$$

The actual space-charge density, ρ, cannot be exactly specified in the beam. A good approximation is obtained by writing

$$\rho = \frac{I_0}{\pi r^2 u} \quad , \tag{13}$$

where I_0 is the beam current and u is the z-directed beam velocity; ρ and u should be independent of r when this approximation is used. (From observations on the beam cross section it has been seen that ρ is indeed very nearly independent of r.) For the Brillouin beam ($g = 0$), Wang[4] has shown that u is independent of the beam radius and has the value,

$$u = \sqrt{2 n (V_b + \phi_s)} \quad ,$$

where V_b is the potential at the beam edge, and ϕ_s is due to the negative potential depression at the beam center caused by the space charge in the beam. Gilmour[3] has tabulated u as a function of the ratio of beam radius to drift-tube radius for a beam of microperveance one.

Using Equations (10), (12), and (13) in Equation (7a) gives

$$\ddot{r} = -r\left[\omega_L^2 - \left(\omega_L \frac{g^2}{r^2} - \dot{\theta}_c\right)^2\right] + \frac{\eta I_0}{2\pi \epsilon_0 r u} \quad . \tag{14}$$

By writing $R = r/a$ and $R_g = g/a$, where

$$a = \frac{1}{\omega_L}\sqrt{\frac{\eta I_0}{2\pi \epsilon_0 u}} \quad , \tag{15}$$

one finds that Equation (14) becomes

$$\ddot{R} + \omega_L^2 \left[R\left(1 - \frac{R_g^4}{R^4}\right) - \frac{1}{R}\right] = 0 \quad . \tag{16}$$

This equation describes nonlinear oscillations about an equilibrium radius R_e at which $\ddot{R} = 0$. After some manipulation, we get

$$R_e = \left[\frac{1}{2} + \frac{1}{2}\left(1 + 4\, R_g^4\right)^{\frac{1}{2}}\right]^{\frac{1}{2}} \quad . \tag{17}$$

It is seen that for the Brillouin beam ($g = 0$),

$$R_e = 1 \quad ,$$

or

$$r_e = a \quad .$$

Thus the normalizing term specified in Equation (15) is the equilibrium radius for the Brillouin beam.

B. SCALLOP WAVELENGTH FROM LINEARIZED TRAJECTORY EQUATION

Equation (16) is not very useful for calculations in the form given. For this study, however, only values of the focusing field near that value that produces a Brillouin beam with no radial oscillations are studied. The

radial deviations from the equilibrium radius should therefore be small, and the normalised beam radius may be written as

$$R = R_e (1 + \delta) \quad ,$$

where δ is small, such that

$$\frac{1}{1 + \delta} = 1 - \delta \quad ,$$

$$\frac{1}{(1 + \delta)^3} \approx 1 - 3\delta \quad .$$

Then Equation (17) becomes

$$\ddot{\delta} + \omega_L^2 \; \delta \left[1 + \frac{3 R_g^4}{R_e^4} + \frac{1}{R_e^2} \right] = \left[\frac{R_g^4}{R_e^4} + \frac{1}{R_e^2} - 1 \right] \omega_L^2 \quad .$$

From the definition of R_e given in Equation (17), it is easily shown that the term on the right-hand side is equal to zero, so that

$$\ddot{\delta} + \omega_L^2 \; \delta \left[1 + \frac{3 R_g^4}{R_e^4} + \frac{1}{R_e^2} \right] = 0 \quad . \tag{18}$$

Some predictions of the beam behavior for a few special cases can be made on the basis of this equation. The simplest case is that of the perfect Brillouin beam for which Equation (18) becomes

$$\ddot{\delta} + 2 \, \omega_L^2 \; \delta = 0 \quad . \tag{19}$$

This equation describes radial oscillations at the scallop frequency $\omega_s = \sqrt{2}\,\omega_L$. When ρ is calculated from Equation (13) using the equilibrium radius as given by Equation (15), then

$$\omega_s = \sqrt{2}\,\omega_L = \omega_p \quad , \tag{20}$$

where ω_p is the plasma frequency, and $\omega_p = \left(\frac{\eta\rho}{\epsilon_o}\right)^{\frac{1}{2}}$. It should be noted that Equation (20) has been obtained without the restriction that the beam does not scallop. The amplitude of the beam scallops cannot be very large, however, or the restrictions placed on δ in deriving the linearized Equation (18) will not hold.

The scallop wavelength can be readily obtained from Equation (20):

$$\lambda_s = \frac{2\pi u}{\sqrt{2}\,\omega_L} = \sqrt{2}\,\frac{2\pi u}{\omega_c} = \sqrt{2}\quad \lambda_c \quad , \tag{21}$$

where λ_c is the cyclotron wavelength, and $\omega_c = \eta B$ is the cyclotron frequency.

The opposite extreme from the case $g = 0$ is when $R_g/R_e = 1$. This is analogous to the case of confined flow in which all the focusing flux threads the cathode, and very high magnetic fields are used. It can readily be shown from Equation (17), however, that the condition $R_g = R_e$ can only be met at $R_e = 0$, which is not a physically realizable case. The problem arises from the term $1/R$ in Equation (16), which represents the space charge of the beam. Because of this term, the equilibrium radius, R_e, of the beam in the drift region must be larger than the radius of the flux line threading the edge of the cathode. This expansion of the beam allows the electron trajectories to encircle more magnetic flux in the drift region than at the cathode, so that the inward-directed Lorentz force can balance the outward-directed space-charge force.

For the case of zero space charge,

$$\begin{aligned} \omega_s &= \omega_c \quad , \\ \lambda_s &= \lambda_c \quad . \end{aligned} \tag{22}$$

When the space charge of the beam is considered, Equation (22) serves as an asymptotic limit to the scallop wavelength as the magnetic field is increased.

For those cases where some flux threads the cathode, the scallop wavelength will be intermediate between λ_c and $\sqrt{2}\,\lambda_c$. The value predicted by the theory must be calculated for the parameters of the system being studied, where

$$\omega_s = \omega_L \left[1 + \frac{3R_g^4}{R_e^4} + \frac{1}{R_e^4} \right]^{\frac{1}{2}} , \tag{23a}$$

$$\lambda_s = 2\,\lambda_c \left[1 + \frac{3R_g^4}{R_e^4} + \frac{1}{R_e^2} \right]^{\frac{1}{2}} , \tag{23b}$$

and R_e is given by Equation (17). It should be noted that these equations are still subject to the condition that $\delta \ll 1$ under which the linearized equation was derived.

C. MAGNITUDE OF BEAM SCALLOPS

In a practical tube design, the magnitude of beam scallops is of great importance. This has been determined by previous workers, but not in the form best suited to this study. The values of R_{max} and R_{min} can be obtained by integrating Equation (16). If this equation is multiplied by $2\dot{R}$ it can be integrated directly to yield

$$\dot{R}^2 + \omega_L^2 \left[R^2 + \frac{R_g^4}{R^2} - 2 \ln R \right] = C \quad ; \tag{24}$$

C is a constant that is evaluated from the boundary conditions at the plane of injection into the focusing field. In this study this plane is referred to as the anode exit.

It has been observed experimentally that the case of zero amplitude scallops can almost be obtained with the beam from the STL-100 electron gun. This suggests that the radial velocity at the anode exit is zero or $\dot{R}_o = 0$. Scalloping does occur, however, when the magnetic field is set either above or below the value for zero amplitude scallops. Since $\dot{R}_o = 0$, this corresponds to the case $R_o \neq R_e$, which is to be expected, since R_e is a function of the magnetic field. The boundary conditions can then be written as

$$R_o = A\, R_e \quad , \tag{25}$$

$$\dot{R}_o = 0 \quad ;$$

then

$$C = \omega_L^2 \left[R_o^2 + \frac{R_s^4}{R_o^2} - 2 \ln R_o \right] \quad ,$$

and

$$(\dot{R})^2 + \omega_L^2 \left[R_o^2 + \frac{R_g^4}{R_o^2} \left(\frac{R_o^2}{R^2} - 1 \right) - 2 \ln \frac{R}{R_o} \right] = 0 \quad . \tag{26}$$

At R_m, where the subscript m denotes either a maximum or a minimum of the beam radius, $\dot{R} = 0$. For the case $R_g = 0$, the calculation of R_m is rather straightforward:

$$R_m^2 - R_o^2 - 2 \ln \frac{R_m}{R_o} = 0 \quad . \tag{27}$$

When $A = 1$ in Equation (25), $R_m = R_e$ and there is no scalloping. If $A \neq 1$, there are two solutions, one of which is $R_m = R_o$. If $A > 1$,

$$R_{max} = R_o \quad ,$$

$$R_{min} = A^2 R_e^2 - \alpha^2 = A^2 - \alpha^2 \quad ;$$

since $R_e = 1$ and Equation (27) gives

$$\alpha^2 = \ln \frac{A^2}{A^2 - \alpha^2} \quad . \tag{28}$$

For the case of $A < 1$,

$$R_{min} = R_o \quad ,$$

$$R_{max} = A^2 + \alpha^2 \quad ,$$

where

$$\alpha^2 = \ln \frac{A^2 + \alpha^2}{A^2} \quad . \tag{29}$$

In each of these cases,

$$\alpha^2 = R^2_{max} - R^2_{min} = \ln \frac{R^2_{max}}{R^2_{min}} \quad . \tag{30}$$

When $R_g \neq 0$, the calculation of R_m becomes more difficult. It is sufficient for this study to observe the effect on the scallop amplitude of small amounts of flux threading the cathode. From Equation (26),

$$R^2_m - R^2_o + \frac{R^4_g}{R^2_o} \left(\frac{R^2_o}{R^2_m} - 1 \right) - 2 \ln \frac{R_m}{R_o} = 0 \quad . \tag{31}$$

It is readily seen that the value $R_m = R_o$ is still a solution for Equation (31). Then Equation (31) may be written as

$$R^2_{max} - R^2_{min} + \frac{R^4_g}{R^2_{min}} \left(\frac{R^2_{min}}{R^2_{max}} - 1 \right) = \ln \frac{R^2_{max}}{R^2_{min}} \quad . \tag{32}$$

This requires that for the same difference, $R^2_{max} - R^2_{min}$, the addition of cathode flux causes the ratio R_{max}/R_{min} to decrease. This means that the

percentage of scalloping decreases, but that the average radius (or equilibrium radius) increases. It has previously been shown that the effect of cathode flux is to increase the equilibrium radius over the Brillouin radius. Thus the effect of flux threading the cathode is to decrease the scallop amplitude.

III. CALCULATIONS AND EXPERIMENTAL RESULTS

A. METHODS OF TAKING DATA

The data for this experiment were obtained using the electron beam analyser described in Appendix A. Because of the construction of the analyzer, it was not possible to obtain data closer than at a plane 6.2 inches from the anode exit. Measurements were therefore taken in a drift region from 6.2 inches to 20 inches from the anode exit. This restriction caused some uncertainties about the behavior of the beam immediately after leaving the anode exit, which are discussed later in the text. In general, however, the beam behavior could be adequately measured in the region available. Figure 20 shows some typical data with the beam cross section as a function of axial position for several values of magnetic field. The beam diameter obtained from data such as are shown in Figure 20 are presented in Figure 2 for five values of magnetic field. This diameter was

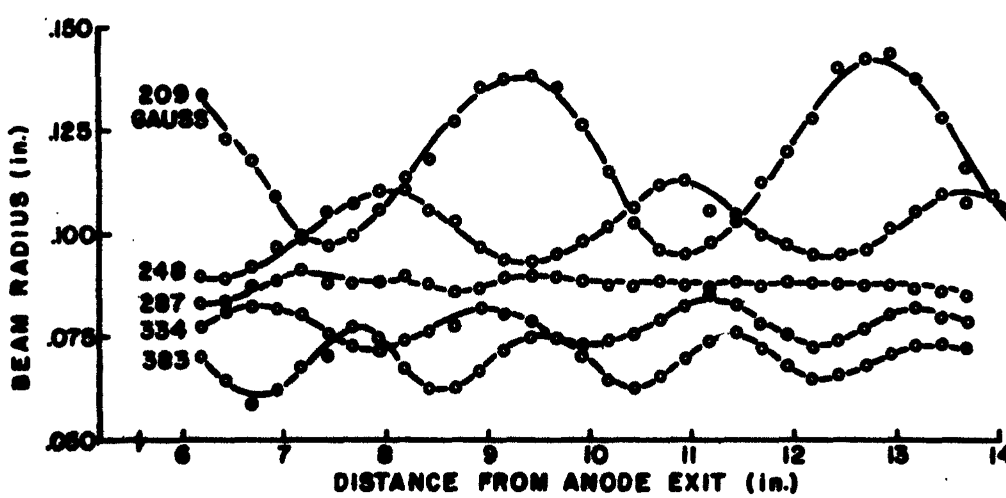

Figure 2. Beam Radius Including 95 Per Cent of the Beam Current versus Axial Position.

measured at the value of current density that was one-third the current density at the center of the cross section. Detailed measurements on several cross sections showed that this method of measuring the beam diameter yielded a value that included 95 per cent of the beam current within about 1 per cent tolerance.

This method yielded very good results on the beam diameter, but was very tedious for determining the scallop wavelength for many values of the focusing field. By measuring the variation in current density on the axis, one could obtain the scallop wavelength much more easily.

Plots showing the current density variation on the axis are shown in Figure 3. A unit of J_o in this plot is the current density on the axis when the beam is focused by the Brillouin field. Figure 3 is a direct reproduction of data taken on the x-y recorder, on which all data were recorded. It is apparent that it was easier to measure the scallop wavelength from these plots than to reduce the data as required for Figure 2.

B. CALCULATIONS OF THE BRILLOUIN FOCUSING FIELD

To calculate the Brillouin field,* the current, voltage, and beam radius must be accurately known. The beam radius is one of the most difficult parameters of the beam to define because of the finite slope of the beam edge, which makes it necessary to choose some value of radius arbitrarily and define it as the beam "edge." For Figure 2 the beam diameter including 95 per cent of the current was chosen. With this value, the radius of the nonscalloping Brillouin beam was .088 in. Since the beam

---

*In this study the term Brillouin field will refer to the value of focusing field that produced the minimum scalloping on the Brillouin beam.

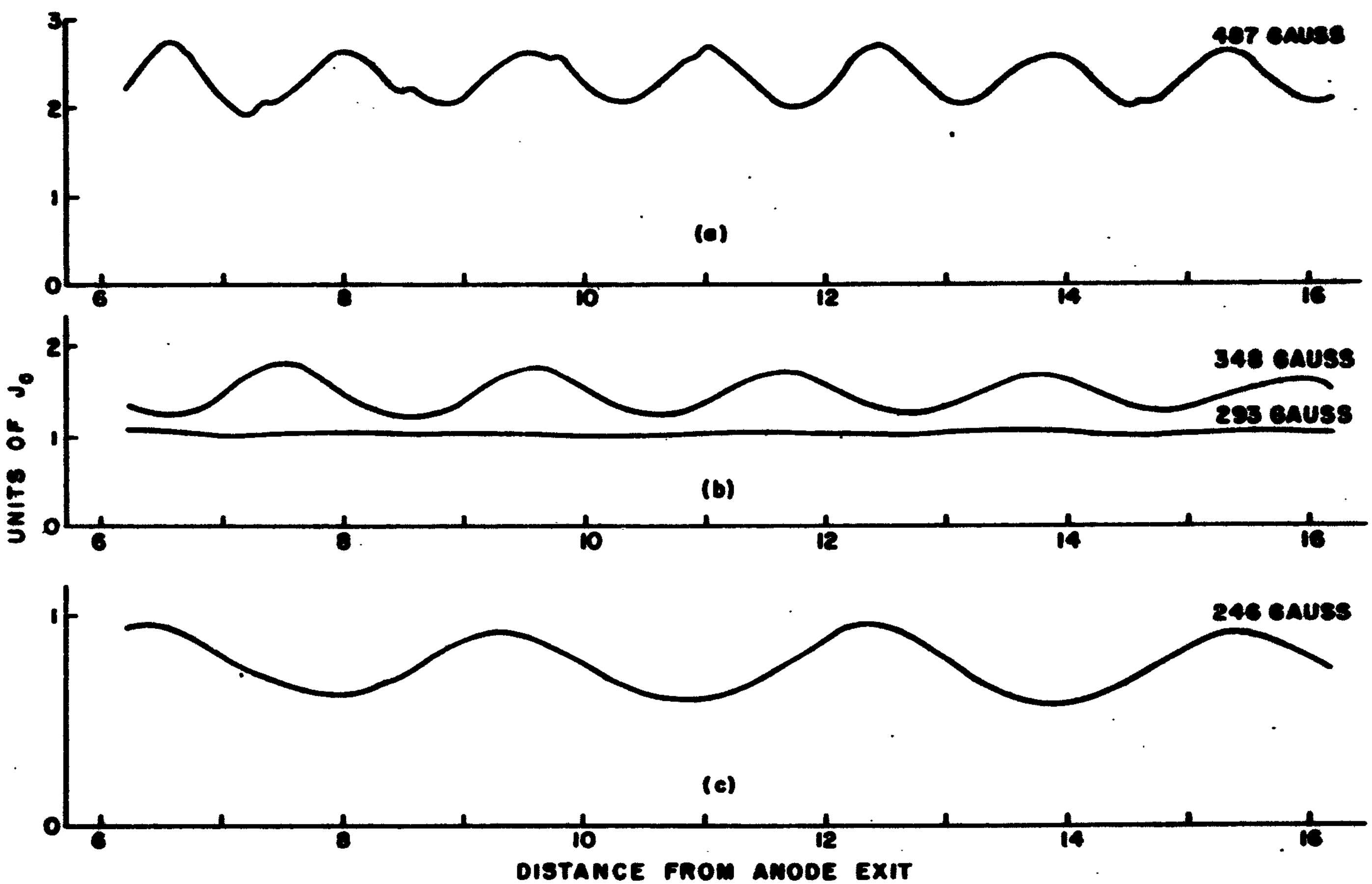

Figure 3. Current Density on the Beam Axis versus Axial Position. (The unit of J_o is the current density on the axis when there is no scalloping.)

current and voltage were known, this made it possible to calculate the Brillouin field using the equation derived by Pierce[5]:

$$I_o = 1.45 \times 10^6 B^2 V_o^{1/2} r^2 \quad \text{(mks)} \quad . \tag{33}$$

For this calculation, the effective voltage, $(V_{eff})^{1/2} = .95 (V_o)^{1/2}$, was used to allow for the depression in potential at the beam center. This correction was calculated by Gilmour[3] for the perveance and the drift tube size used. With

$I_o = .407$ a

$V_o = .5000$ v

$r = .088$ in. ,

the calculated value of magnetic field was

B = 297 gauss.

The amplitude of the beam scalloping was less than 5 per cent over a range of focusing field from 287 to 293 gauss. This indicated an experimental value of the Brillouin field of 290 gauss. This is within 2.4 per cent of the theoretical value, which is excellent agreement with the theory, in view of the assumption made in the calculation. Because of this agreement and the limitation on the accuracy of the calculation, a value of 290 gauss is used for the Brillouin field in the following discussion.

Previous experimenters have reported that much higher fields than the calculated Brillouin value were required to focus the beam.[6,7,8] Brewer,[6] reported that fields 10-20 per cent greater than the calculated

Brillouin value were required to obtain minimum scalloping. He also noted the presence of a translaminar stream of electrons in his beam caused by aberrations in the anode of the gun. In the beam studied, however, there was very little translaminar motion detected. This suggests that significant amounts of translaminar motion in the beams studied in previous experiments made it necessary to use focusing fields higher than the calculated Brillouin field. This would mean that the optics of the STL-100 electron gun are much better than those usually encountered in electron guns, so that the entrance conditions at the anode exit approximate the theoretical model more closely than in previous experiments, resulting in a more nearly laminar beam.

C. EQUILIBRIUM BEAM RADIUS

In Figure 4 the equilibrium radius, r_e, is plotted as a function of magnetic field, using Equation (17). In these calculations, and in all others in this study, the ratio B_c/B (where B_c is the flux through the cathode) was assumed to be constant for all values of magnetic field, a valid assumption if the shielding material over the electron gun saturated uniformly. In practice B_c/B was probably not constant, but over the narrow range of magnetic field used, this was a reasonable approximation.

When the ratio B_c/B was constant, the term R_g, which accounted for flux through the cathode, could be evaluated in terms of the beam parameters:

$$R_g^4 = \frac{g^4}{a^4} = \frac{r_c^4}{a^4}\left(\frac{B_c}{B}\right)^2 = r_c^4\left(\frac{B_c}{B}\right)^2 B^4\left(\frac{\eta\epsilon_o \pi u}{2 I_o}\right)^2 .$$

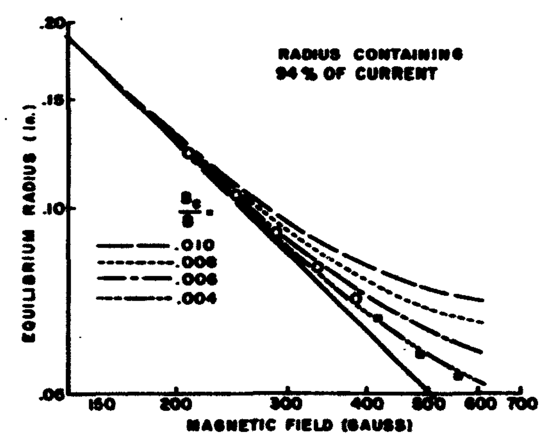

Fig. 4. Equilibrium Radius as Function of Magnetic Field When Small Amount of Flux Threads Cathode.

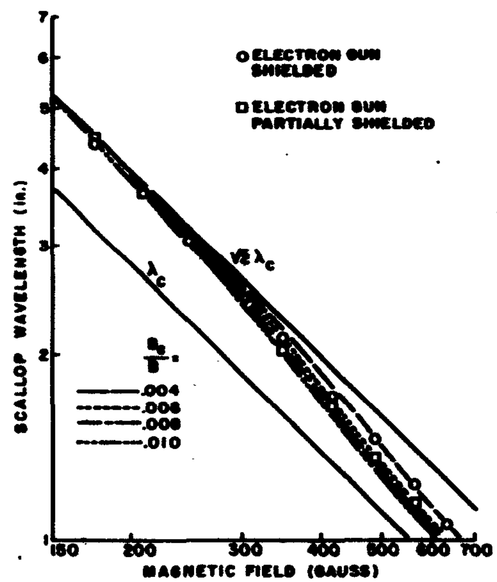

Fig. 5. Scallop Wavelength Determined from Current Density Variation on Beam Axis Compared with Laminar Theory.

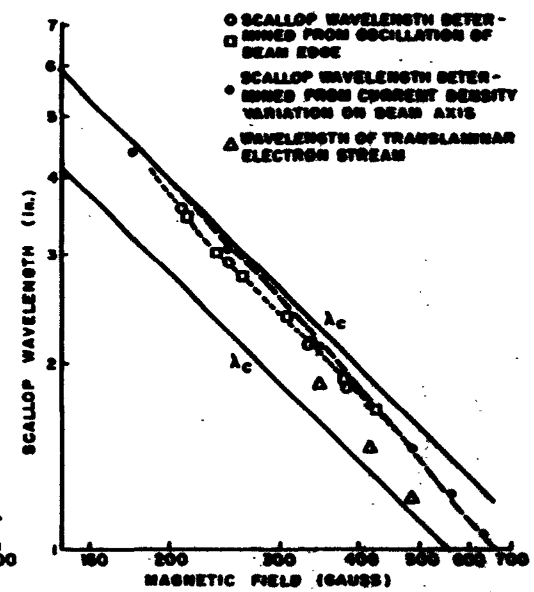

Fig. 6. Comparison of Scallop Wavelength Determined from Beam Edge and Axial Current Density Variations.

Then if

$$D = r_c^4 \left(\frac{\eta \epsilon_o \pi u}{2 I_o}\right)^2 ,$$

where D is a constant for a given beam voltage,

$$R_g^4 = D\left(\frac{B_c}{B}\right)^2 B^4 . \tag{34}$$

Since $R_g \sim B$, the value of r_e was tabulated for several values of B for different ratios B_c/B and the appropriate curves drawn. In the calculation using Equation (17), the ratio r_e/a was obtained. The value of effective beam voltage was used in calculating a in a manner similar to that used in calculating the Brillouin magnetic field.

The beam radius containing 94 per cent of the beam was plotted for several values of magnetic field. Data was taken on the beam using two different cathodes in the same gun. Values of r_e obtained from each cathode over different ranges of magnetic field are shown. The radius including 94 per cent of the current was chosen for this plot to obtain the best fit with the theoretical curves. Several values of radius were tried, all of which produced curves of nearly the same shape but different vertical position on the plot. The value of r_e for the lowest magnetic field was most important, since it should have been just above the curve calculated for $B_c/B \cong 0$.

The variation of the equilibrium radius as the magnetic field was increased indicated that $B_c/B = .004$. The presence of this flux is important in explaining some of the anomalies observed by Gilmour[3] and is discussed more fully in a later section.

D. SCALLOP WAVELENGTH

In Section II it was shown that when the entrance conditions at the anode exit were not those required for Brillouin flow,* the beam edge would oscillate radially, so that the beam took on a scalloped appearance. The scallop wavelength was derived from the linearized trajectory equation. This wavelength is plotted in Figure 5 for low values of B_c/B. The general behavior is seen to agree with the behavior predicted in the discussion of the theory. The value of λ_c used in calculating the scallop wavelength was obtained from the beam velocity and magnetic field: $\lambda_c = 2\pi u/\eta B$. The accuracy of this calculation of λ_c has been experimentally verified by Gilmour,[3] who used the effective beam velocity.

Figure 5 shows values of scallop wavelength obtained from measurements, similar to those of Figure 3, of current density on the axis. These values support the observation that there is a fraction of the focusing field threading the cathode and that $B_c/B \cong .004$.

Some further measurements of the scallop wavelength were made with some of the shielding removed from the cathode. In addition to the ferromagnetic gun shell, an iron cap was usually placed over the gun to provide additional shielding. This cap is shown in Figure 13. By removing this cap the amount of flux threading the cathode was increased slightly. The measurements of scallop wavelength shown in Figure 5 indicate that this increase was $B_c/B \cong .002$.

This change in the scallop wavelength obtained by allowing additional flux to thread the cathode supports the view that the decrease in

*The term Brillouin flow refers to a Brillouin beam focused by the Brillouin field.

scallop wavelength below the theoretical value was indeed due to a small amount of flux threading the cathode. This is important in explaining the anomaly observed by Gilmour.[3] He measured scallop wavelengths 7 per cent shorter than those predicted by theory ($\lambda_s = 1.31\,\lambda_c$ instead of $\lambda_s = \sqrt{2}\,\lambda_c$), but concluded that no flux threaded the cathode because the plot of λ_s versus B had a slope of -1. The basis for this conclusion is shown in Figure 6, where the values of scallop wavelength measured from oscillations of the beam edge are plotted. The points represented by circles are values obtained in this study, and those by squares are values obtained by Gilmour.[3] The agreement between these values is seen to be extremely good, which points to the high accuracy of these measurements.

This high accuracy near the Brillouin value of magnetic field makes significant the marked deviation between values of scallop wavelength measured from the oscillations of the beam edge and those measured from the variation in charge density on the beam axis. This deviation must arise from phenomena not included in the laminar theory. This difference can be explained by considering the motion of a group of translaminar electrons moving in the interior of the beam.

Assume, then, that the theory is valid and that the values of scallop wavelength measured from the current density on the axis are those closest to the correct value, even though near the Brillouin field these values were also lower than predicted by the theory. It should be noted that any phenomenon which alters the scallop wavelength of those electrons near the outer edge of the beam might also affect the wavelength of electrons near the beam axis.

Brewer[6] has shown that for a Brillouin beam that does not scallop, the interior of the beam is a force-free region; that is, an electron moving across the beam in a translaminar manner will not be deflected until it passes outside the beam. For a Brillouin beam with small scallops, the forces on translaminar internal electrons will be small. If there are significant numbers of translaminar electrons, this idealized view would not be valid, but this would be because the laminar electrons had been perturbed from their "perfect" Brillouin trajectories.

Consider the case of a Brillouin beam that is scalloping very slightly, as illustrated in Figure 7. In the interior of this beam is a stream of translaminar electrons comprising only a few per cent of the total beam current. The translaminar stream can be considered to be scalloping with a wavelength shorter than the beam scallop wavelength. Since this translaminar stream is oscillating violently, the forces on electrons in this stream are relatively large, and the wavelength of this stream may be considered to be rather stable. The laminar electrons are oscillating with low amplitudes, where the focusing forces are

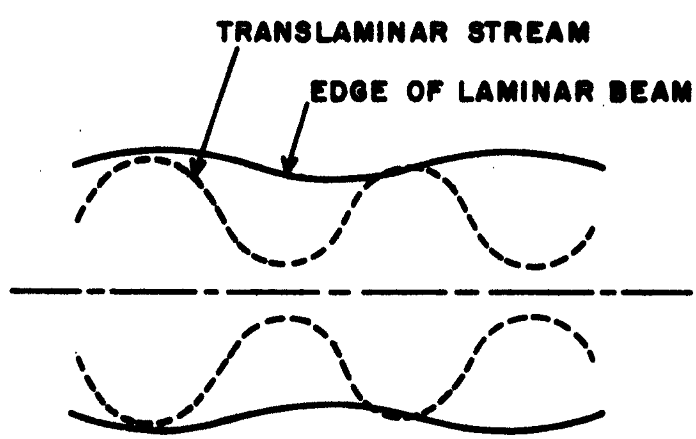

Figure 7. Motion of Translaminar Stream in Brillouin Beam.

delicately balanced, therefore it is quite conceivable that the space-charge forces of the translaminar stream would "pull" the wavelength of the laminar electrons toward the translaminar scallop wavelength. This would appear as a shortening of the beam scallop wavelength. The wavelength of the translaminar stream would also be pulled toward the scallop wavelength of the beam to allow the transverse momentum to be conserved. This pulling effect on the wavelength would be most noticeable near Brillouin flow. Since this translaminar stream is assumed to include only a small per cent of the total beam current, its effect on the wavelength would not be appreciable when the scalloping becomes large.

This hypothesis can now be related to the actual beam studied. At high magnetic fields, a translaminar stream such as the one described was clearly observed in the beam, and cross sections of the beam taken at several axial positions showed that it oscillated violently. The presence of this stream can also be noted in Figure 3a at the points where it passed near the beam axis. At values near Brillouin flow and below, this translaminar stream became too diffused to be identified, but the translaminar electrons should still be present in the beam. The wavelength of the stream was determined at high values of magnetic field and is plotted in Figure 6. A curve drawn through these values would be similar to one plotted from the theory for a rather high value of flux threading the cathode. Near the edge of the cathode the flux threading the cathode would be expected to be higher than the average flux threading the cathode because of the close proximity of the ferromagnetic focusing electrode. Also, Brewer[6] has shown that the electrons near the beam edge are likely to be formed into a translaminar stream by aberrations in the anode aperture.

Thus not only the presence but the origin of this translaminar stream can be identified.

Therefore, near Brillouin flow, translaminar electrons were present in the beam which could disturb the scallop wavelength as hypothesized. For a magnetic field of roughly 200 gauss, i.e., 2/3 the scallop-free Brillouin value, the curve of slope - 1 is seen to turn toward the value predicted by the theory. From the hypothesis this would be expected as the beam scalloping again became large. Because the slight upward trend in the value of scallop wavelength was always observed, it must be considered significant. Furthermore, Gilmour observed this phenomenon occurring consistently at values of beam voltage in the range 3000 v – 6000 v.

The presence of oscillations with two different wavelengths in the beam should result in a beating effect. This was in fact observed; moreover, it was observed only for focusing fields near the Brillouin field. Because of the small amplitude of the beam scallops in this region, it was difficult to observe, but it was observed by measuring current density variation on the axis with high level of gain in the recording circuitry.

It may be safely concluded, therefore, that the translaminar electrons in the beam had caused part of the reduction in scallop wavelength observed by Gilmour. Of the 7 per cent error, about 3 per cent may be attributed to the presence of flux threading the cathode and the remaining 4 per cent to the pulling effect of the translaminar electrons.

It has been shown that when flux threads the cathode, the translaminar stream cannot pass through the beam axis. Since the primary effect of this stream must be on electrons in the region through which it moves, this explains why the scallop wavelength measured from the current

density variation on the beam axis should differ from that measured at the beam edge. The slight decrease in scallop wavelength on the beam axis below the theoretical value may be ascribed to the secondary effect of the wavelength of the outer edge scallop pulling the axial scallop wavelength.

Some other properties of the translaminar stream should be noted:

1. The reason the translaminar stream appears in Figure 3a is that the pin-hole of the scanner was not exactly on the beam axis. This was because the beam axis oscillated about the axis of the drift tube at the cyclotron wavelength. At some axial positions where the stream would have been expected to appear, it was not seen because the pin-hole was on the beam axis.

2. The translaminar stream discussed here was not a part of the tails that have been observed moving transversely in the beam.[3] The scallop wavelength of an electron that makes up part of the tails is nearly that of the beam and therefore would not fit into the explanation of the shortened scallop wavelength.

3. The translaminar stream referred to here is definitely a property of the STL-100 gun and not the result of a cathode imperfection or misalignment of one particular cathode. It was observed on the beams generated from several cathodes.

E. MAGNITUDE OF BEAM SCALLOPS

The magnitude of the beam scallops computed from Equation (30) is plotted in Figure 8. The radius including 95 per cent of the beam and the radius of the outer edge of the beam are shown on the plot. The outer edge of the beam was determined by extrapolating the side of the beam to zero current as shown in Figure 9. Neither of these values of the radius

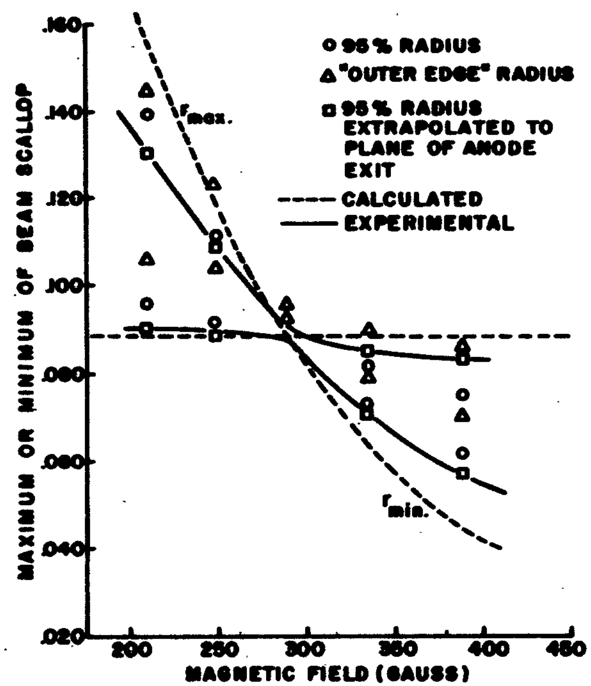

Figure 8. Magnitude of Beam Scallops as Magnetic Field is Varied.

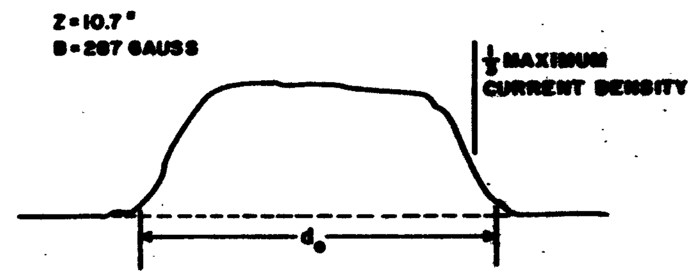

Figure 9. Method of Measuring Radius of "Outer Edge" of Beam. (d_o is "outer edge", diameter obtained by extrapolating sides of beam cross section to zero.)

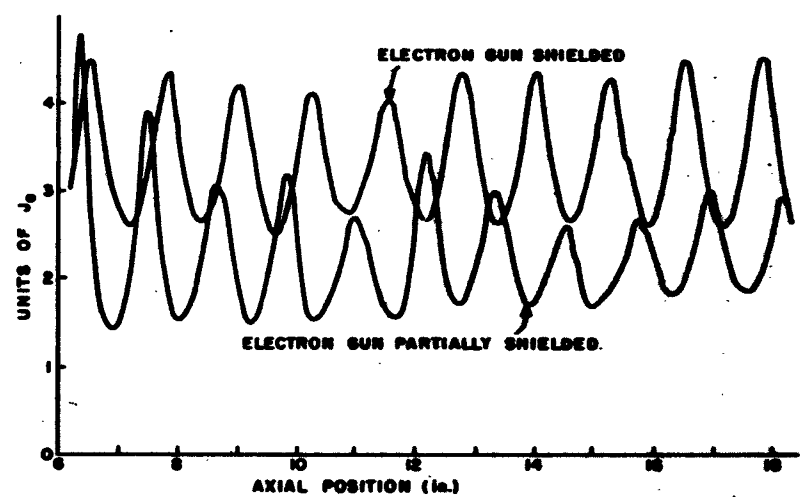

Figure 10. Effect of Flux through the Cathode on Current Density on the Beam Axis.

provides a good fit with the theory for magnetic fields either above or below the Brillouin field of 290 gauss.

This discrepancy can be resolved after careful examination of Figure 2, which shows that the amplitude of the scallops decreased and the equilibrium radius of the beam increased as a function of axial position. Somewhat better correlation between the theory and experiment was obtained by a linear extrapolation of the measured values of the maximum and minimum radii of excursion back to the plane of the anode exit. There is of course no particular justification for using a linear extrapolation or even the same extrapolation for all values of maxima and minima, but this extrapolation points up the problem. A good fit between the maximum and minimum radius of the beam scallop was not obtained, because it was not possible to determine the amplitude of the initial scallop.

This decrease in the magnitude of the scallops and increase of equilibrium radius had been observed by Rigrod[9] and used to explain the growth of noise in the beam. He considered the mechanism for this noise growth to be scalloped beam amplification, in the manner described by Mihran.[10] It is possible that this phenomenon could be used to explain the decrease in magnitude of the beam scallop observed here.

F. ACCURACY OF THE LINEARIZED THEORY

Striking confirmation of the validity of the linearized theory for the region of interest was obtained using the data presented in Figure 10. In this figure data similar to that shown in Figure 3 was obtained with and without the shielding cap over the electron gun. The average axial current

was reduced by approximately 28 per cent when some of the shielding was removed. If the beam shape remains constant (variation of P with radius does not change), then

$$\therefore \frac{\Delta J_o}{J_o} = \frac{(\Delta r_e)^2}{(r_e)^2} \quad , \tag{35}$$

and the decrease in axial density corresponds to an increase in the equilibrium radius of 13 per cent. From Figure 4, this corresponds to an increase in equilibrium radius to 0.61 in. or $B_c/B \cong .006$. This value of flux threading the cathode when the shielding cap was removed is the same as that obtained in direct measurements. This agreement attests to the accuracy of the measurements and the soundness of the theory.

G. THERMAL EFFECTS

It is well recognized that the assumption of a laminar beam is highly idealistic. In a true laminar beam the electrons must have zero velocity at the cathode, whereas, in fact, the electrons are emitted in random directions with a wide range of velocities. Thus despite the excellent agreement noted between the laminar theory and the over-all beam behavior, some differences in the details of electron motion are to be expected.

It is characteristic of electron beams that the beam edge is not sharp, as predicted by the laminar theory. This arises from the transverse velocities of the thermal electrons which cross the nominal beam edge and cause this edge to appear diffuse. Pierce and Walker[11] have derived a theory that incorporates a thermal correction into the laminar theory. They assume that the transverse velocities of the electrons are

in thermal equilibrium with a Maxwellian distribution of charge density within the beam. In their derivation, Pierce and Walker derive a factor, μ, which is proportional to the beam parameters:

$$\mu = 5.56 \frac{I_o}{T_o \sqrt{V_o}} , \tag{36}$$

where

I_o = beam current in milliamperes,

V_o = beam voltage in kilovolts,

T_o = beam temperature in hundreds of degrees Centigrade.

It has been observed both theoretically and experimentally[12] that T_o may be calculated by

$$T_o = M^2 T_c , \tag{37}$$

where M^2 is the area convergence ratio of the gun, and T_c is the cathode temperature.

The fraction of the beam outside a selected radius has been plotted for various values of μ. This plot is reproduced for three values of μ in Figure 11. Using the known beam and gun parameters for a beam voltage of 5000 volts gives

$$\mu = 21.3 .$$

This indicates that the "cold" Brillouin radius (for which $T_o = 0$) would include 90 per cent of the current, but this would require a value of Brillouin field much higher than the experimental value; therefore the 95 per cent radius must be the "cold" radius, and the value of μ must be adjusted to $\mu = 100$.

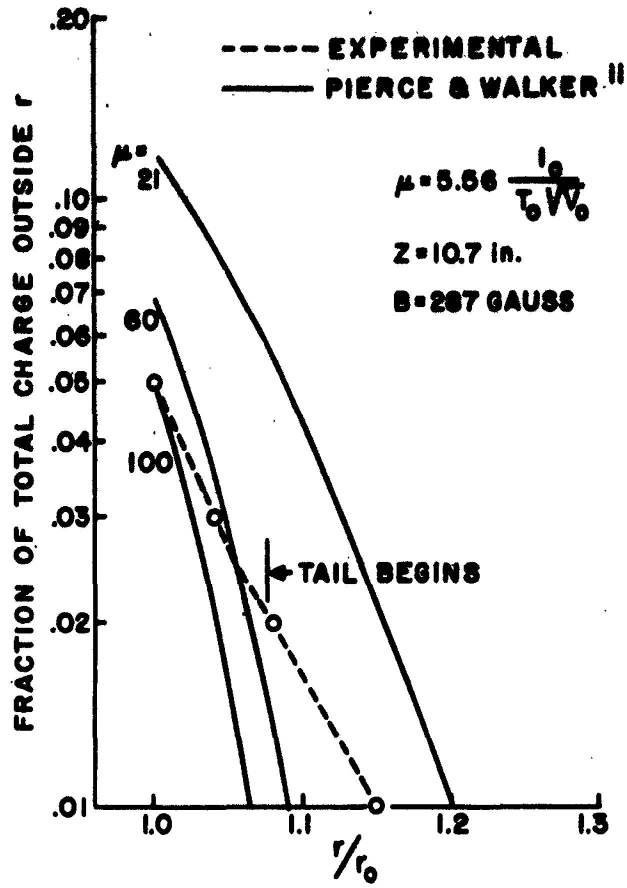

Figure 11. Fraction of Charge Outside of Given Radius, r, Normalized to "Cold" Brillouin Radius, r_o.

The shape of a beam edge obtained from a typical cross section is also shown in Figure 11. In view of the crudeness with which the data points were taken, the correspondence with the Pierce-Walker theory is good. The most significant result is that the observed beam temperature using the "cold" radius was five times lower than that predicted from the Pierce-Walker theory and from Equation (6). The reason for this is not fully understood.

Another theory that has been proposed to describe the thermal velocity effects in the beam is Herrmann's optical theory.[13] The electrons are assumed to move in a perfect optical system under the paraxial-ray assumptions, and the requirement of laminarity is discarded. The beam is shown to form corssovers and images at successive points on the axis. At a crossover the beam cross section is Gaussian in shape, and at an image the beam cross section is rectangular (an image of the cathode). This theory also predicts that the focusing field should be larger than that predicted by the laminar theory as given in Equation (33).

Electron flow like that predicted by the optical theory has been observed experimentally under special conditions;[7] i.e. at low voltage, where thermal effects become very significant. In this study the STL-100 gun was also operated at low voltage – 420 volts – to see if a correlation between the beam behavior and the optical theory could be obtained. This data is shown in Figure 12a and can be compared with the data obtained at 5000 volts as shown in Figure 12b.

The beam edge is much more diffuse in Figure 12a than in Figure 12b. The thermal theory of Pierce and Walker predicts this. From Equation (36) for a beam of constant perveance, K,

$$\mu \sim \frac{I_o}{T_o \, V_o^{1/2}} = \frac{K \, V_o}{T_o} \, , \tag{38}$$

so that μ is directly proportional to the beam voltage. Using the value already obtained of $\mu = 100$ at 5000 volts, we get $\mu = 8.4$ for 420 volts, and from Pierce and Walker's results, the "cold" Brillouin radius is found to include only 80 per cent of the beam current. This accounts for the diffuse beam edge. The optical theory does not provide a means for determining

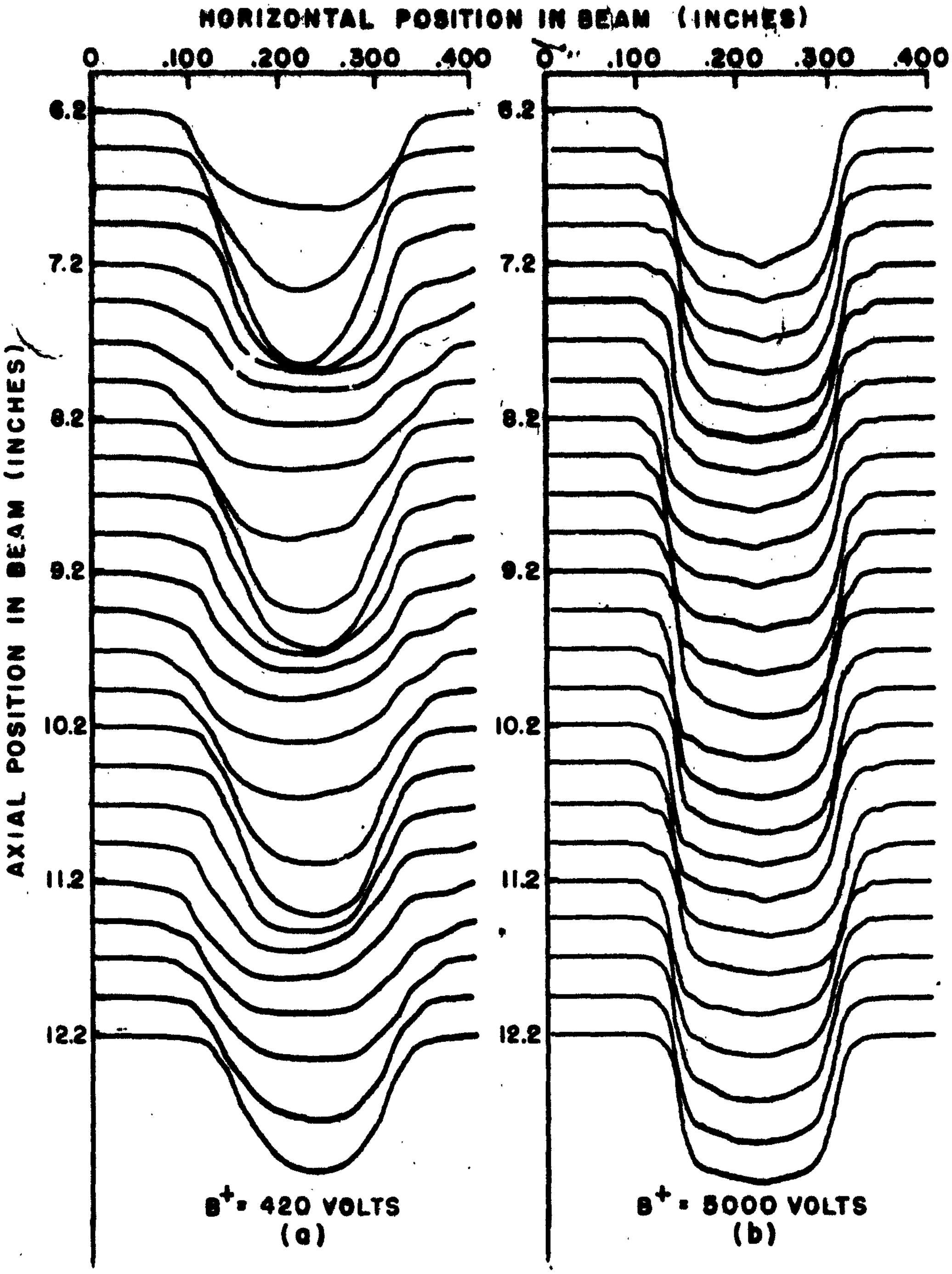

Figure 12. Beam Cross-Sections Showing Applicability of Optical Theory.

the beam edge. Since the beam edge is diffuse, one must be able to determine the nominal beam edge; therefore the 80 per cent radius obtained from Pierce and Walker was used.

When the beam radius that included 80 per cent of the beam was plotted, it was found that this radius scalloped about the value $r_e = .087$ in., which is essentially the same as the "cold" Brillouin radius determined at a beam voltage of 5000 volts. Ideally the beam edge should not scallop at this radius. It was shown in an experiment at 5000 volts, however, that beam scalloping of considerable magnitude could readily be induced by moving the magnetic pole piece axially 1/8 in. This changed the entry conditions at the anode exit so that they deviated from ideal conditions, which would indicate that the scalloping of the beam edge at 420 volts may be attributed to improper entry conditions.

Except for the diffuse beam edge and scalloping, the beam was seen to follow the predictions of the optical theory. The fact that Gaussian crossovers were formed periodically is not entirely evident from the data in Figure 12a because of the distortions arising from the beam scalloping. A scallop wavelength of 1.19 λ_c was measured, which could be compared to the distance between images of 1.6 λ_c. It was not possible to adjust the focusing field so that the current density on the axis did not vary, as would be expected from the model of the optical theory.

The validity of the laminar and optical theories for the low-voltage beam is compared in the following table. The values calculated from the optical theory were obtained using Equation (5) instead of the corrected beam temperature needed for the Pierce and Walker theory, and are shown in Table I.

TABLE I

Comparison of Optical and Laminar Theories with Experimental Measurements

Value	Measured	Laminar Theory	Optical Theory
B (gauss)	107	84	108
λ_s/λ_c	1.19	1.41	1.21

The beam behavior at 5000 volts does not agree with the optical theory model. A calculation using this theory predicts a required focusing field of 306 gauss, which is somewhat high. Much more serious is the difference in the beam cross section and the prediction of periodic crossovers of Gaussian shape. The data in Figure 12b show no such tendency. When similar data were taken over the full range of from 6.2 in. to 20 in. from the anode exit, no change in the beam cross section was noted. This also held true when the beam was scalloping with radial variations of up to 40 per cent. A calculation from the optical theory predicts that crossovers should occur every 10.2 in., so that at least one cross over should have occurred within the space in which data was taken. The assumptions under which the optical theory was derived do not seem to have been violated, so it would seem that the model is not valid at high voltages.

IV. DISCUSSION AND CONCLUSION

A. SUMMARY OF RESULTS

The linearized theory of the laminar beam presented has been shown to predict the beam behavior near Brillouin flow accurately even when a small amount of flux threads the cathode, which indicates that the laminar model gives a close representation of the behavior of the medium-power beam. The observed correlation between separate measurements on the beam, which was predicted by the theory, indicates that the data taken in this experiment are of high accuracy.

The optical model of the beam, which has been proposed to allow for the thermal velocities of the electrons, was shown to be very accurate at low beam voltage (420 volts), but not valid at the higher voltages usually used with this beam. At higher voltages the beam was focused at the calculated Brillouin field and the periodic appearance of Gaussian cross sections in the beam was not observed, as would be expected from the laminar model. Therefore, the laminar model is a closer representation of the actual beam behavior at higher voltages. This is not very surprising, since at higher beam voltages the thermal effects become relatively smaller. It has not been previously reported that the optical theory is not applicable at higher voltages. It should, therefore, be restricted in its application to devices operating at low beam voltages.

The linearized theory developed in this report has wider application than the theory used by Gilmour[3] in that the restriction $R_g \ll 1$ has been removed. For a gun of high area convergence, such as the one used in the

STL-100, this restriction can be shown to make Gilmour's theory invalid even when B_c/B is only a small fraction of one per cent.

The anomaly in the scallop wavelength observed by Gilmour was also observed in this experiment. In addition it was observed that the scallop wavelengths measured on the beam axis near Brillouin flow differed from those measured on the beam axis. This behavior has been attributed to a translaminar stream moving near the outer edge of the laminar beam that "pulled" the scallop wavelength of the outer edge electrons when the focusing field was near the Brillouin field. Gilmour's finding that a straight line of slope -1 best fit his data points, indicating an observed scallop wavelength less than the calculated value, must be attributed to his data being taken over a narrower range than reported here.

The anomalous magnitude of the beam scallop has been shown to be due at least in part to the data not being taken in the region where the beam entered the magnetic field and to the scallop decreasing with axial position from the anode exit to the region where data were taken. This decrease in the magnitude of the scallop cannot be explained using the laminar theory but may be due to noise amplification in the beam as described by Rigrod.[9]

The diffuse appearance of the beam edge was shown to result from thermal spreading of the electrons across the nominal beam edge as predicted by Pierce and Walker.[11] This agrees with the results of a much more thorough investigation by Brewer,[6] except that an equivalent beam temperature of only one-fifth of the value usually taken[12] was required to obtain this agreement. The reason for this discrepancy is not known at this time.

B. PROPOSALS FOR FUTURE INVESTIGATION

An investigation of the beam flow in the first six inches after leaving the anode exit should be made. This should make it possible to determine the magnitude of the beam scallops at the arode exit, and the experimental results could then be compared with the maximum and minimum of the scallops predicted by the laminar theory. The shape of the beam edge at several axial positions starting with the anode exit should be compared to the shape predicted by the Pierce and Walker theory. It may be that this theory accurately predicts the beam shape at the anode exit when the calculated value[12] of the beam temperature is used. It does not predict the beam shape in the drift region, where one-fifth of the calculated beam temperature was used. A possible change in beam temperature between the two regions may be related to the decrease in the magnitude of the scallops. Such a change in temperature with distance is not predicted by the Pierce and Walker theory, it would probably be necessary to study the axial variation in transverse noise velocities in the beam to explain it.

A bucking coil should be used with the STL-100 gun to investigate the validity of the linearized laminar theory when appreciable amounts of flux thread the cathode. It would also be of great interest to see if the beam used in these studies can be made to behave as an immersed beam, as this would greatly extend the usefulness of this gun for r-f studies on the Cornell beam analyzer.

APPENDIX A. BEAM ANALYZER

The beam analyzer used in obtaining the data in this experiment was first described by A. S. Gilmour[3] and is shown in Figure 13. This appendix reviews the important features of this analyzer and describes the improvements that have been made since Gilmour's report was published.

A. VACUUM SYSTEM

A schematic diagram of the vacuum system of the analyzer is shown in Figure 14. This vacuum system was designed to meet two criteria: (1) that high ultimate vacuum approaching that found in high-power microwave tubes be attainable, and (2) that it be possible to open, close, and evacuate the system easily and quickly.

The most important improvement made in the primary vacuum system in the course of the experiment was the replacement of the oil diffusion pump system with a 75 l/sec VacIon pump. This ion-getter pump provided several advantages over the old system: faster pumpdown, lower ultimate pressure, reliability, and no oil contamination.

1. <u>Faster pumpdown.</u> Because of the size of the beam analyzer, it was not feasible to bake it while it was being pumped, so that in order to obtain a high vacuum, it was necessary to pump the gas that was slowly evolved from the analyzer parts. The speed of the new pump was estimated to be four to five times that of the oil diffusion pump previously used. Furthermore, the necessity of baking the zeolyte trap before turning on the oil-diffusion pump has added a few hours to the pumpdown process. The result was that with the new pump, pressures in the low 10^{-7}mm Hg range were achieved in a few hours, where 3 - 5 days had been required with the oil-

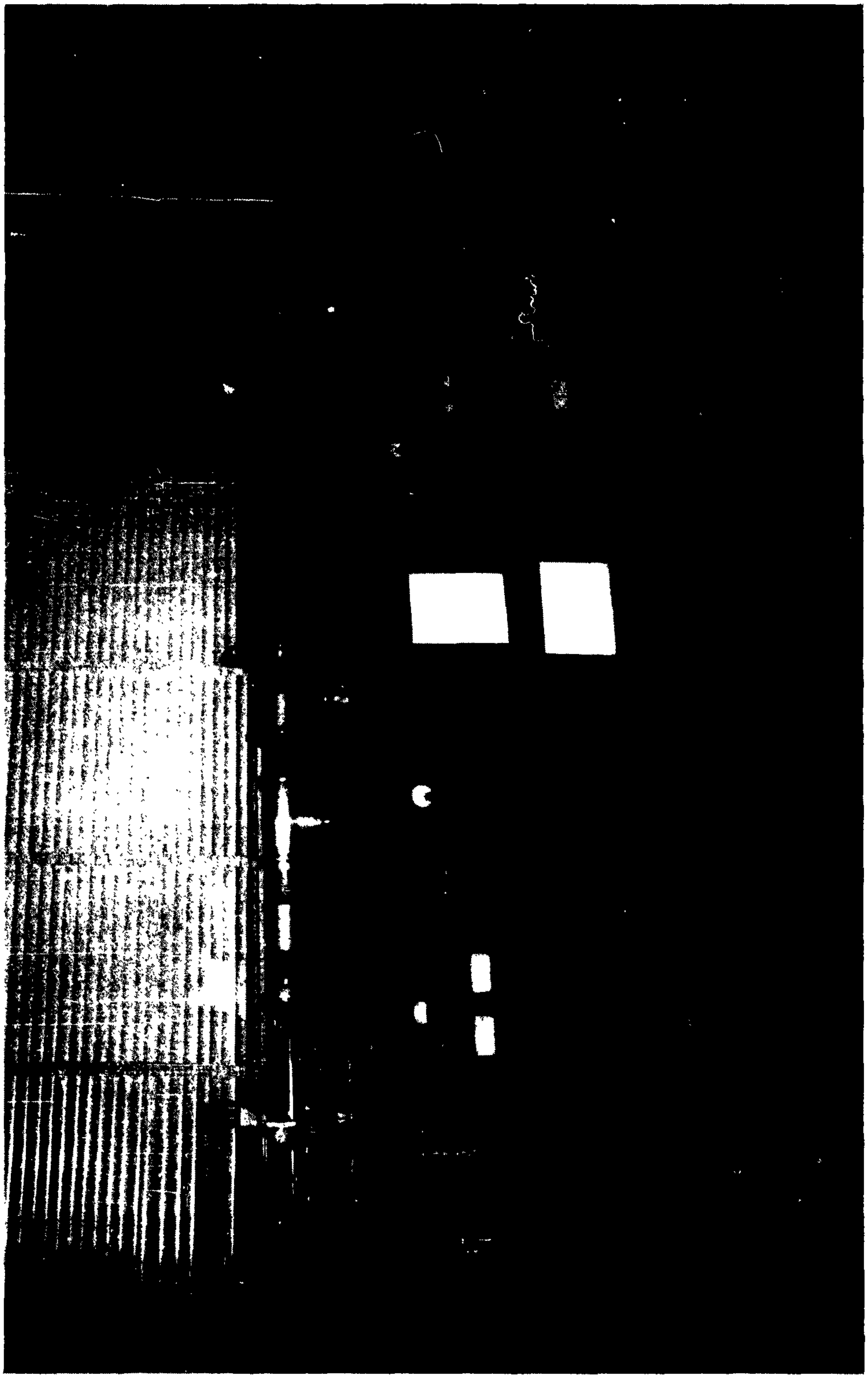

Figure 13. Beam Analyzer.

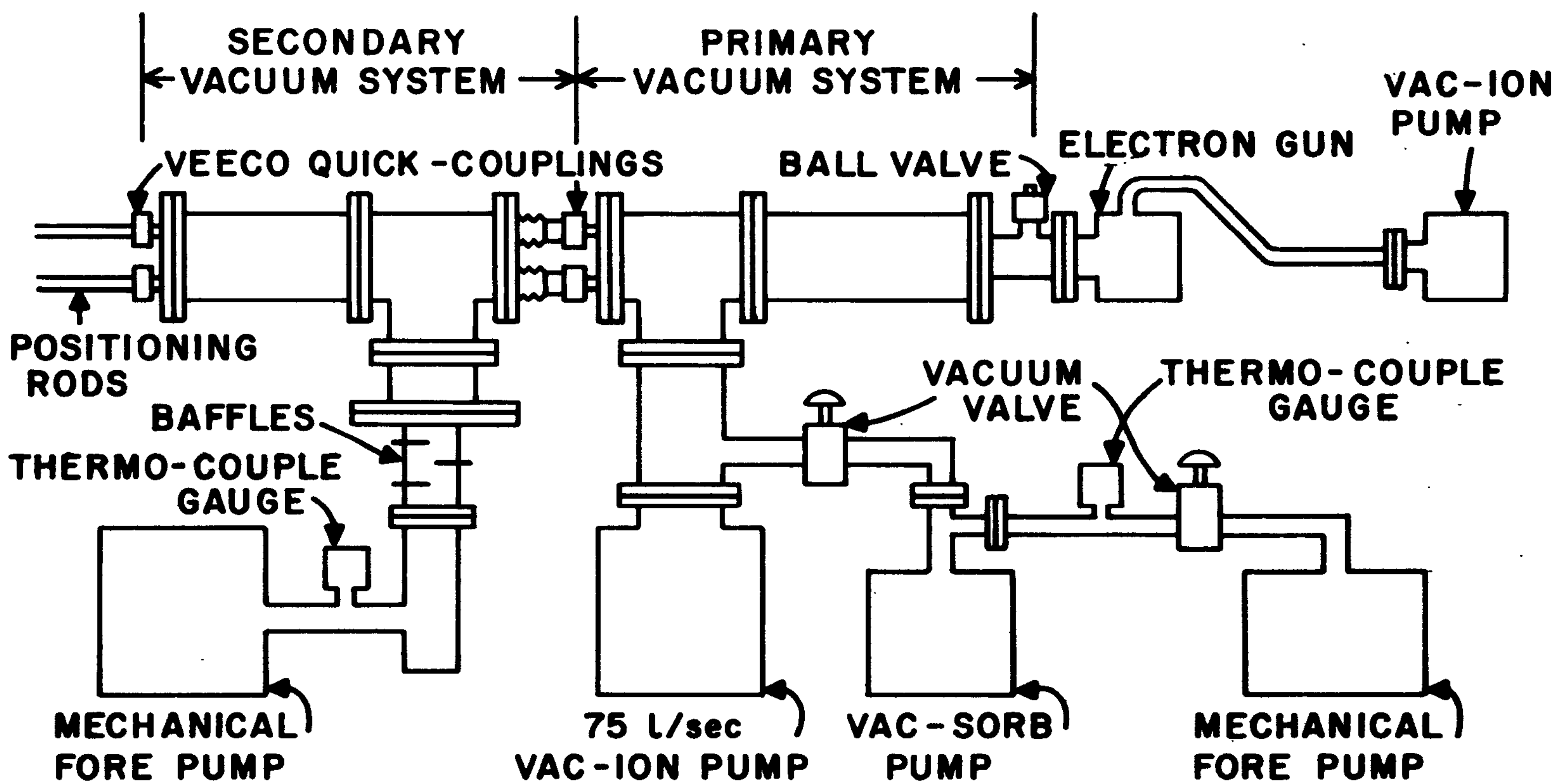

Figure 14. Vacuum System of Beam Analyzer.

diffusion pump, the length of time depending on the cleanliness of the vacuum system when pumpdown began.

2. Lower ultimate pressure. With the oil-diffusion pump, the best vacuum obtained was a little better than 1×10^{-7} mm Hg; whereas with the new pump, a pressure of 2×10^{-8} mm Hg was achieved in the analyzer, an improvement of nearly an order of magnitude in ultimate pressure. This proved to be significant, since it was found that ions affected the focus of the electron beam.*

3. Reliability. When the oil pump was used, electrical and mechanical failures resulted in a loss of vacuum and the spraying of oil from the diffusion pump into the analyzer. This made it necessary to dismantle and clean the analyzer with a consequent loss of several days before the system was pumped down again . While an electric power failure would cause the VacIon pump to stop, it could be restarted, and within a few hours the analyzer would be in operation, since no cleaning would be required.

4. No oil contamination. Even without a power failure, there was a slow but steady backstreaming of oil into the drift tube of the analyzer, which condensed on the scanning mechanism, r-f structure, and walls of the drift tube. With the ball valve open, this oil drifted into the gun region, contaminating the cathode, and thus significantly reducing cathode emission.[1]

The moving parts inside the vacuum system were controlled by polished stainless steel rods sliding through Veeco quick-couplings. These rods were coated with a film of Dow-Corning high-vacuum grease as a lubricant. When the beam was on and data was being taken, it was necessary to move these rods in and out of the primary vacuum system. When the

---

*A report on this study has been issued since this report was written: A. S. Gilmour and D. D. Hallock, "Ion Effects in a Brillouin Beam," Research Report EE 545, Cornell University, 20 October, 1962.

rods were pulled out into the atmosphere, gas was absorbed on their surface. This gas was released when the rods were pushed into the system. In order to keep this effect to a minimum, a secondary vacuum system was used to keep those parts of the rods that were to be moved into the primary vacuum system at a pressure of less than 10 microns when they were pulled out of the drift tube. Under these conditions, when the rods were pushed slowly into the vacuum system, only a small change in pressure was observed with the drift tube in the 10^{-8} mm Hg range.

The flanges used in the beam analyzer were designed for simplicity. They were made from No. 304 stainless steel and polished on the mating sides. Two kinds of gaskets were used. Lead O-rings were used for those seals where no insulation was required between mating sections, and when properly installed these gaskets did not leak. It was necessary to tighten these gaskets periodically after they were first installed, because they tended to creep. Their melting temperature of 180 degrees Centigrade prevented high-temperature bakeout, but this was no problem, since good pressures were obtained without bakeout.

When insulation was required between flanges, teflon gaskets were used. In addition insulating sleeves were placed around the bolts and insulating washers were placed under the bolt heads. These teflon gaskets were reusable for an indefinite period of time.

One of the most important features of the beam analyzer was the high-vacuum ball valve used to isolate the electron gun from the primary vacuum system. A sketch of the ball valve is shown in Figure 15. When the valve was open, the beam passed through the aperture in the ball. When the valve was closed, the drift tube could be opened to atmospheric pressure

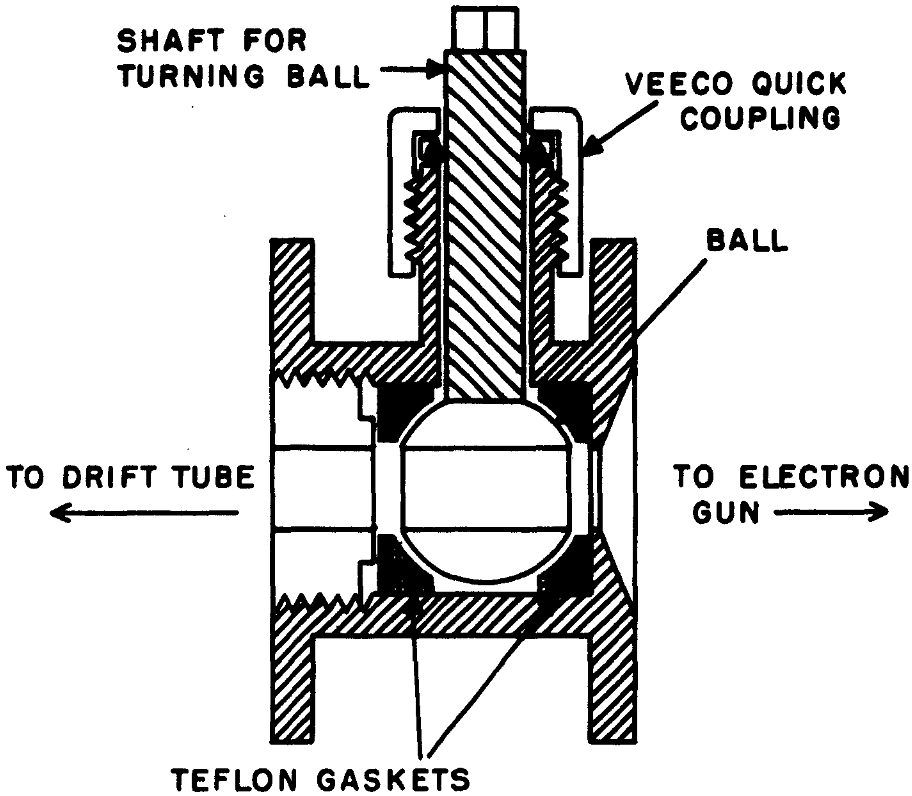

Figure 15. Simplified Sketch of Ball Valve with Ball in Open Position.

while the cathode was kept in a high vacuum. The ball, teflon gaskets, and body shell were obtained from a Jamesbury ball valve. The valve, as modified at Cornell University, was capable of holding the gun at pressures about 5×10^{-9} mm Hg. To obtain this performance, however, it was necessary to lubricate the teflon gaskets. Dow-Corning high-vacuum grease was used for this lubrication.

B. ELECTRON GUN

The electron gun used for this experiment was taken from an STL-100 traveling-wave tube.* This is a Pierce gun with a perveance of 1.15×10^{-6}, and area convergence of 52.7, at Brillouin flow. It was designed to operate at 5400 volts, but tests were made with this gun at beam voltages of 1000 to 10,000 volts with satisfactory results. A photograph of the gun mounted on the beam analyzer is shown in Figure 16.

Mating flanges, similar in design to those used on Varian VacIon pumps were brazed to the gun body and back plate, so that the gun could be readily opened if necessary. A flange that mated with the ball-valve flange was brazed to the gun where it had been cut away from the interaction region of the traveling-wave tube. Provision for pumping the gun when the ball valve was closed was made by attaching an 8 l/sec VacIon pump to the fitting that had served as the exhaust port on the original tube.

Although the electron gun from the STL-100 was capable of d-c operation at 5400 volts, it was necessary to pulse this gun on the beam tester to reduce the power dissipated by the scanning mechanism. The duty cycle was usually .001. A Manson Laboratories modulator capable of supplying up to 20 kv and 20 amperes at a duty cycle of .001 was used to supply the beam voltage.

The heater of the STL-100 gun was operated from a 60-cps sinusoidal supply. When the beam was pulsed at an arbitrary repetition rate, the cathode therefore being pulsed at various values of heater current, Gilmour[3] observed a great deal of modulation on the beam. He attributed

*This was one of five donated to the School of Electrical Engineering by the Sperry Gyroscope Company.

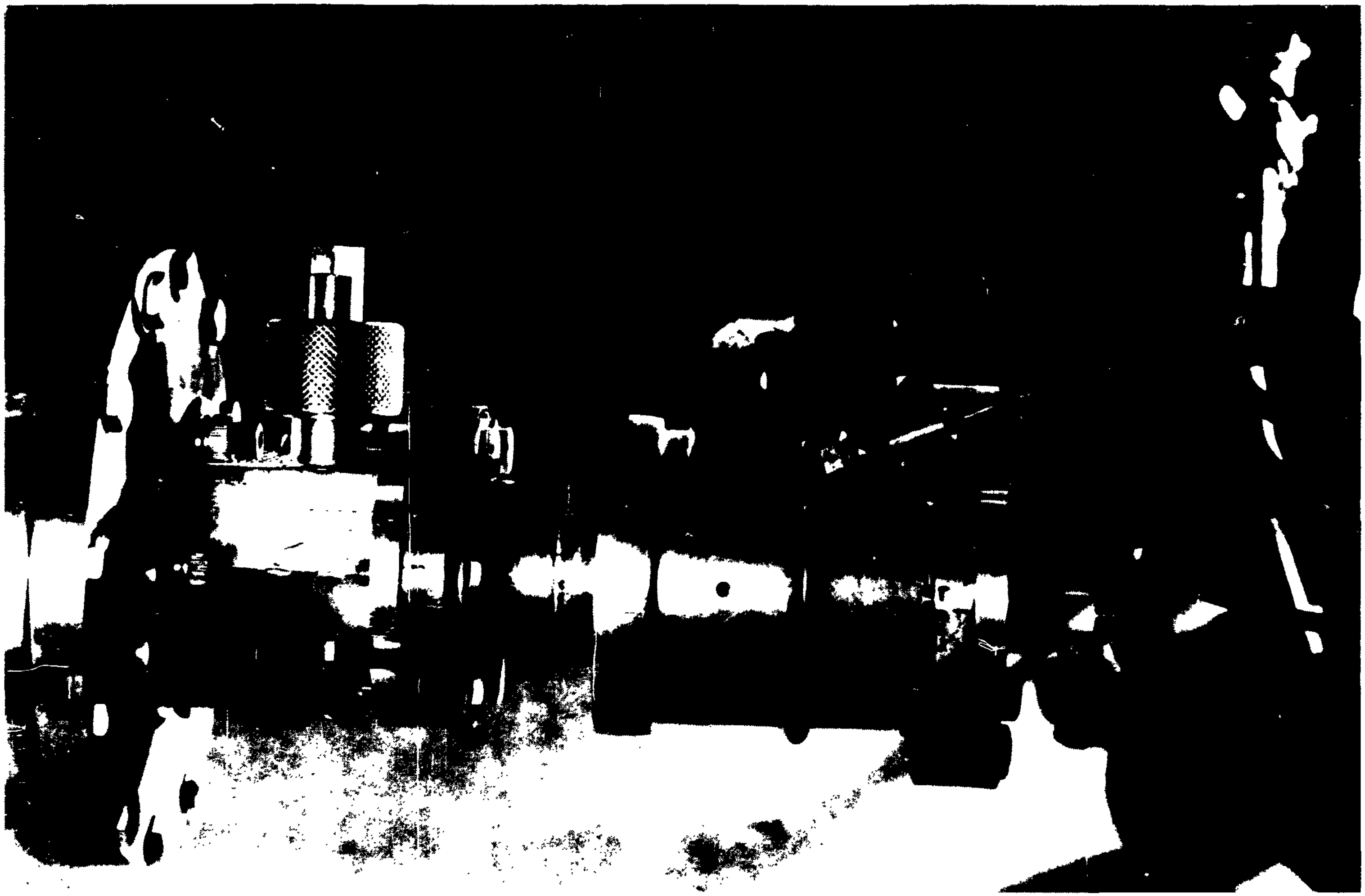

Figure 16. Electron Gun and Ball Valve Mounted on Beam Analyzer.

this modulation to the magnetic field produced by the noninductive heater used in the gun. When the cathode was pulsed at a repetition rate of 60 cps and the pulses synchronized with zeros of the heater current, thus modulation was eliminated, and the laminarity of the electron flow in the beam was greatly improved.

C. BEAM SCANNER

The electron beam was collected on a pin-hole scanner, which was positioned in the x, y, and z directions in the drift tube. A simplified sketch of the scanner is shown in Figure 17. The beam-collecting area on the scanner was a molybdenum plate that was carbonized to reduce the emission of secondary electrons. A .005-inch hole in the center of this plate allowed a small fraction of the beam to pass through the collecting

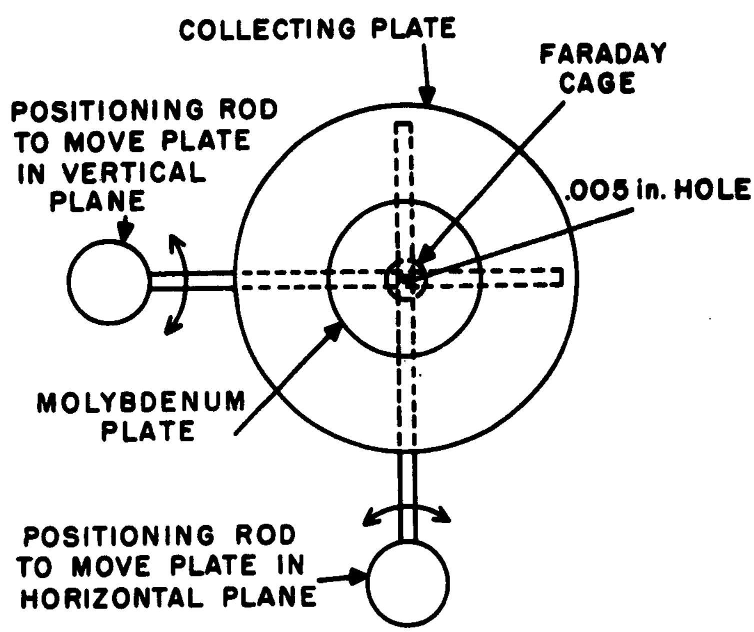

Figure 17. Simplified Sketch of Beam-scanning Mechanism inside Drift Tube.

plate to a Faraday cage. A photograph of the complete scanner is shown in Figure 18. In the beam scanner used for this experiment, the Faraday cage was part of the center conductor of a co-axial line so that injected r-f currents could be measured for other experiments. This, of course, had no effect on its use for d-c measurements.

The scanner was moved by two positioning rods that were controlled from outside the vacuum system. A plate to center the scanner inside the drift tube was attached to these rods behind the collecting plate. The centering plate moved along a guide rail inside the drift tube and was held in position by spring-loaded teflon blocks.

The control mechanism for the positioning rods in shown in Figure 19. The scanning mechanism was moved axially by using the gear and rack arrangement shown in the figure. The angular position of the rods was adjusted by means of the micrometers. The micrometer that set the horizontal position of the scanner was equipped with a motor drive, and reversing switches caused the motor to sweep the scanner back and forth across the beam automatically. A ten-turn helipot was geared to the motor to provide a voltage proportional to the horizontal position of the scanner; this voltage could be applied to the x input of an x-y recorder. The current from the Faraday cage produced a voltage drop across the input resistor of the General Radio electrometer and provided a y input to the recorder proportional to the current to the Faraday cage. Beam cross sections obtained in this manner are shown in Figure 20. From this data the beam diameter could be determined as a function of axial position.

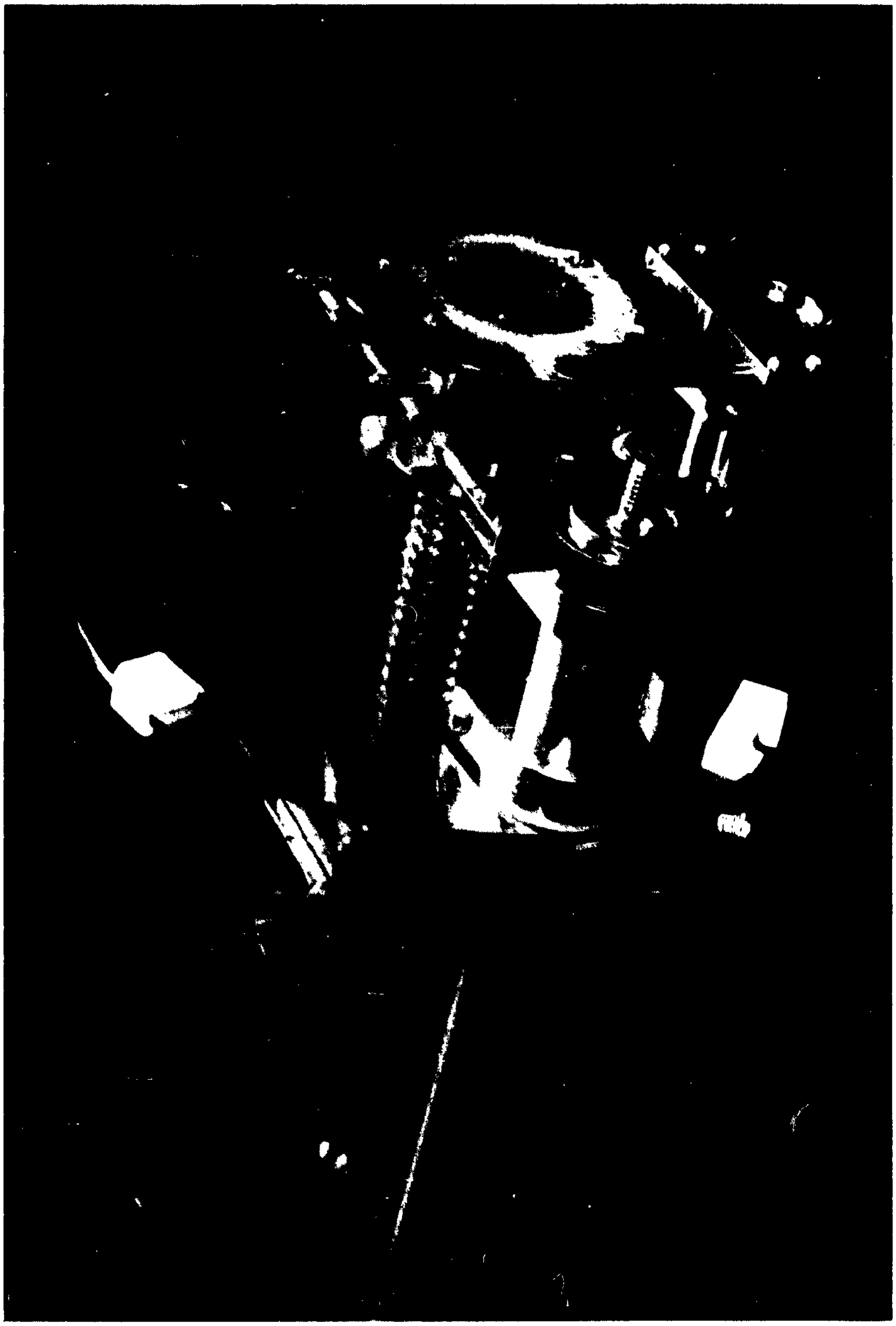

Figure 18. Beam Scanner Assembly.

Figure 19. Control Mechanism for Beam Scanner and Data-Recording System.

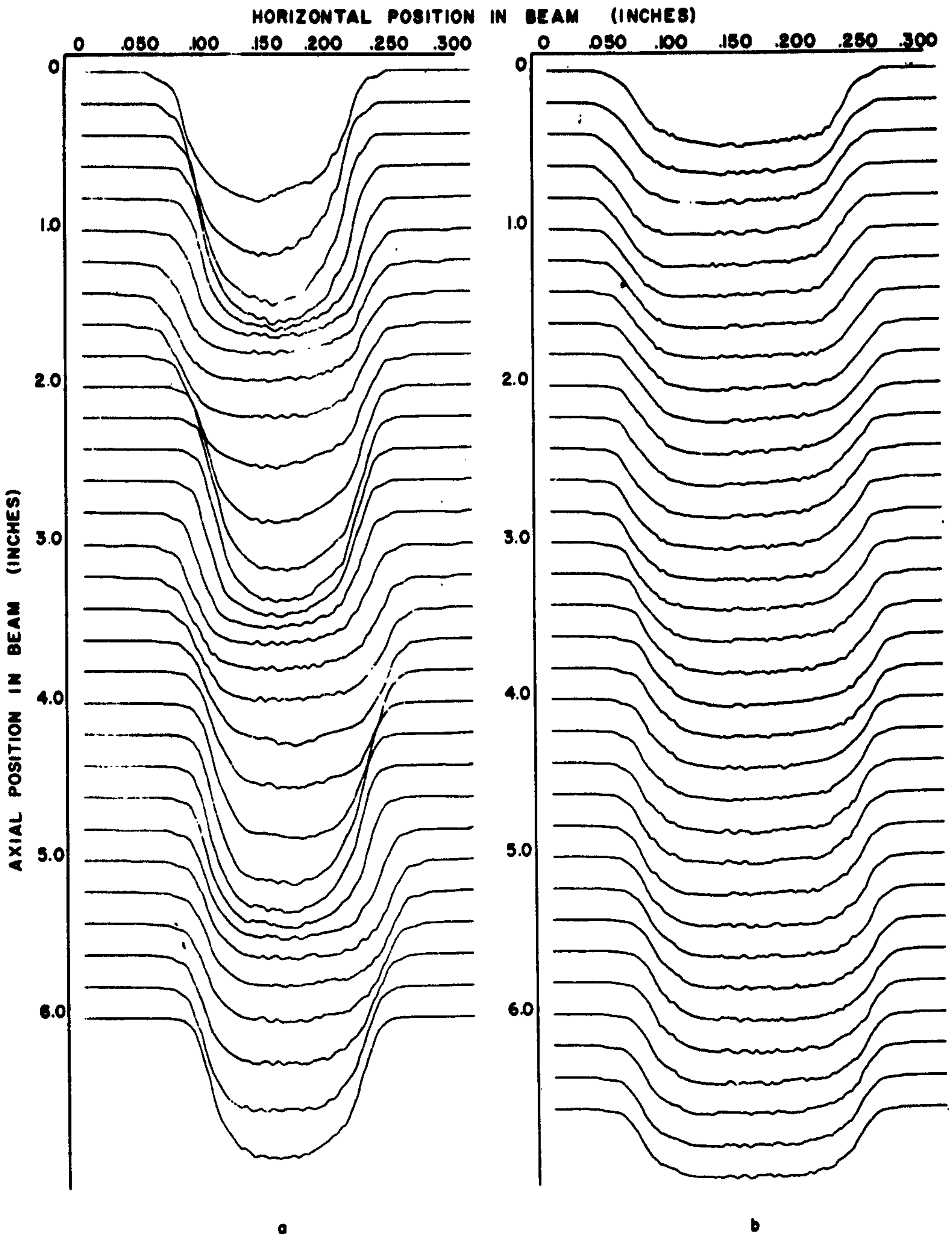

Figure 20. Typical Data from which Beam Diameter Was Obtained.

It was also possible to arrange helipots to provide a voltage proportional to either the x or z position of the scanner. This made it possible to measure the beam current as a function of any one of the three positional parameters in a single scan.

APPENDIX B. BEAM-PERTURBATION EXPERIMENT

The object of this experiment was to measure the degree of laminarity of the electron beam directly. It was planned to identify certain electrons by placing a local perturbation on the beam, which could be tracked in the axial direction. Because of a lack of sensitivity in the detection mechanism, it was necessary to perturb the beam so strongly to detect a change in the beam cross section that the laminar equations of motion were no longer valid. The objectives of the experiment, therefore, were not met. The results of the investigation are summarized here to point up the problems encountered as well as to serve as a basis for future investigations.

A. METHODS OF PERTURBING THE BEAM

The two methods used by previous experimenters for applying a local perturbation on the beam were (1) placing an obstruction in the beam path[14, 15] and (2) removing the oxide coating from a portion of the cathode surface.[15] These techniques were not suitable for this experiment for the following reasons:

1. The perturbation introduced by these methods was more severe than was necessary for detection with the beam analyzer, and it was felt that a better understanding of the behavior of the unperturbed beam would be obtained if the smallest detectable perturbation were used. Since the beam-scanning sensitivity of this analyzer was greater than that available to previous experimenters, a more refined technique was possible.

2. The d-c characteristics of the beam could not be checked. Since a rather small perturbation was anticipated, it was necessary to determine the behavior of the beam under d-c operation precisely for comparison with the perturbed behavior before the perturbation was applied. It was also important to compare the d-c behavior of the beam with the theoretical predictions before perturbing it.

Some method of perturbing the beam by an electric or magnetic field was indicated by the preceding requirements. The idea of using an electric probe was rejected. If the cathode surface is not to be disturbed, such a probe can be used only to perturb the outer edge electrons of the beam. Moreover, the addition of a mechanical structure near the beam edge in the cathode-anode region of the electron gun might disturb the focusing of the beam.

This left the magnetic field as the most promising means of perturbing the beam. Previous electron-beam studies at Cornell University had shown the possibility of using a small transverse magnetic field near the cathode to perturb the beam.[16] The field from a small perturbing coil placed just behind the cathode generated a perturbation in the beam emitted from the portion of the cathode in front of the coil. The degree of perturbation was varied by varying the current flowing through the coil. In addition, the d-c characteristics of the beam were checked simply by not passing any current through the coil. This allowed other experiments with this cathode to be made on the analyzer when data for the laminar flow study were not being taken.

B. DESIGN OF PERTURBING COIL

It was estimated that a transverse magnetic flux density of 5 gauss would be required just in front of the cathode to produce an easily detectable perturbation. This estimate was based on a knowledge of the transverse field developed at peak heater current by the noninductive heater used in the STL-100 cathode and the resulting perturbation of the electron beam. As mentioned in Appendix A, this effect was not present in the d-c beam under test conditions because the cathode was pulsed at a zero of the heater current.

A plot of gauss per ampere-turn was obtained in designing the coil by assuming a single turn at the location of the perturbing coil. This plot showed that approximately 100 ampere-turns were required in the perturbing coil. The choice of seven turns and 15 amperes was made as the best compromise for the design criteria of size, power, and perturbing effect. Because only fringing fields of the coil were used to perturb the beam, only turns close to the cathode were effective. The use of concentric turns was ruled out because of the mechanical problems involved in fabricating such a coil and because this would have made the diameter of the perturbing coil too large to provide only a local perturbation. It was necessary, however, to use as many turns as possible to keep the current from being high.

The estimate of flux density per ampere developed in front of the cathode by the seven-turn coil was calculated by considering the perturbing coil to be equivalent to seven circular turns. The model used is shown in Figure 21(a) and the resulting fields in Figure 21(b). The points at which these

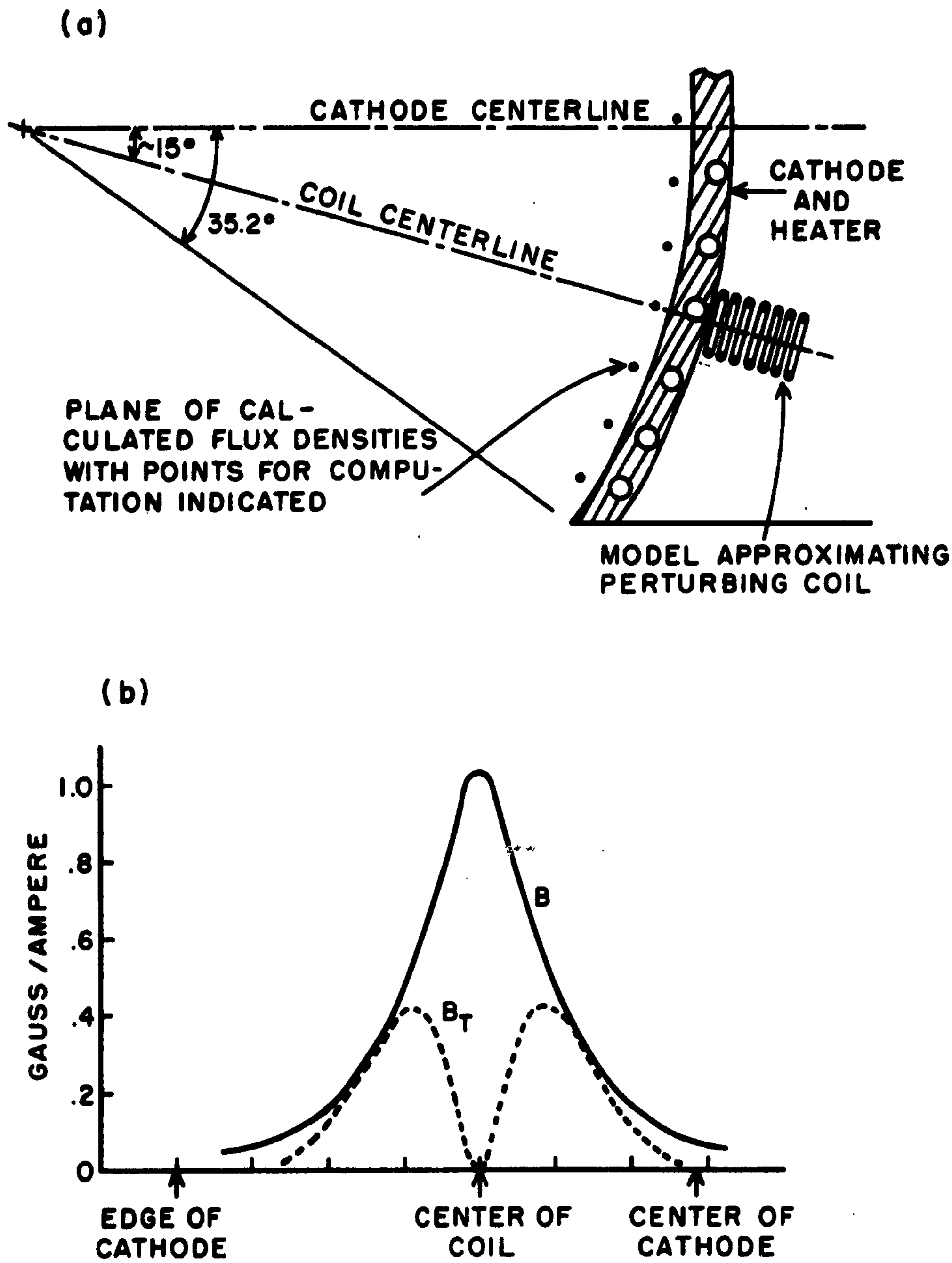

Figure 21. Calculated Flux Density Per Ampere Developed by Perturbing Coil: (a) Schematic Showing Coil Position, (b) Field Distribution.

values were obtained were one millimeter in front of the cathode to obtain flux densities beyond the space-charge depression. This plot, using the more accurate model, shows that only 12 amperes were required in the perturbing coil to provide a sufficient transverse magnetic field, B_T.

A photograph of the coil parts and an assembled perturbing coil are shown in Figure 22. A seven-turn coil of .013-inch tungsten wire (B) was wound on the mandrel (A). The coil was then unscrewed from the mandrel, chemically cleaned, and placed on the ceramic cylinder (C), with one lead going through the center of the cylinder. Nickel straps were spot welded to the coil to hold it in place. Figure 23 is a schematic diagram showing the perturbing coil mounted behind the cathode. The heater lead support structure is omitted for simplicity. The coil was held in place by a molybdenum spring. This permitted some freedom of movement that allowed for thermal expansions. The coil lead from the center of the ceramic cylinder was connected to the cathode, while the other lead was clamped in a block that was fastened to the focusing electrode with a ceramic insulator. The perturbing coil pulse was applied between the perturbing coil lead and the heater-cathode lead. With this arrangement the perturbing coil was always maintained at the cathode potential.

C. MOTION OF THE PERTURBED ELECTRONS

The computation of the exact trajectory of an electron moving through the magnetic field of the small coil mounted behind the cathode is a problem for a computer. In this treatment the motion will be described qualitatively.

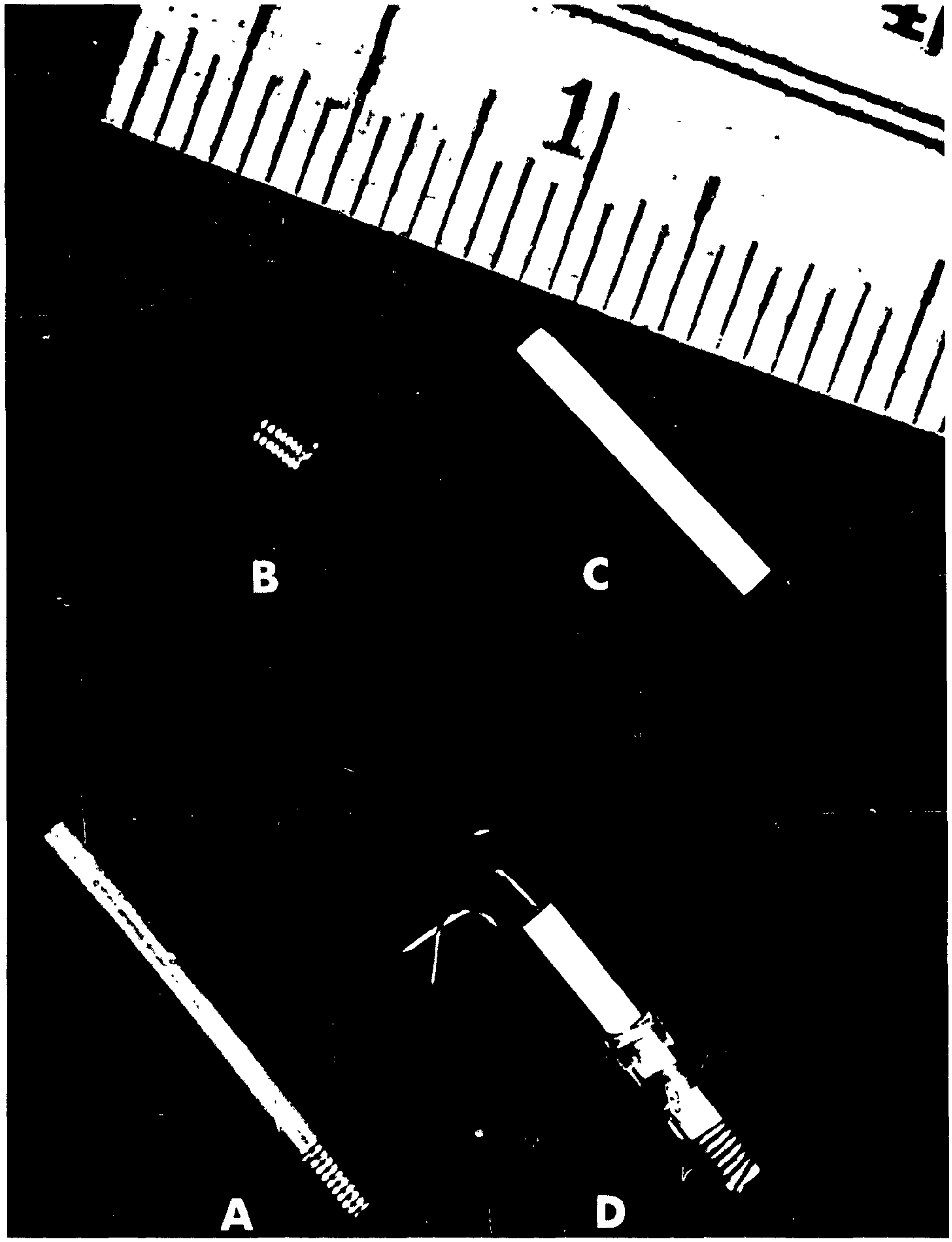

Figure 22. Perturbing Coil and Parts: (a) Mandrel for winding coil, (b) perturbing coil, (c) ceramic tubing, (d) assembled perturbing coil.

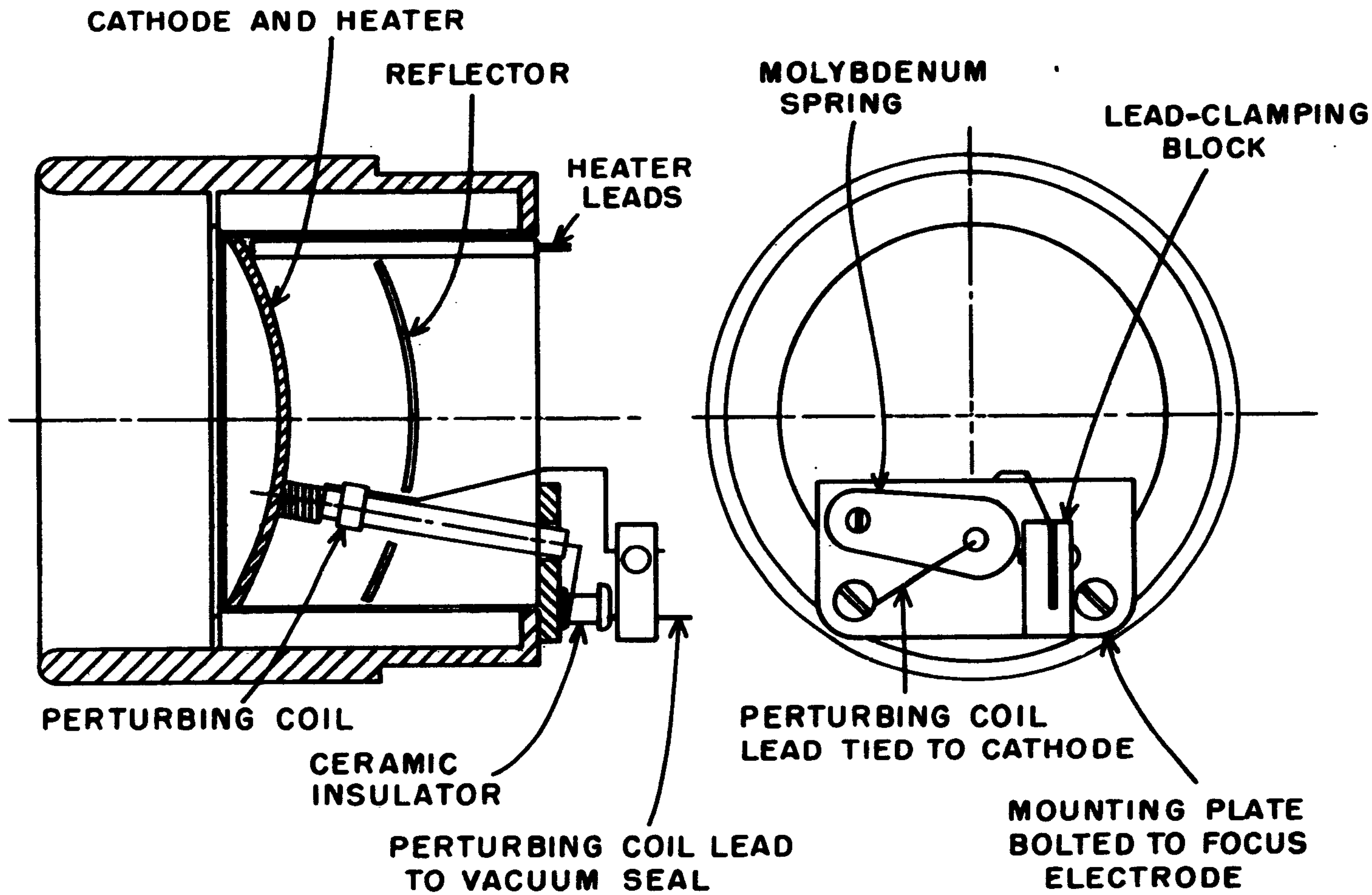

Figure 23. Sketch of Perturbing Coil Mounted behind Cathode.

In the model used to describe the perturbation, the magnetic field that perturbed the electron trajectories was independent of the focusing field. Since the perturbing field strength dropped off as the inverse cube of the distance from the coil, it was assumed that this field gave certain electrons an initial translaminar velocity at the cathode and that it did not extend appreciably into the acceleration region of the gun. This assumption was supported by Figure 24, which shows the maximum value of perturbing field that occurred on the axis of the coil for a current of 15 amperes in the coil. The field strength is seen to drop off to levels which do not seriously perturb the beam beyond about .15 in. in front of the cathode. The field strength that was chosen for this level was roughly that produced by the heater at peak heater current. The countering effect of increasing

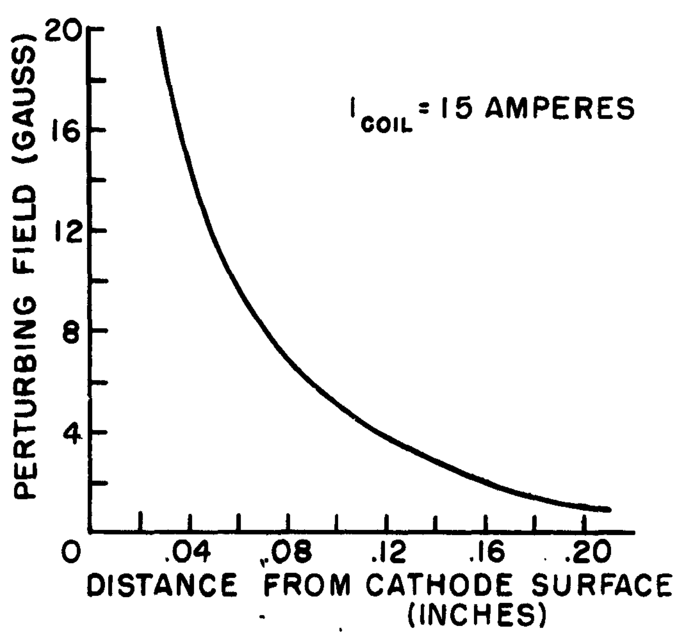

Figure 24. Maximum of Perturbing Field as Function of Distance from Cathode.

electron velocities was not included. This led to an underestimate of the actual perturbation. The extent of the effective perturbing field in front of the cathode is shown in Figure 25.

1. With No Focusing Field Threading the Cathode

Cutler and Hines[17] have developed a method for analyzing the effect of perturbations in Pierce-type electron guns and have applied it to determine the effects of thermal velocity in electron beams. The method assumes an ideal laminar beam, which is treated under paraxial-ray assumptions: (1) All angles of convergence and divergence of laminar flow lines are small; (2) longitudinal electric fields are uniform over a given cross section of the beam; and (3) all radial fields are proportional to the distance from the axis. One electron is perturbed at the cathode and its trajectory is traced as it moves in the laminar beam. Expressions are obtained which give, through the use of graphs, the displacement of the trajectory of this perturbed electron from the trajectory of the laminar electron that originated at the same place on the cathode. This method is readily adapted to determine the displacement of a perturbed electron from that of a laminar electron at the anode exit of the STL-100 gun where the beam is injected into the magnetic field. Figure 26 shows the geometry of the gun and some of the nomenclature required for this derivation.

The radial position of the perturbed electron is given as

$$r(z) = \mu(z)\, r_e(z) \quad , \tag{33}$$

where r_e is the radius of the edge of the beam and μ is a radial co-ordinate, which varies from zero at the beam center to unity at the beam edge. Laminar electrons follow paths of constant u.

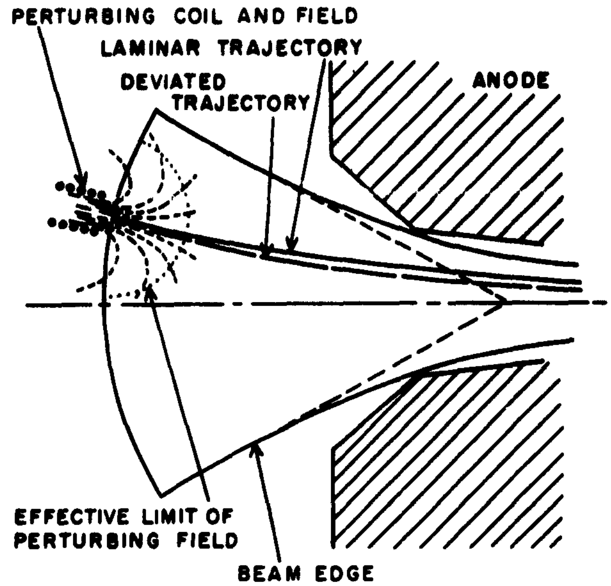

Figure 25. Extent of Effective Perturbing Field into Acceleration Region of Electron Gun.

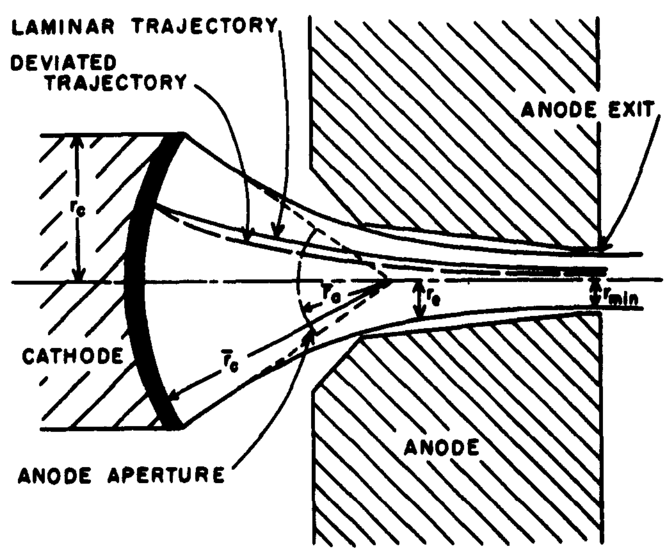

Figure 26. Diagram Showing Electron Gun Parameters Used in Tracing Perturbed Electrons.

From this Cutler and Hines[17] readily obtain

$$\mu - \mu_1 = \left(\frac{d\mu}{dt}\right)_1 \int_{t_1}^{t} \frac{dt}{\left(\frac{r_e}{r_{e_1}}\right)^2} \quad , \tag{34}$$

where the subscript 1 refers to the value at any given reference plane. This gives the trajectory deviation Δr at any place along the axis in terms of the perturbation velocity and position at the reference plane. From Equation (33), this may be written as

$$\Delta r = \mu\, r_e - \mu_1\, r_e = \left(\frac{d_r}{dt}\right)_1 \frac{r_e}{r_{e_1}} \int_{t_1}^{t} \frac{dt}{\left(\frac{r_e}{r_{e_1}}\right)^2} \quad . \tag{35}$$

In the Cutler and Hines analysis, the integral on the right is separated into two parts: the first covers the accelerating region between the cathode and anode aperture, the second covers the drift space beyond the anode aperture. The time $t_1 = t_c$, the time at the cathode, is the lower limit.

After the appropriate substitutions and integrations, the first part of the integral becomes:

$$\int_{t_c}^{t_a} \frac{dt}{\left(\frac{r_e}{r_c}\right)^2} = \frac{\bar{r}_c(-\alpha_a)^{2/3}}{\sqrt{2\eta V_a}} \quad A\left(\frac{\bar{r}_c}{\bar{r}_a}\right) \quad , \tag{36}$$

where $\bar{r}_c$, and $\bar{r}_a$ are the radius of curvature of the cathode and anode aperture respectively, α_a is the Langmuir parameter α evaluated at the anode, V_a is the anode potential, and $A\,(\bar{r}_c/\bar{r}_a)$ is a tabulated function of $(\bar{r}_c/\bar{r}_a)$.

In the drift region beyond the anode aperture the beam diverges under the effect of the space charge in the beam. There is in addition the lens effect at the anode aperture, but this will provide only a higher-order modification to the Cutler-Hines trajectory deviation; therefore, the Cutler-Hines deviation is adequate for this application.

For the case of the shielded beam of slowly varying diameter in terms of the beam voltage and current,

$$\frac{d^2 r_e}{dt^2} = \frac{\eta}{2\pi\epsilon r_e} = \frac{\eta I_b}{2\pi\epsilon r_e \sqrt{2\eta V_a}} \quad . \tag{37}$$

When the appropriate values are substituted from the acceleration region, and several changes of variable and integration are performed, a lengthy expression for the integral on the right in Equation (35) is obtained for the beam in the drift region. This expression may be considered for the case $r_e = r_{min}$; that is, r_{min} occurs at the anode exit. That this is a valid assumption is indicated by the small amount of scalloping detected under the Brillouin focus condition described in Section III. Since the condition of zero scalloping can only be achieved if the beam is injected into the magnetic field just at $r_e = r_{min}$, the conclusion is that the beam minimum does occur at or very near the anode exit.

For the axial position at the beam minimum, the complete expression for the trajectory deviation becomes

$$\frac{\Delta r}{\left(\frac{dr}{dt}\right)_c} = \frac{\bar{r}_c}{\sqrt{2\eta V_a}} \left[\frac{r_{min}}{r_c} (-\alpha_a)^{2/3} A\left(\frac{\bar{r}_c}{\bar{r}_a}\right) + 3\sqrt{\frac{\pi}{2}(-\alpha_a)^2} \operatorname{erf} \sqrt{\ln \frac{r_a}{r_{min}}}\right] \quad . \tag{38}$$

The significant thing about this relation is that for the fixed gun design of the STL-100 and fixed beam voltage, the value of the right-hand side is a constant; thus,

$$\Delta r = \frac{K'}{\mu_o} \left(\frac{dr}{dt}\right)_c \quad . \tag{39}$$

This indicates that the trajectory deviation is directly proportional to the transverse perturbation velocity at the cathode and inversely proportional to the beam velocity. Also, though the theory was derived for the case of an initial transverse velocity in the radial direction, it may be shown to apply for off-axis electrons with initial velocities in any transverse direction. This is a consequence of the linear character of the variation of the radial fields with radius under the paraxial-ray assumption. Thus the result applies to all electrons perturbed by the magnetic field of the perturbing coil.

It should also be noted that because of the electrostatic nature of the accelerating fields, an initial transverse velocity in any given plane could be assumed to produce a trajectory deviation in that plane. This further simplifies the task of tracking electrons through the acceleration and drift regions of the gun.

The trajectory deviation of electrons entering the drift region can have both velocity and positional components. It can be expressed in terms of an $\dot{r}_c$ and a $\dot{\theta}_c$ at the cathode plane. These terms do not represent actual velocities at the cathode surface, but are mathematical equivalents which give the trajectory deviation at the anode exit.

Ideally, when the perturbed electron trajectories are extrapolated from the anode exit back to the cathode plane according to the preceding

theory, they should all intercept the cathode plane at a common point. Because the perturbing field is solenoidal, this will not occur. As a result, the "local" perturbation assumed at the cathode is, in terms of the electron motion in the beam, rather diffuse.

Some typical transverse velocities at the cathode surface are shown in Figure 27. These velocities were determined by considering the forces on an electron moving through the perturbing field. The diffuse nature of the source of the perturbations is shown. In fact, the perturbed area accounts for something approaching one-quarter of the cathode area. Because the field of the perturbing coil is confined near the coil axis and because it falls to low levels rather quickly, the diffusion is not so severe that this method of perturbing the electrons is not valid.

Now that the motion of perturbed electrons through the accelerating region of the electron gun is understood, the motion of the perturbed electrons in the beam may be described. For this treatment the laminar equa-

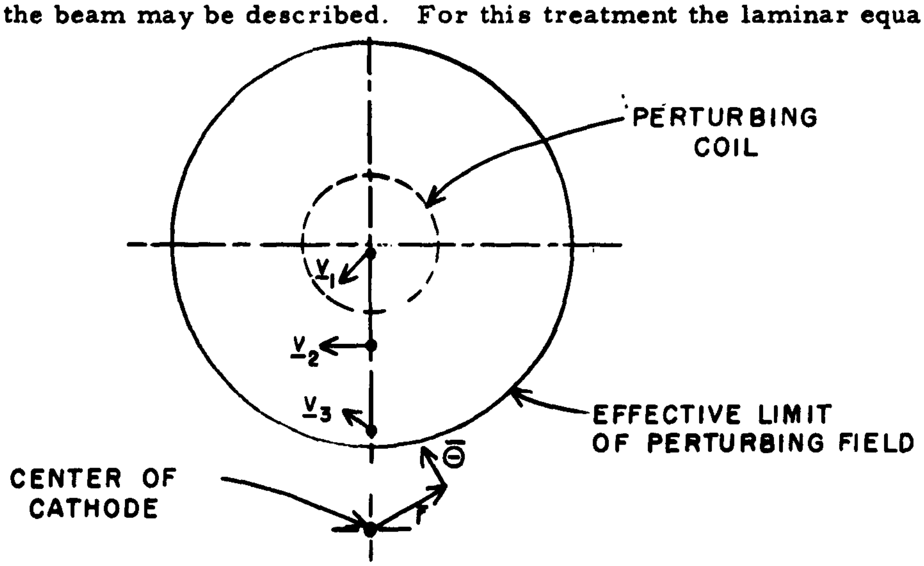

Figure 27. Typical Transverse Velocities Given to Three Electrons by the Perturbing Coil.

tion of motion previously derived will be used. This treatment is based on the so-called "translaminar theory" of a few translaminar electrons in a laminar stream used by Brewer,[6] and also used in this report to explain the anomalous scallop wavelength observed by Gilmour.[3] The assumptions are (1) that the perturbed electrons do not disturb the essential laminarity of the electron beam and (2) that they remain within the beam.

The solution to Busch's theorem, Equation (8), then becomes,

$$mr^2\dot{\theta} = er\, A_\theta - er_c\, A_{\theta_c} + mr_c^{\,2}\ \dot{\theta}_c \quad , \tag{40}$$

or

$$\dot{\theta} = \omega_L \left(1 - \frac{g^2}{r^2}\right) + \frac{r_c^{\,2}}{r^2}\ \dot{\theta}_c \quad . \tag{41}$$

When the additional term, $\frac{r_c^{\,2}}{r^2}\ \dot{\theta}_c$, is carried through, the necessary algebra for the case $g = o$, Equation (16) becomes,

$$\ddot{R} + \omega_L^{\,2} \left[R \left(1 - \frac{R_c^{\,4}}{R^4} \quad \frac{\dot{\theta}_c^{\,2}}{\omega_L^{\,2}} \right) - \frac{1}{R} \right] = 0 \quad . \tag{42}$$

This shows that the $\dot{R}_c$ component of the perturbation does not influence the radial frequency of oscillation of the electrons. An electron with a purely $\dot{R}_c$ component at the cathode plane ($\dot{\theta}_c = 0$ for this electron) will oscillate about the laminar trajectory and remain in a constant phase relationship with it. An electron with a $\dot{\theta}_c$ component, on the other hand, will not oscillate in the radial direction with the same frequency as the laminar electron. This will give rise to a "wash-out" of the perturbation with axial position, which will become more severe as $\dot{\theta}_c$ increases.

Since the term $\dot{\theta}_c$ is squared, it might appear that the sign of this term would not affect the radial frequency of oscillation. This would be

occur only if the sign of $\dot{\theta}_c$ did not affect the axial velocity of the electron. The sign of $\dot{\theta}_c$ does affect the axial velocity,[18] however, so this effect must be considered. Since the perturbing coil used was not on the beam axis, both positive and negative signs of θ_c were given to perturbed electrons. Although detailed calculations were not made, the change in axial velocity arising from the different signs of θ_c would increase the rate of wash-out of the perturbation above that expected from Equation (42) alone.

2. With Focusing Field Threading the Cathode

Since for this study the conditions investigated were near Brillouin flow, the case of flux threading the cathode can be considered as a perturbation of the previously treated case. When $R_g \neq 0$, Equation (16) becomes:

$$\ddot{R} + \omega_L{}^2 \left\{ R \left[1 - \frac{R_g^4}{R^4} \left(1 - \frac{\dot{\theta}_c}{\omega_{L_c}} \right)^2 \right] - \frac{1}{R} \right\} = 0 , \qquad (43)$$

where $\omega_{L_c} = \dfrac{\eta B_c}{2}$.

This indicates that the presence of flux threading the cathode can affect the motion of the perturbed electrons. The sign of $\dot{\theta}_c$ alters the oscillation frequency about the laminar trajectory. Since both signs of $\dot{\theta}_c$ existed in the beam, the perturbation washed out more quickly when flux threaded the cathode. Again the velocity variation with $\dot{\theta}_c$ will exist, as when flux does not thread the cathode.

D. EXPERIMENTAL OBSERVATIONS

1. Pulse Applied to Perturbing Coil

The resistance of the coil at a cathode temperature of 825 degrees Centigrade was very nearly 1/4 ohm. The power dissipated by this coil under d-c operating conditions at a current of 12 amperes would have been too large to be practical. Since the cathode was pulsed at a .001 duty cycle, it was possible to pulse the perturbing coil in synchronism with the cathode pulse at very nearly this duty cycle. This reduced the average power dissipated by the perturbing coil to less than 3/4 watt, which was a negligible fraction of the heater power of 68 watts.

The pulse applied to the perturbing coil was synchronized with the cathode pulse,which occurred at a repetition rate of 60 cycles per second. The pulse duration of the cathode pulse was 16.7 microseconds, but a coil pulse duration of up to 100 microseconds was the design goal to allow for the use of longer pulse durations and the possibility of poor rise and fall times of the perturbing coil pulse.

A pulse transformer was used to match the extremely low impedance of the perturbing coil to a cathode follower. This transformer also provided d-c insulation between the cathode and pulsing network. A flash shield was provided to protect the primary windings from a breakdown of the insulation of the secondary windings.

A schematic of the pulsing network is shown in Figure 28. The modulator was equipped with a 60-cps sine-wave output with the phase variable with respect to a zero of the heater current. This signal was used to trigger the pulse generator in the modulator. The phase of the sine-

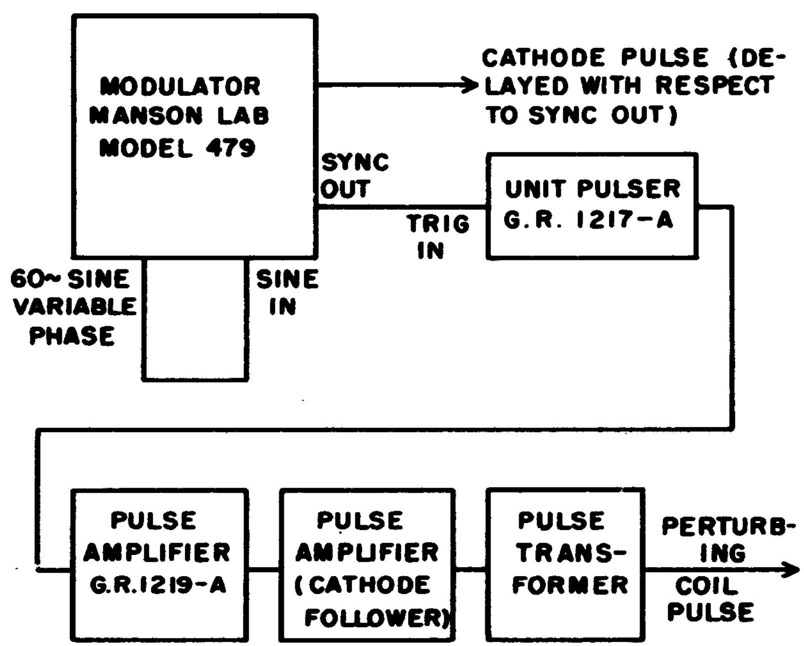

Figure 28. Schematic of Pulsing Network.

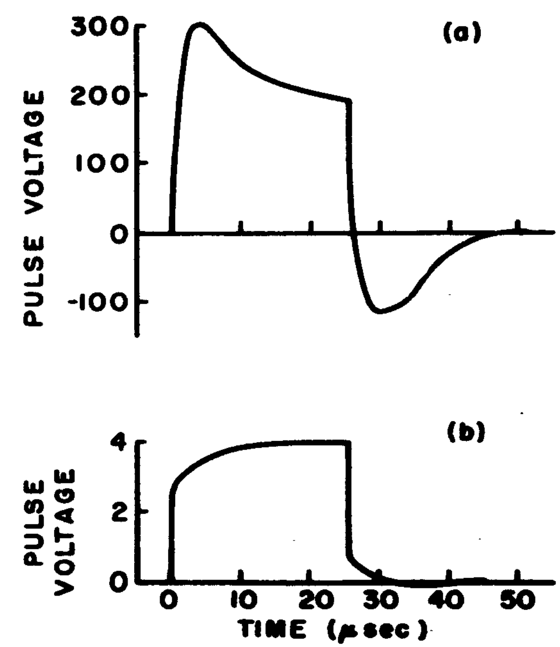

Figure 29. Perturbing Coil Pulse Waveforms: (a) Pulse on Primary of Pulse Transformer, (b) Pulse on Secondary of Pulse Transformer.

wave trigger was adjusted to make the cathode pulse occur at a zero of the heater current. The synchronous output of the modulator was used to trigger the perturbing coil pulse. A delay line with up to 14 μsec total delay in 1.4 μsec steps was installed in the pulse generator of the modulator to allow the cathode pulse to be delayed with respect to the synchronous output. This allowed for the circuit delays in the perturbing-coil pulsing circuit and for the rise time of the perturbing-coil pulse.

A General Radio pulser and pulse amplifier were used to generate the pulse perturbing the coil. A cathode follower was needed following the General Radio pulse amplifier to provide the necessary power to the perturbing coil. This amplifier had been constructed at Cornell for another experiment. A 20-ampere pulse applied to the perturbing coil with a pulse duration of up to 100 μsec was produced. The vibration of the coil leads at the vacuum seal induced by the varying current limited the pulse current to this value for safe operation. Figure 29 shows the pulse waveforms on the primary and secondary of the pulse transformer for a 25-μsec pulse.

2. Observations on the Perturbed Beam

The perturbation was observed on the beam cross section by scanning the beam twice, once with the perturbing coil current turned on and once with the current turned off. The cross sections were superimposed on the x-y recorder so that the two results could be compared and the perturbation could be easily seen.

When the beam was pulsed, the full coil current (12 amperes) was required to obtain a measurable perturbation. This precluded varying the current to detect a possible change in the magnitude and behavior in the beam. It was originally hoped that the unperturbed beam could be evaluated

by extrapolating to zero the results obtained by perturbing the beam at several values of coil current.

The behavior of the perturbed beam was as expected. The perturbation was observed over a distance of six to eight inches from the anode exit. In this region it seemed to rotate about the axis at roughly the Larmor angular velocity. Beyond this point the perturbation washed out. This behavior would be expected from the previous theoretical discussion. At a distance of 16-18 inches from the anode exit two perturbations appeared on the beam on opposite sides of the beam center. (That two localized perturbations were seen was a little surprising and has not been explained.)

The coil was modulated with a 500 kc/s r-f signal detected with a receiver in order to increase the sensitivity of the measurements. The higher harmonics of the beam pulse made detection of the perturbation impossible with this technique.

E. RECOMMENDATIONS FOR FUTURE STUDY

This method of probing the beam has shown some promise. In order to obtain useful results, however, some improvements in the detection sensitivity must be made.

1. Perturb alternate pulses of the beam. This would put a 30-cycle perturbation on the beam. A low-pass filter in series with the detected beam current will allow the 60-cycle beam-pulse component to be eliminated. This 30-cycle perturbation could be amplified and visually displayed on an oscilloscope to obtain much greater sensitivity than the method described in Section D. A circuit for perturbing alternate pulses of the electron beam has been built and a schematic of it is shown in Figure 30.

2. Use a smaller pin-hole. If a .002 in. or .003 in. pinhole is used instead of the .005-inch pinhole used in taking data thus far, the amount of trajectory deviation required would be much less. This should allow the maximum benefit to be obtained from the increase in sensitivity described above.

3. Investigate the first few inches of beam after the anode exit. Since the perturbation blurs beyond 8-10 inches from the anode exit, the increase in sensitivity and resolution resulting from using a smaller pinhole and perturbing alternate pulses of the beam would be of little value unless measurements were taken close to the anode exit.

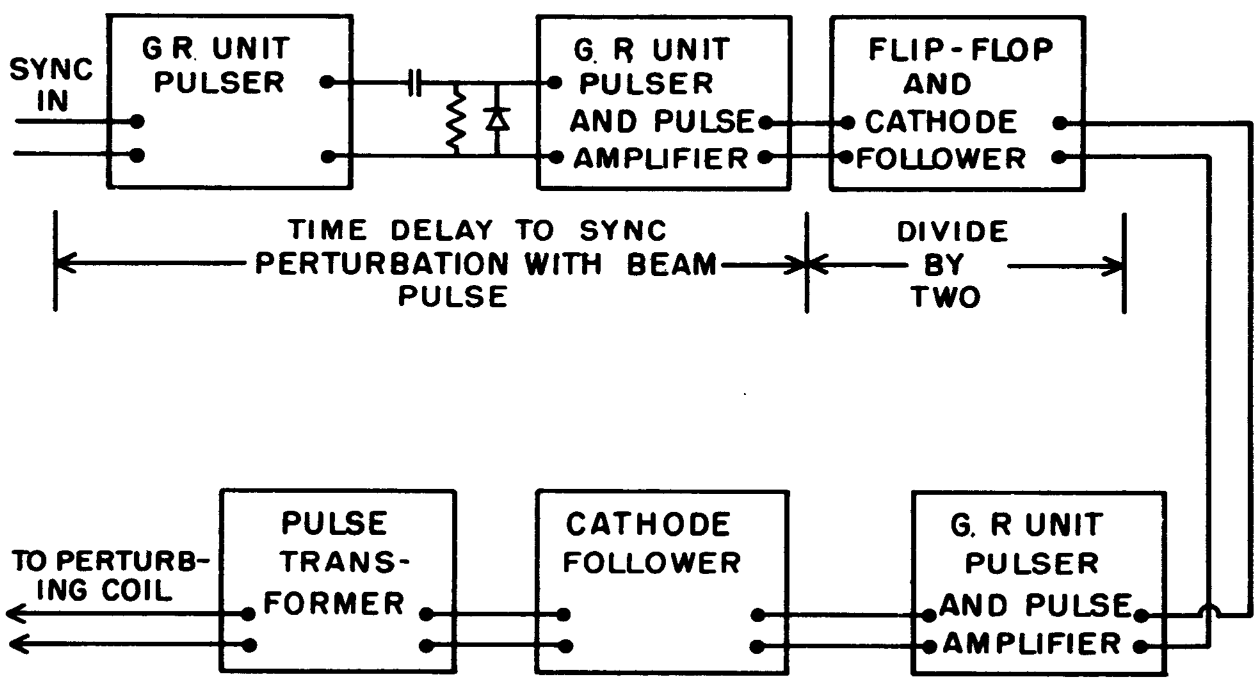

Figure 30. Circuit for Perturbing Alternate Beam Pulses.

REFERENCES

1. A. S. Gilmour, Jr., "The Velocity Distribution in a Velocity-modulated Electron Beam from a Shielded Pierce Gun," Research Report EE 507, Cornell University, August 1961.

2. L. Brillouin, "A Theorem of Larmor and its Importance for Electrons in a Magnetic Field, "Phys. Rev., 66, (1945), pp. 260-266.

3. A. S. Gilmour, Jr., "A Beam Tester for Studying the Characteristics of Velocity-modulated Electron Beams," Research Report EE 495, Cornell University, May 1961.

4. C. C. Wang, "Electron Beams in Axially Symmetric Electric and Magnetic Fields," Proc. I.R.E., 38 (February 1950), pp. 135-147.

5. J. R. Pierce, Theory and Design of Electron Beams, New York: D. Van Ostrand, (1949), p. 153.

6. G. R. Brewer, "Some Characteristics of a Magnetically Focused Electron Beam," J. App. Phys., 30 (July 1959), pp. 1022-1038.

7. J. L. Palmer and C. Süsskind, "Effects of Transverse Velocities in Magnetically Focused Cylindrical Electron Beams," in Proc. Int. Conf. on Microwave Tubes, Munich, (June 7 to 11, 1960), New York: Academic Press, (1961), pp. 456-460.

8. R. D. Frost, O. T. Purl, and H. R. Johnson, "Electron Guns for Forming Solid Beams of High Perveance and High Convergence," Proc. I.R.E., 50 (August 1962), pp. 1800-1807.

9. W. W. Rigrod, "Noise Spectrum of Electron Beam in Longitudinal Magnetic Field," Bell Sys. Tel. Jour., 36 (July 1957), pp. 831-889.

10. T. G. Mihran, "Scalloped Beam Amplification," Trans. I.R.E., ED-3 (January 1956), p. 32.

11. J. R. Pierce and L. R. Walker, "Brillouin Flow with Thermal Velocities," J. App. Phys., 24 (October 1953), p. 1328.

12. C. C. Cutler and J. A. Saloom, "Pin-Hole Camera Investigation of Electron Beams," Proc. I.R.E., 43 (March 1955), pp. 299-306.

13. G. F. Herrman, "Optical Theory of Thermal Velocity Effects in Cylindrical Electron Beams," J. App. Phys., 29 (February 1958) pp. 127-136.

14. H. F. Webster, "Structure in Magnetically Confined Electron Beams," J. App. Phys., 28 (December 1957), pp. 1388-1397.

15. A. Askin, "Electron Beam Analyzer," J. App. Phys., 28 (May 1957), pp. 564-569.

16. A. S. Gilmour, Jr., Private Communication.

17. C. C. Cutler and M. E. Hines, "Thermal Velocity Effects in Electron Guns," Proc. I.R.E., 43 (March 1955), pp. 307-315.

18. J. L. Palmer, "Laminar Flow in Magnetically Focused Electron Beams," Trans. I.R.E., ED-6 (July 1959), pp. 262-269.

ION EFFECTS IN A BRILLOUIN BEAM

A. S. Gilmour, Jr. and D. D. Hallock

School of Electrical Engineering
CORNELL UNIVERSITY
Ithaca, New York

RESEARCH REPORT EE 545

ION EFFECTS IN A BRILLOUIN BEAM

A. S. Gilmour, Jr. and D. D. Hallock

LINEAR BEAM MICROWAVE TUBES

Technical Report No. 22 20 October 1962

Published under Contract No. AF30(602)-2573
Rome Air Development Center, Griffiss Air Force Base, New York

CONTENTS

ABSTRACT

This report describes some of the effects of ion neutralization of the space charge in a Brillouin beam noted while making d-c and r-f current measurements with an electron beam analyzer. Ion neutralization made the beam behavior depart from the ideal Brillouin behavior, resulting in a difference between theory and experiment. As ion neutralization was reduced, the experimental observations approached the theoretical predictions more closely. Ion neutralization was observed by injecting gas into the beam analyzer, on which the measurements were made, and observing the change in beam shape by measuring the current density at various points in the beam on an oscilloscope and an x-y recorder. The beam shape changed during the cathode pulse, indicating a build-up of ions, the rate of ion formation being a linear function of time during the pulse and varying with pressure. The presence and formation of ions in the beam seemed to increase the degree of nonlaminarity of flow.

I. INTRODUCTION

In the course of the investigations of the electron flow in Brillouin beams described in other Cornell University research reports[1-3] the effect of ion neutralization of the space charge in the beam was observed. The purpose of this report is to present these observations in a useful and meaningful form. Ion neutralization made the beam behavior depart from the ideal laminar behavior, on which r-f theories are based. This difference between the theoretical predictions and experiment was not, in fact, due to a deficiency in the theory; for as ion neutralization was reduced, the experimental observations approached the theoretical predictions more closely.

The simple, qualitative treatment given by Harman[4] of the production of ions by the electron beam was used to predict the degree of ion neutralization in the beam and was shown to be valid.

Cutler and Saloom[5] reported that the creation of positive ions in the beam caused the current density on the beam axis to increase during the pulses and caused the beam edge to move inward toward the axis. Section III describes similar effects of ion neutralization on the beam shape observed in this experiment. The effect on the "tails" of the beam of varying the pressure in the gun is also shown.

II. QUALITATIVE TREATMENT OF ION FORMATION

The effect of ionization of the residual gas in a vacuum tube on the beam behavior is not treated exactly because of the large number of variables involved. Some values can be obtained from equations given by Harman,[4] which predict the magnitude of the ion effects, and this was done for the beam analyzer used at Cornell University. There were certain limitations imposed by the experiments, which rendered an exact analysis of the ionization problem impossible. The most serious of these was that the composition of the gas in the analyzer was not known; in fact it was not even known whether the composition remained constant while the analyzer was in operation and the control rods were being moved in and out of the drift region.

From Harman's[4] equations (5.72) and (5.73), we have for the electron density,

$$\text{electrons}/\text{cm}^3 = 3.7 \times 10^9 \quad , \qquad (1)$$

for the beam parameters used in this experiment; and for the gas molecule density,

$$\text{molecules}/\text{cm}^3 = 6.4 \times 10^9 \quad , \qquad (2)$$

for a pressure of 2×10^{-7} mm Hg. This shows that these two densities were comparable in this experiment.

The densities of gas molecules and electrons were not as high as the numbers might indicate, for the mean free path of an electron in the analyzer was of the order of 10^3 meters. The calculation of the mean-free path was based on the assumption that the residual gas was largely oxygen, carbon monoxide, and nitrogen. These have been shown to be prominent among the

residual gases in many vacuum tubes. The importance of this estimate of the mean-free path is that it is much greater than the cathode-to-collector spacing in the analyzer, so that most of the electrons did not suffer collisions with gas molecules in transit. Even when a collision did take place, the probability of ion formation was rather small, probably of the order of one-third to one-tenth of the collisions producing an ionized molecule. Those ions formed were primarily positive ions resulting from an outer shell electron being separated from the atom.

As a result of the long mean-free path and the low probability of ionization, the rate of ion production in the analyzer was much smaller than the rate of electron production. The ion density could become comparable to the electron density, however, because the ions remained relatively fixed in position. Harman gives as a typical experimentally determined rate of positive ion production for an unspecified gas:

$$\text{ions/second/cm of beam} \cong \frac{PI}{V} \times 10^{23} , \qquad (3)$$

where P is the pressure in millimeters of mercury, I is the beam current in amperes, and V is the beam voltage in volts. From this equation and the cross section and area of the beam near Brillouin flow, the ion density can be determined. The values calculated are given in Table I.

Table I.
Calculated Values of Ion Density as Function of Time

Time after start of beam pulse (μsec)	1	10	100
Ion density (ions/cm^3)	1×10^7	1×10^8	1×10^9

This shows that after 1 μsec the ion density in the beam was a negligible fraction of the electron density; after 10 μsec the ion density had reached a level at which it could begin to affect the charge density in the beam (and hence the beam shape). This is in agreement with the results reported in the next section. After 100 μsec the ion density shown in Table I was very nearly the electron density shown in Equation (1). Equation (3), from which Table I was derived, does not allow for the removal of ions from the beam region. In fact, a saturation level would be reached beyond which the charge density (or ion density) in the beam would not change.

If zero initial velocity is assumed, simple calculations show that between pulses the ions formed in the beam region diffused to the walls of the drift tube. When the electron charge was removed at the end of the pulse, a collection of positive ions remained in the center of the drift tube. The space-charge forces of the ions caused them to move quickly out of the beam region toward the wall of the drift tube, where they recombined.

III. OBSERVATIONS ON THE BRILLOUIN BEAM

A. Description of the Beam Analyzer

The beam analyzer with which the ion neutralization in the Brillouin beam was observed has been described in great detail in other reports.[1, 3, 6] For an understanding of some of the observations reported here, however, it is necessary to have an understanding of the operation of the beam analyzer and the vacuum system.

A simplified sketch of the beamanalyzer is shown in Figure 1. The electron gun* used for this experiment was a shielded Pierce-type gun of perveance 1.15 x 10^{-6}, which was operated at 5,000 volts. Because of the low average power that could be dissipated by the beam-collecting apparatus, the gun was pulsed at a repetition rate of 60 cps with pulse lengths of 10 — 30 μsec. The ball valve served to isolate the electron gun from the drift tube, so that the drift tube could be opened to allow for changes in its internal structure without contaminating the oxide cathode of the electron gun. The beam was collected on a movable beam scanner in the drift tube. The collecting plate on this scanner was carbonized to reduce the emission of secondary electrons. A small fraction of the beam passed through a pinhole in the collecting plate and was collected at a Faraday cage. By moving the scanner transversely and axially in the drift tube, one could measure the current density at any point in the beam.

The vacuum system of the beam analyzer is shown in Figure 2. The drift tube was the major part of the primary vacuum system. This system was originally pumped with a 20-l/sec diffusion pump, but this was replaced

*This gun was obtained from a Sperry STL-100, one of five donated to the School of Electrical Engineering by the Sperry Gyroscope Company.

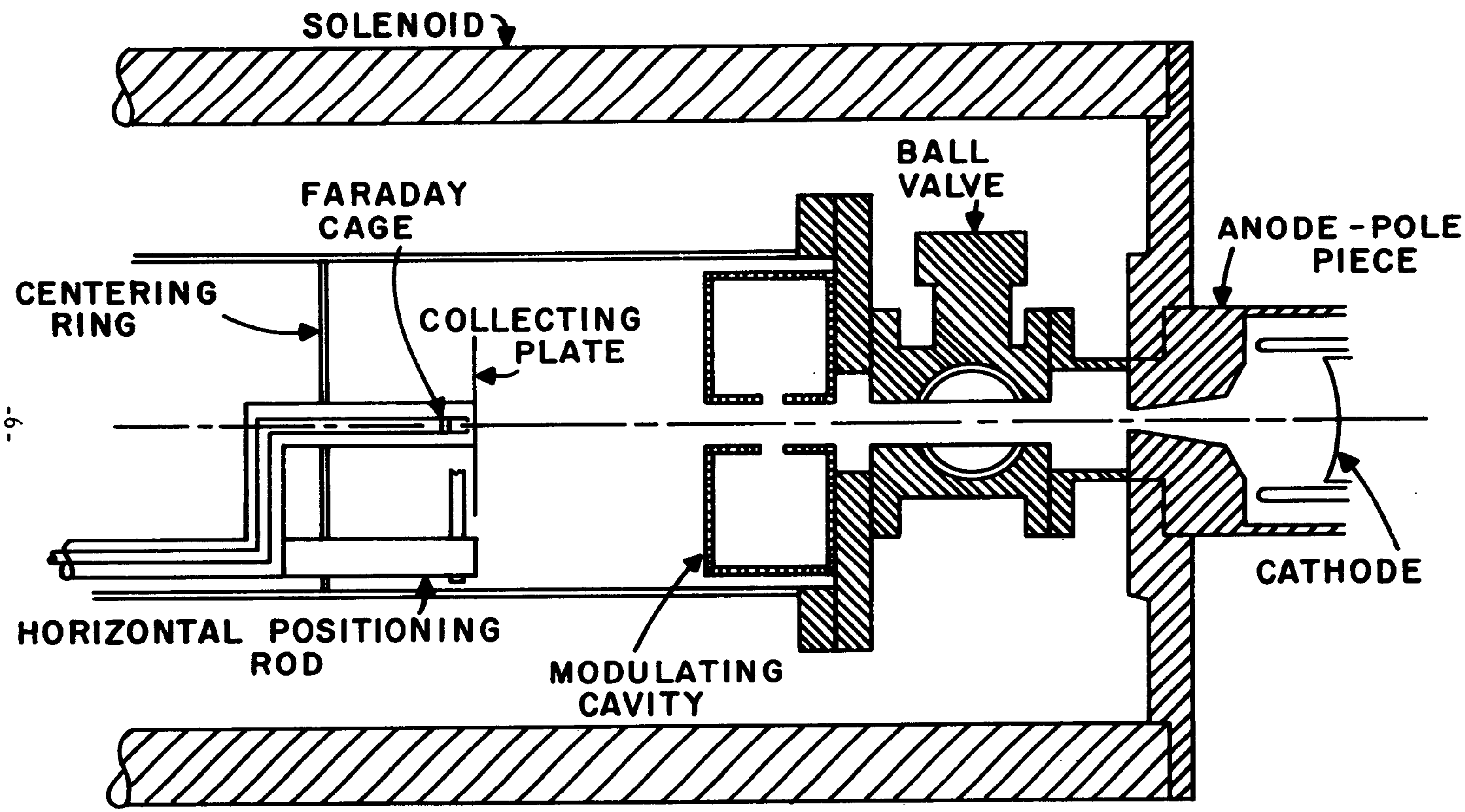

Figure 1. Simplified Sketch of Beam Analyzer.

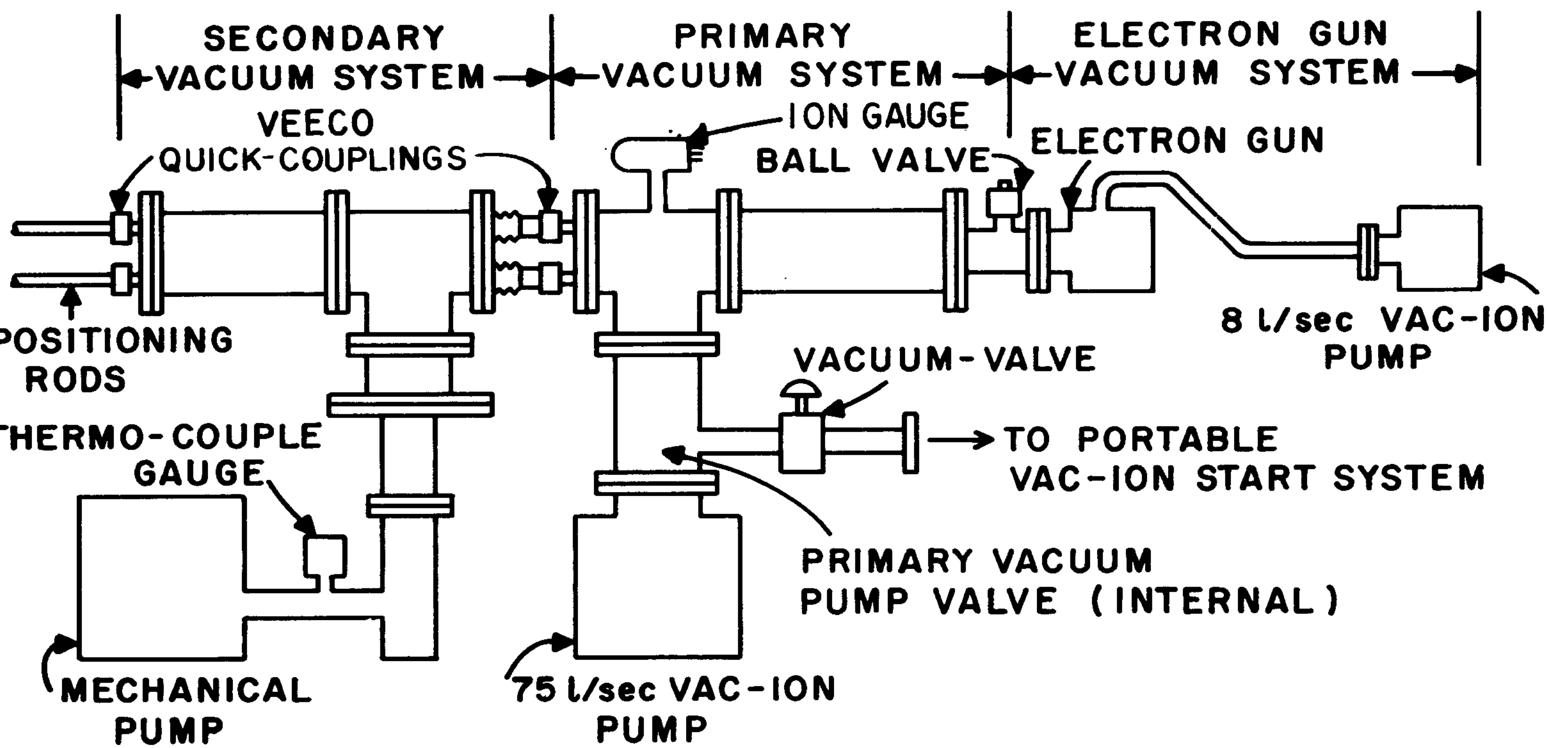

Figure 2. Vacuum System of Beam Analyzer.

with the 75-l/sec VacIon pump shown in the figure to obtain a greater pumping speed and to avoid oil contamination of the internal structure and oxide cathode. Provision was made for independent pumping of the electron gun with an 8-l/sec VacIon pump when the ball valve was closed. The secondary vacuum system served to keep the positioning rods that controlled the beam scanner at a pressure of about 10 microns of atmospheric pressure so that the pressure rise in the primary vacuum system was kept at a minimum when the positioning rods were pushed into the drift tube. The vacuum seals for the positioning rods were sliding O-ring seals.* An ion gauge was attached to the analyzer for measuring the pressure when the primary system was pumped by the oil diffusion pump.

B. Ion Effects Observed in the Beam

The effects of ions were observed when an oscilloscope was used to monitor the electron current arriving at the Faraday cage from the sampling aperture in the beam-collecting plate. Shown in Figure 3 are oscillograms of the cage current at the center of the beam before and after gas was injected into the analyzer (the gas was injected by moving the beam-measuring apparatus rapidly into the analyzer). The oscillogram in Figure 3a was obtained before injecting the gas with the pressure in the analyzer at 2×10^{-7} mm Hg, as indicated by the ion gauge. Immediately after the gas was injected, the pressure indicated by the ion gauge increased to 4×10^{-7} mm Hg and the oscilloscope pattern shown in Figure 3b was obtained. During the succeeding period of about 10 sec, however, while

*Manufactured by Vacuum Electronics Company

the pressure decreased to 2×10^{-7} mm Hg, this pattern changed and returned to that shown in Figure 3a. Shown in Figure 4 are similar oscillograms of the cage current near the edge of the electron beam before and after gas was injected into the analyzer.

Figures 3 and 4 show that the leading edges of the pulses all have the same amplitude and the amplitude of the trailing edge increases at the center of the beam and decreases at the edge of the beam. By plotting the amplitudes of the currents at the leading and trailing edges of the pulse as the sampling aperture was moved horizontally through the beam at the vertical center position of the beam, we obtained the data for the curves shown in Figure 5. These curves clearly show that ions build up in the beam during the pulse and that the ions partially neutralize the negative space charge of the electron beam. Since the magnetic forces tending to compress the beam then become larger than the electrostatic forces that cause the beam to diverge, the diameter of the beam decreases and the density of current at the beam center increases. The nearly linear rate of ion formation indicated by the increase and decrease of current densities in Figures 3 and 4 further substantiates the applicability of Equation (3) during the pulse.

The data used to measure the d-c and velocity-modulated beam was taken by measuring the average current to the Faraday cage as a function of position in the beam. Since an average was used, the effect of ion neutralization was to make the observed beam cross section appear as an average between Figures 5a and 5b. Typical beam cross sections that illustrate this are shown in Figure 6.

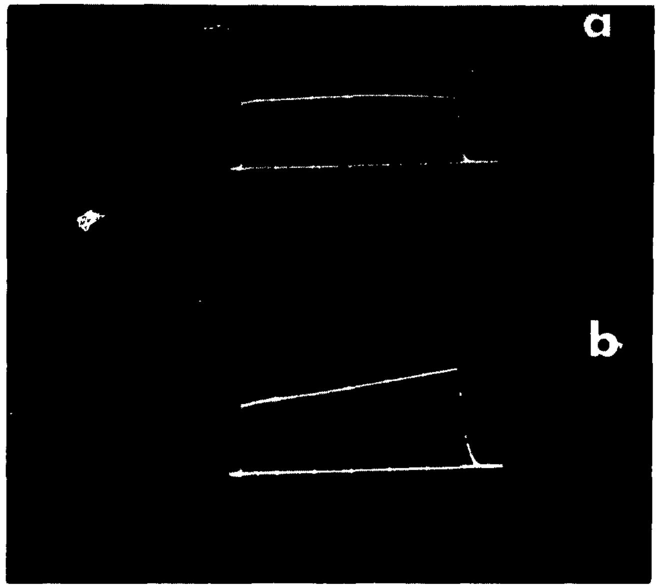

Figure 3. Oscillograms of Current Collected by Faraday Cage at Center of Beam: (a) before Inserting Gas and (b) after Inserting Gas.

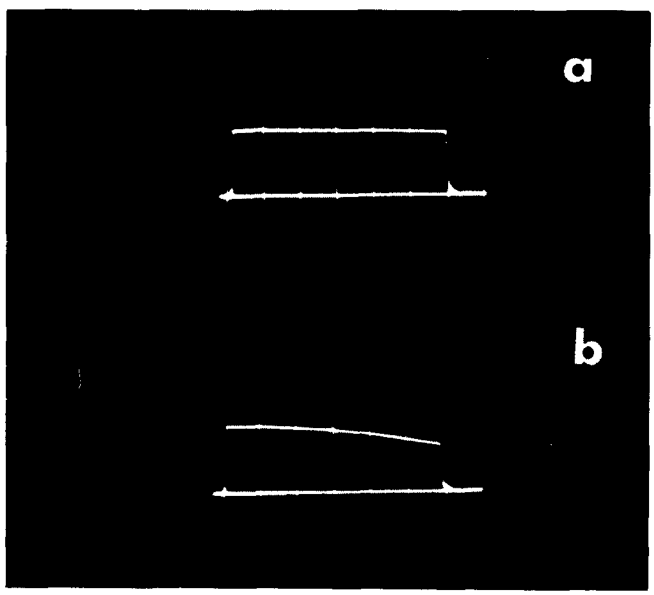

Figure 4. Oscillograms of Current Collected by Faraday Cage at Edge of Beam: (a) before Inserting Gas and (b) after Inserting Gas.

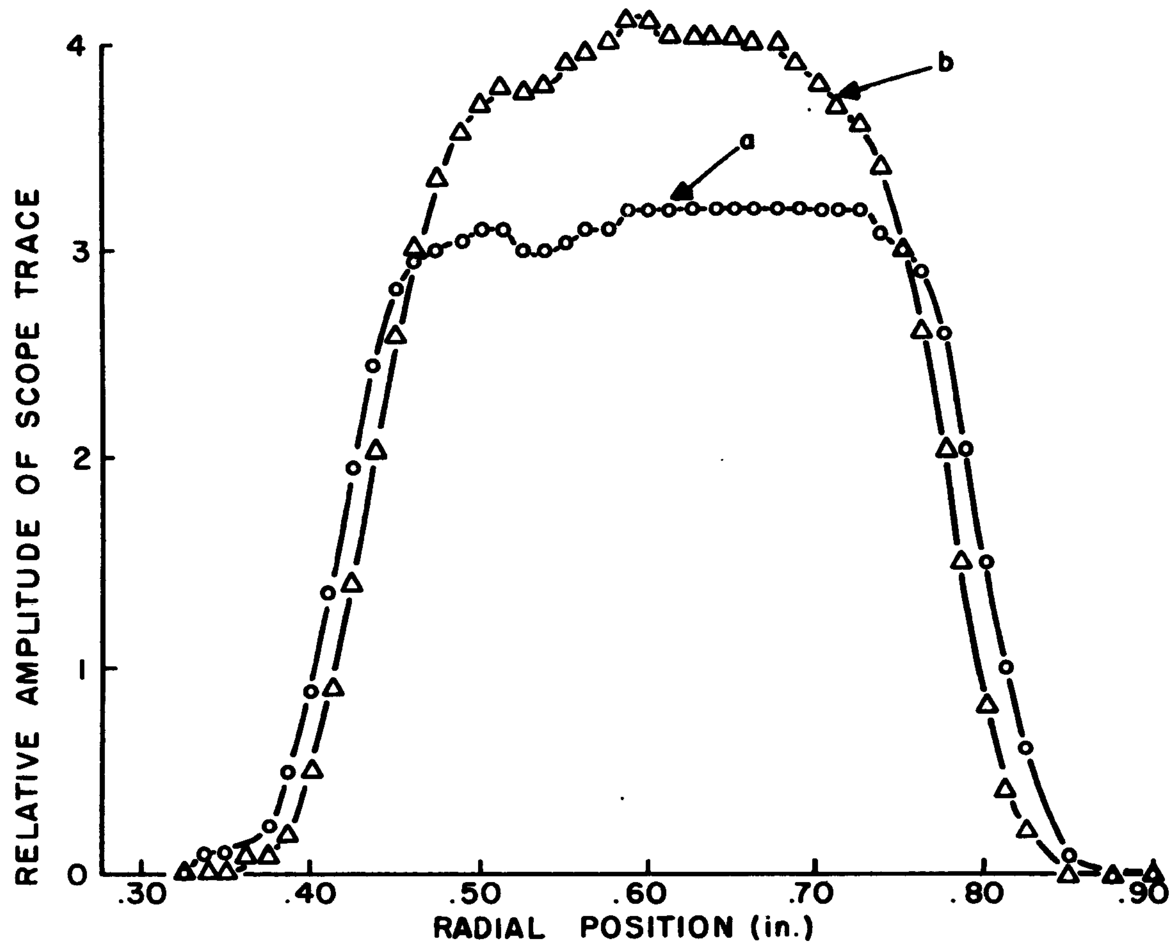

Figure 5. Beam Current Density as a Function of Radial Position of the Sampling Aperture for 30-μsec Pulse: (a) Data from Beginning of Pulse (b) Data from End of Pulse.

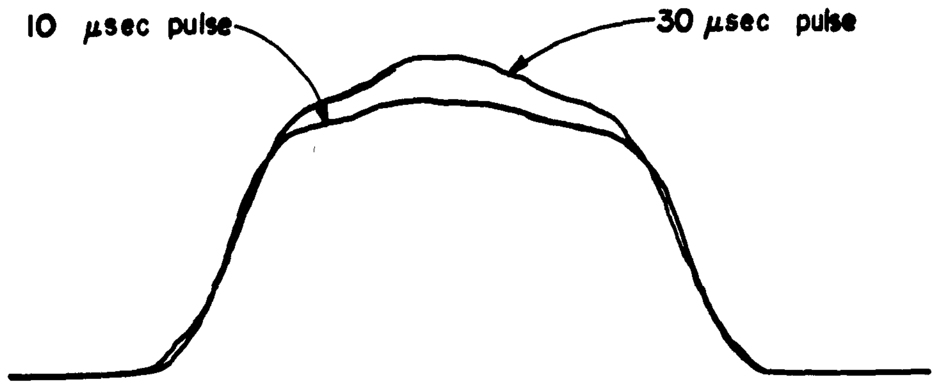

Figure 6. Beam Cross Sections Showing Effects of Ion Neutralization for (a) 30-μsec Pulse and (b) 10-μsec Pulse.

After the results shown in Figure 6 had been obtained, it was noted that there was a region in the electron beam in which some ion neutralization was present, even at indicated pressures below 2×10^{-7} mm Hg, when no gas was being injected into the analyzer. The oscilloscope pattern of the Faraday cage current at the beam center was similar to that shown in Figure 3b at all times. The injection of gas into the analyzer simply increased the slope of the top of the pulse.

This region was the 2 – 4 in. of the drift tube after the beam left the modulating cavity shown in Figure 1, the longer distance occurring when the pressure in the analyzer was the highest. It was concluded that the primary cause of this neutralization was that the drift region through the ball valve and the gun were inadequately pumped when the scanner was positioned close to the modulating cavity. As a result there was a pressure rise in this region, which resulted in a higher degree of ion neutrali-

zation of the beam. This was not indicated by the ion gauge because of its position in the analyzer (see Figure 2).

Because of the ion neutralization in this region resulting from the reduced pumping speed, it was desirable that the pressure indicated at the ion gauge be lower than 2×10^{-7}mm Hg, so that the pressure in the ball valve would not rise above this limit. An improvement in the analyzer performance in this respect was obtained by installing a 75-l/sec VacIon pump as the primary vacuum pump. When this was done it was possible to reduce the indicated pressure to the low 10^{-8}mm Hg range; consequently the degree of ion neutralization was reduced correspondingly when the scanner was within three inches of the modulating cavity.

The electron beam was observed to have low density "tails" surrounding it. The electrons in the tails of the beam used in this experiment had an axial velocity distribution of 95 – 100 per cent of beam velocity.[1] By observing the "tails" of the electron beam both with an oscilloscope and an x-y recorder, it was noted that the amount of current in the tails depended upon the pressure in the electron gun as indicated by the ion pump attached to the gun. It is apparent therefore, that some of the electrons in the "tails" must have originated from the ionization of gas molecules in the electron gun near the cathode. These electrons were accelerated through a large fraction of the beam potential and therefore had the velocity distribution of 95 – 100 per cent of beam velocity, as indicated.

IV. CONCLUSIONS

The effect of ion neutralization of the space charge in a Brillouin beam was noted. It was shown that even under pulsed conditions at what are considered to be high vacuum levels this effect can produce a noticeable change in the beam shape. It was also shown that rather small pressure changes in this high-vacuum region near the critical point, where ion neutralization becomes important, can noticeably affect the beam cross section. Thus with a reduction in pressure of an order of magnitude, ion neutralization will have a negligible effect on the focusing of the beam when this reduction is made in the appropriate range of pressures. The approximate relations given by Harman and simple calculations were shown to be useful in predicting the appropriate range of pressures for a given set of beam parameters. Because of the approximately linear rate of increase of ion formation with time during the pulse, a change in pulse length of an order of magnitude was shown to be equivalent, in terms of the degree of ion neutralization at the end of the pulse, to a change in pressure of an order of magnitude. It was shown that allowances for changes in the effective pumping speed might be necessary when structures are moved inside the vacuum system.

The electrons that appear in the beam "tails" execute radial motion of large amplitude and are therefore nonlaminar. The increase in the current amplitude of the beam tails with increased ion concentration indicates that increasing the formation of positive ions by the electron beam produces some nonlaminarities.

For the beam used in these experiments with a current density of about 2.5 amperes/cm^2, the upper limit for pressure is about 1×10^{-7} mm Hg, if ion neutralization of space charge is not to disturb the beam focusing seriously.

V. REFERENCES

1. A. S. Gilmour, Jr., "A Beam Tester for Studying the Characteristics of D-C and Velocity-modulated Electron Beams," Research Report EE 495, Cornell University, May 1961.

2. D. D. Hallock, "An Investigation of the Laminarity of Flow in a Magnetically Confined Electron Beam," Research Report EE 539, Cornell University, September 1962.

3. A. S. Gilmour, Jr., "The Velocity Distribution in a Velocity-modulated Electron Beam from a Shielded Pierce Gun," Research Report EE 507, Cornell University, August 1961.

4. Willis W. Harman, Electronic Motion, New York: McGraw-Hill Book Co. (1953), pp. 165-172.

5. C. C. Cutler and J. A. Saloom, "Pin-Hole Camera Investigation of Electron Beams," Proc. I.R.E., 43 (March 1955), pp. 299-306.

6. A. S. Gilmour, Jr. and D. D. Hallock, "A Demountable Beam Analyzer for Studying Magnetically Confined Electron Beams," paper presented September 1961 at Proc. Sixth Nat. Conf. on Tube Techniques, to be published by Pergamon Press, N. Y.

CAVITY FIELD PLOTTER

J. E. Goell

School of Electrical Engineering
CORNELL UNIVERSITY
Ithaca, New York

RESEARCH REPORT EE 551

CAVITY FIELD PLOTTER

J. E. Goell

LINEAR BEAM MICROWAVE TUBES

Interim Report 30 October 1962

Published under Contract No. AF30(602)-2573
Rome Air Development Center, Griffiss Air Force Base, New York

CAVITY FIELD PLOTTER

An automated field-plotting system has been built for obtaining curves of electric field strength versus position within a resonant cavity using perturbation techniques.[1] The system will make it possible to obtain accurate and detailed field plots of the fields in complicated structures. Figure 1 shows a block diagram of the system[2] and Figure 2 a circuit diagram of the part of the block diagram outlined by dashed lines.

The operation is based on the shift in resonant frequency of a cavity that occurs when a dielectric, or conductor, is introduced within it. The circuit that has been built produces an output voltage which is proportional to shifts in the resonant frequency. This output voltage is plotted versus position by an x-y recorder.

The signal generator produces a signal whose frequency is a saw-tooth function of time (Figure 3a). Thus, the output of the detector is a "Q" curve (Figure 3b). This signal is amplified and then clipped to remove any noise that might cause false triggering. After being amplified again, the signal is differentiated (Figure 3c). The zero crossing of the differentiated "Q" curve corresponds to the resonance of the cavity. The Schmitt trigger circuit switches from a low- to a high-voltage state as its input goes through zero (Figure 3d). Thus, the output of the following differentiator circuit is a pulse which coincides with the cavity resonance (Figure 3e). This pulse is used to trigger the miltivibrator. The multivibrator pulse operates

1. Edward L. Ginzton, Microwave Measurements, New York: McGraw-Hill (1957), pp. 438-440.

2. This system is patterned after a system developed by the Microwave Tube Division, Sperry Gyroscope Co.

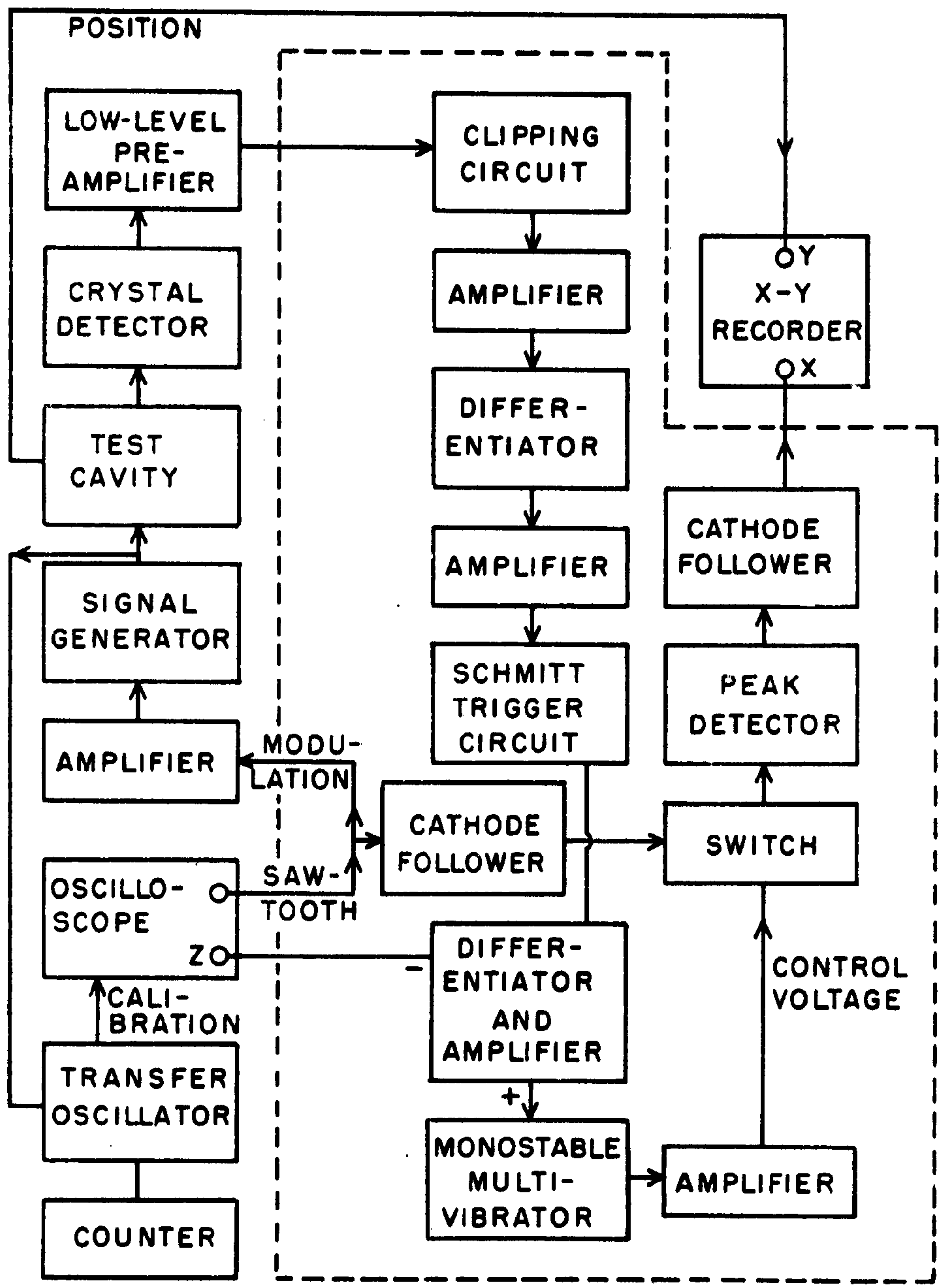

Figure 1. Block Diagram of Field Plotter.

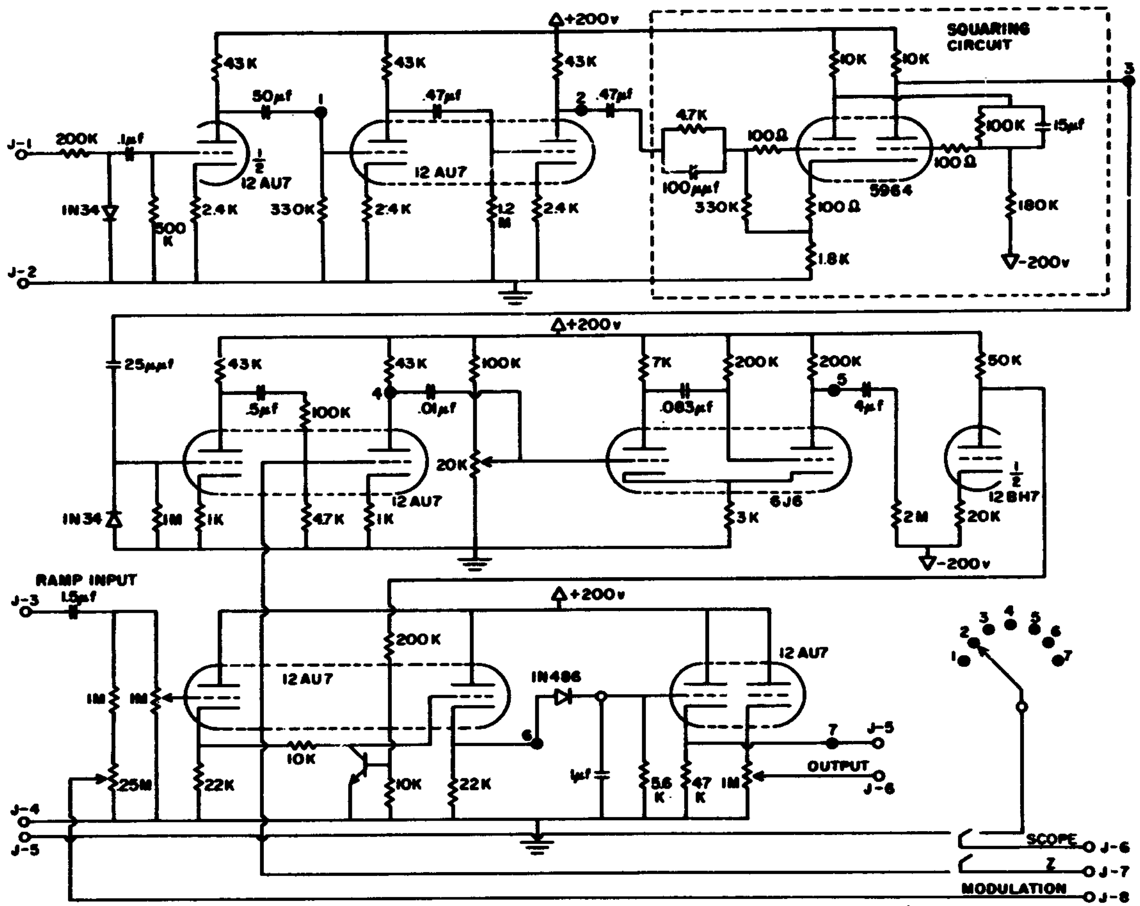

Figure 2. Circuit for Obtaining a Voltage Proportional to the Shifts in Resonant Frequency.

the switch whose output is a portion of the input ramp of fixed width (Figure 3f). If the resonant frequency of the cavity shifts, the portion of the ramp that is peak detected to form the output voltage also shifts. Thus, the output voltage is linearly related to the shift in resonant frequency.

The transfer oscillator and counter shown in Figure 1 are used for calibration. When the center frequency of the swept oscillator is approximately equal to the frequency of one of the harmonics of the transfer-oscillator signal generator, the output of the transfer oscillator is a butterfly pattern whose zero coincides with the time when the frequency of the harmonic is equal to the frequency of the swept-signal generator. This signal is the vertical input to the oscilloscope. The oscilloscope also has an intensity input supplied by the field-plotting circuit when resonance occurs. When the transfer oscillator is adjusted to make the zero of the butterfly pattern coincide with the bright spot on the oscilloscope trace caused by the intensity modulation, the counter indicates the resonant frequency of the cavity divided by an integer. By knowing the approximate resonant frequency or by a comparison of results of adjacent harmonics, one can determine the integer and hence the resonant frequency.

The accuracy of the system is limited to the accuracy of calibration. The calibration system reads to within $\pm$ 4 kc/s of the resonant frequency. Since two points are needed for calibration, the system is accurate to $\pm$ 8 kc/s. Under reasonable conditions of bead and cavity size, shifts of 200 kc/s may be expected. If the system is calibrated on the extremes of the pattern, it will be accurate to within $\pm$ 4 per cent.

Figures 4 and 5 show plots of longitudinal field strength squared versus position for a five-section periodic structure made with the equipment described above.

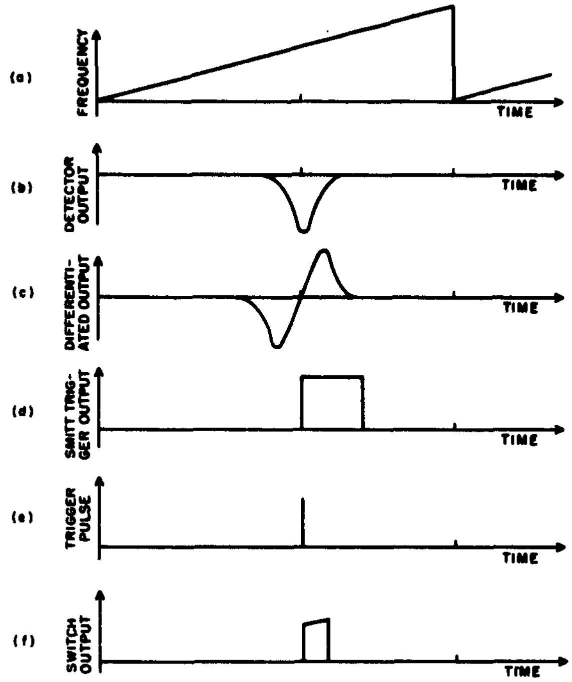

Figure 3. Wave Shapes for the Circuit of Figure 2.

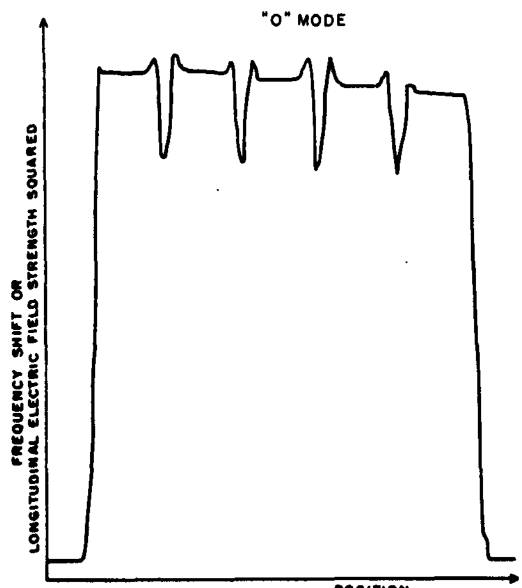

FIG.4

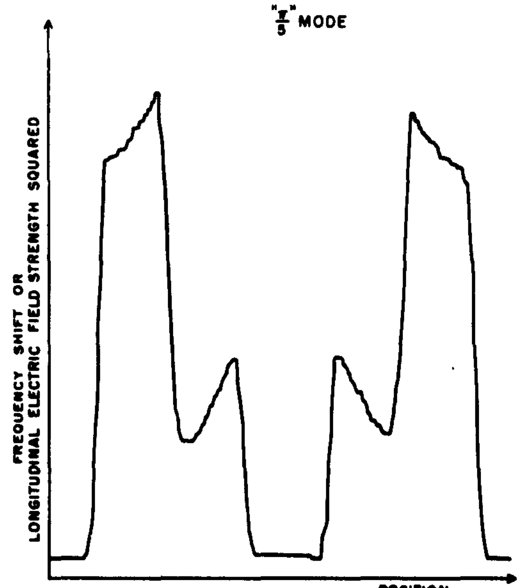

FIG.5

Figures 4, 5. Field Plots for 5-Section Periodic Structure.

INVESTIGATION OF THE EFFECTS OF DRIVING THE MIDDLE CAVITY OF A THREE-CAVITY KLYSTRON

D. Reynolds

School of Electrical Engineering
CORNELL UNIVERSITY
Ithaca, New York

RESEARCH REPORT EE 544

INVESTIGATION OF THE EFFECTS OF DRIVING THE MIDDLE CAVITY OF A THREE-CAVITY KLYSTRON

D. Reynolds

LINEAR BEAM MICROWAVE TUBES

Interim Report 15 October 1962

Published under Contract No. AF30(602)-2573
Rome Air Development Center, Griffiss Air Force Base, New York

CONTENTS

LIST OF SYMBOLS

$-|I_o|$ = average current density in beam

i = a-c current density at location z

i_1 = a-c current density at the end of the first drift space

i_3 = a-c current density entering the third gap

i_{tot} = total current density = $-|I_o| + i$

V_o = d-c beam voltage

V_1 = a-c voltage across the first gap with a positive sign producing a net acceleration of an electron

V_2 = a-c voltage across the second gap with a positive sign producing a net acceleration of an electron

V_{21} = portion of a-c voltage across the second gap resulting from beam current

V_{22} = portion of a-c voltage across the second gap resulting from external drive at the middle cavity

u_o = average beam velocity

u = a-c beam velocity at point z

u_1 = beam velocity at the end of the first drift space

u_{exit} = beam velocity at the exit from the second gap

u_3 = a-c beam velocity entering the third gap

u_{10} = magnitude of velocity modulation impressed upon beam by the first gap

P_1 = power input to first cavity

P_2 = power input to second cavity

P_3 = power output from third cavity

Z_c = magnitude of impedance of middle cavity as seen by the beam

ϕ = impedance angle of middle cavity as seen by beam

θ_1	=	d-c transit angle of the first gap
θ_2	=	d-c transit angle of the second gap
θ_d	=	d-c transit angle of the second drift space
M_1	=	gap-coupling coefficient of the first gap $= \sin \frac{\theta_1}{2} \Big/ \frac{\theta_1}{2}$
M_2	=	gap-coupling coefficient of the second gap $= \sin \frac{\theta_2}{2} \Big/ \frac{\theta_2}{2}$
ω	=	operating angular frequency
ω_p	=	plasma resonant frequency
β_e	=	electronic propagation constant $= \omega/u_o$
β_p	=	plasma propagation constant $= \omega_\rho/u_o$
ρ	=	beam total charge density $= -\lvert\rho_o\rvert + \rho_1$
$-\lvert\rho_o\rvert$	=	average charge density in beam
ρ_1	=	a-c charge density in beam
d_1	=	spacing of first gap
d_2	=	spacing of second gap
d_3	=	spacing of third gap
S_1	=	length of first drift space
S_2	=	length of second drift space

ABSTRACT

This report describes an experimental and theoretical investigation of the effects of driving the middle cavity of a three-cavity klystron. It indicates that drive power levels within a few decibels of the power output of the tube increase the total power output or efficiency no more than proper tuning of the middle cavity. Included are preliminary results of a theoretical study based upon a combination of space-charge waves and first-order ballistic theory.

INTRODUCTION

In the course of development work that resulted in the multiple-beam klystron, Dehn[1] applied power to the middle cavity of a three-cavity klystron and observed that, under some conditions, he obtained an increase in output power of 100w when he applied 100w to the middle cavity. When losses in coupling and in the cavity itself were taken into account, this meant that a power gain was achieved, which could conceivably result in a higher total efficiency for the tube. It was decided to investigate this effect at Cornell to see if it could be reproduced, increased, and explained theoretically.

The original plan was to carry out experimental work on the SAL-36 klystron, a three-cavity klystron rated at a nominal beam voltage of 160 kv peak, with a cathode perveance of one microperv,* and an operating frequency of 840 Mc/s. It was planned to use a relatively high-power traveling-wave tube as a driver for measurements at low power levels and to apply output power from the SAL-36 through a power divider for measurements at higher power levels. Because of experimental difficulties with the SAL-36 system, it was necessary to make measurements on the SAS-61 klystron, a three-cavity klystron operating at S-band (2700-2900 Mc/s). The SAS-61 has a cathode perveance of three micropervs and is designed to operate at a beam voltage of 13 kv with a maximum pulse width of 10 μsec. A major advantage of using this system lay in the possibility of attaining input power levels of the order of the output power of the tube under test by using a sec-

---

* One microperv $= \left(\dfrac{\text{amperes}}{\text{volts}^{3/2}}\right) \times 10^6$

ond SAS-61** tube as a driver. A further advantage was the availability of a wider range of auxiliary equipment at this frequency range.

EXPERIMENTAL RESULTS

The initial portion of the work reported here consisted of an experimental investigation into the effects of driving the middle cavity of a SAS-61 klystron. It was first planned to vary the relative phase of the drive at the middle cavity with respect to that at the first cavity over increments of 30 degrees in phase. It was soon apparent that most of the changes observed were of the order of the experimental error, except at those points where the relative phase was such as to produce minimum output, where a noticeable reduction in output power occurred. Data were therefore obtained at the condition of middle-cavity drive power giving minimum output, and at a point 180 degrees removed in phase from this point.

It was also planned in the beginning to observe the effects of varying levels of middle-cavity drive power. Early observations showed, however, that the output power varied linearly with changes in middle-cavity drive power. Points were therefore taken only for an applied middle-cavity drive power of 1 kw.

Experimental data were obtained on equipment connected as shown in Figure 1. A single modulator was used to drive both the driver tube and the tube under test. It was necessary to operate the modulator at 60 cps to minimize pulse amplitude jitter resulting from voltage variations among

**This was made possible through the kind co-operation of Dr. A. D. Sutherland of the Sperry Gyroscope Company, Gainesville, Florida, who arranged to have a SAS-61 tube donated for the purposes of this experiment.

phases of the supply. R-F drive power was obtained from a reflex klystron and amplified to an appropriate level by a traveling-wave amplifier. This signal was applied to the input cavity of the driver klystron, whose output was split to provide drives for both the first and second cavities of the tube under test. Two attenuators and a coaxial trombone provided virtually independent control of signal amplitude and relative phase.

Various directional couplers were connected as indicated in Figure 1 to allow measurement of forward and reflected power at all three cavities of the tube under test. An additional directional coupler was inserted in the input to the first cavity of the tube under test to provide a phase reference signal. A slotted line in the input to the middle cavity allowed selection of a comparison signal for determination of relative signal phase. The slotted line was equipped with a r-f adaptor instead of the usual crystal. Its output was combined with the output taken by directional coupler in the feed to the first cavity. The combination was mixed with a local-oscillator signal, and the detected output was amplified and displayed on an oscilloscope. A phase difference introduced by changing the length of the trombone could be measured by the shift in position of the slotted-line carriage necessary to obtain a null indication. This technique was described fully in an earlier report.[2]

Since the SAS-61 klystron is designed for pulse operation, it was necessary to measure peak power. This was accomplished by placing a calibrated attenuator before a crystal and displaying the crystal output on an oscilloscope. An absolute reading was obtained by comparing the reading from this device with that from a power bridge on the c-w r-f output of the traveling-wave tube. The change in attenuation necessary to reach the same voltage level on the oscilloscope display was a measure of the change in

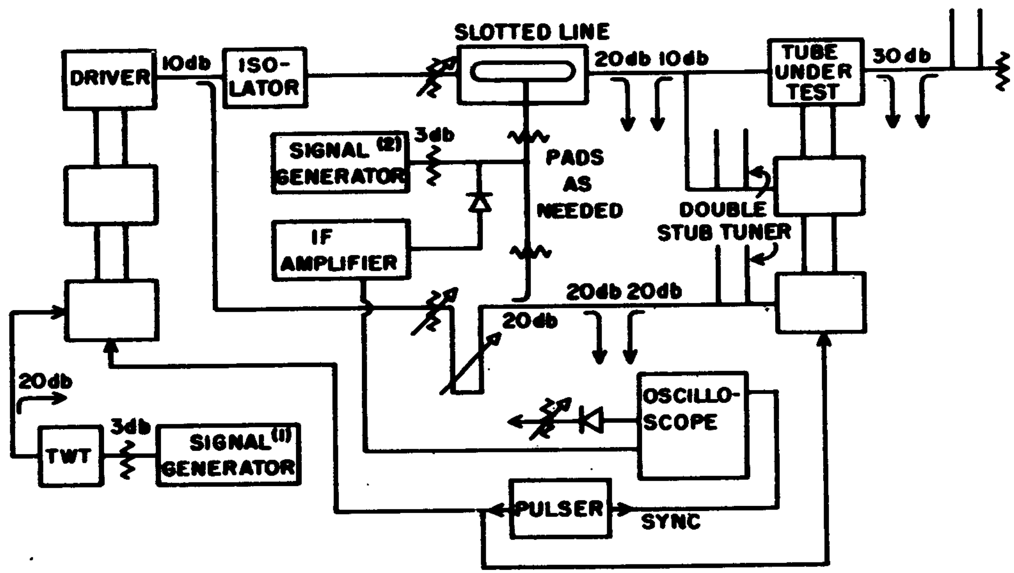

<u>Driver and Tube under Test</u> - Sperry SAS-61 three-cavity klystrons. 2700-2900 Mc/s, nominal operating voltage 13kv, maximum pulse length 10μsec.

<u>Isolator</u> - Ferrite, cascade model

<u>Signal Generator</u> - (1) Sperry Microline using a 417-A reflex klystron (2) Polarad Microwave (S-band)

<u>TWT</u> - RCA 4010 traveling-wave tube

<u>I-F Amplifier</u> - General Radio Unit

<u>Slotted Line</u> - Hewlett-Packard 810A

<u>Oscilloscope</u> - Tektronix 585 with high-gain preamplifier

<u>Pulser</u> - Capable of supplying d-c to tube heaters and variable pulses synchronized to line frequency with peak voltages to 20kv, variable pulse width.

<u>Note</u> - Numbers indicate magnitude of fixed attenuators or of the coupling ratio for directional couplers.

Figure 1. Modified Block Diagram of Test Equipment for Investigating Effects of Middle-Cavity Drive.

power level of the unknown signal from the reference level.

The large number of cascaded voltage-sensitive elements of the experimental circuit resulted in excessive sensitivity to small variations in line voltage. A series line-voltage regulator solved this problem for all equipment except the modulator, which required three-phase power. Variation in the pulse amplitude of the modulator was finally controlled by installing a differential amplifier to control bias on the charging tetrode according to an error signal produced by comparing a portion of the output signal with the voltage across a gas voltage-regulator tube. Before the addition of the differential-amplifier circuit, pulse voltage on the driver and on the tube under test was observed to vary more than 500 v with normal line-voltage ripple. After the change, the variations were observed to be less than one per cent.

In addition to measurements of power inputs and outputs and of relative phase, various incidental measurements were necessary. These included a check on the perveance of the tube under test and information sufficient to determine cavity Q's under the effects of beam loading. Voltage points for determining perveance were obtained from oscilloscope measurements of pulse voltage with a viewing resistor, and current points were calculated from the duty cycle and the indicated average current. The duty cycle was set at 6×10^{-4} through the use of a line-synchronized 60-cps repetition rate and the maintenance of a 10-μs pulse width. Pulse width was set by adjusting first-cavity drive power to give a desired peak output power and then adjusting pulse width to provide the corresponding reading of average power on a power bridge.

Information sufficient to determine cavity Q's was obtained by using reversed directional couplers and measuring direct and reflected power with

the device described for measuring peak power. The conventional methods of making this determination were not possible because it was necessary to make measurements only when the pulse was on.

It can be seen from Figure 1 that a double-stub tuner was placed at the input to the middle cavity. This was necessary because in the SAS-61 the input loop at the middle cavity is intended as a sampling loop only, and is highly undercoupled as would be expected. The double-stub tuner was inserted to provide the best possible match to the middle cavity. All determinations of middle-cavity drive power were made with this tuner adjusted to minimize reflected power.

Figures 2 through 6 show power output plotted as a function of first-cavity drive power for middle-cavity drive power at zero, at 1 kw in the most favorable phase, and at 1 kw in the most unfavorable phase. The parameter

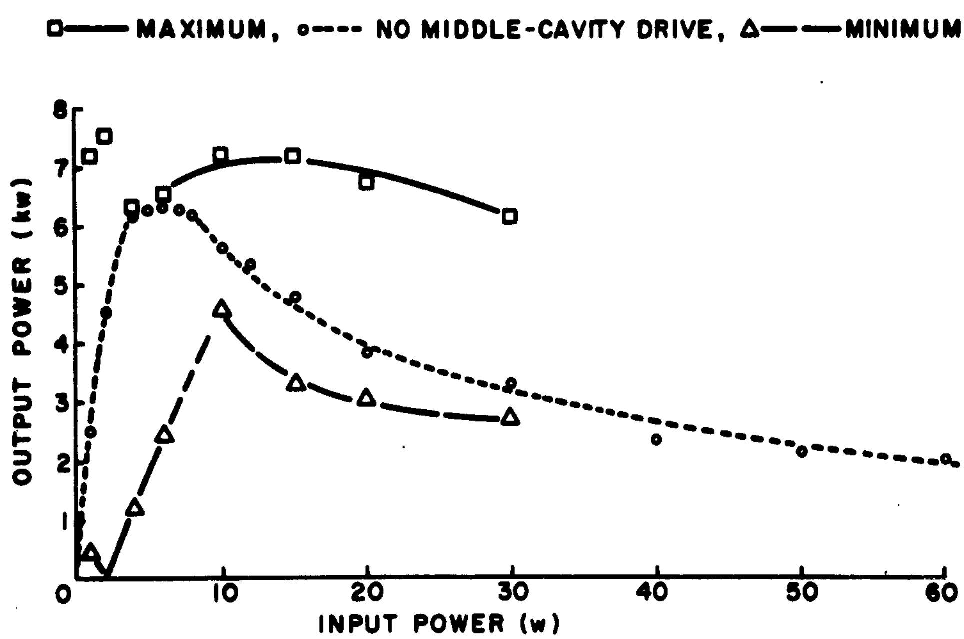

Figure 2. Gain Curve of SAS-61 Klystron with Middle Cavity Tuned for Maximum No-Drive Output at 200 mw (Synchronous); 1 kw to Middle Cavity.

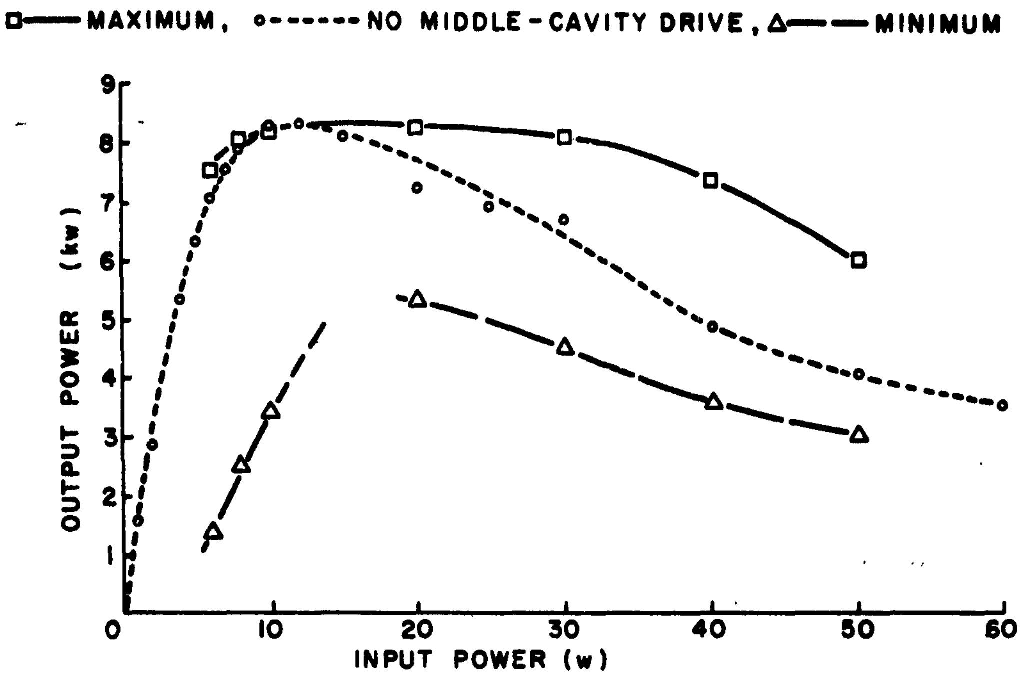

Figure 3. Gain Curve of SAS-61 Klystron with Middle Cavity Tuned for Maximum No-Drive Output at 10-w Drive; 1 kw to Middle Cavity.

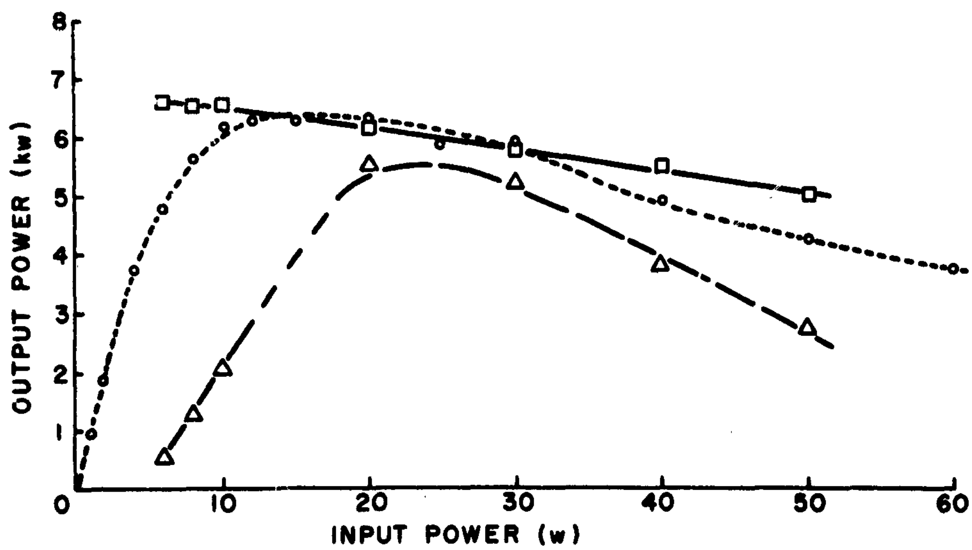

Figure 4. Gain Curve of SAS-61 Klystron with Middle Cavity Tuned for Maximum No-Drive Output at 20-w Drive; 1 kw to Middle Cavity.

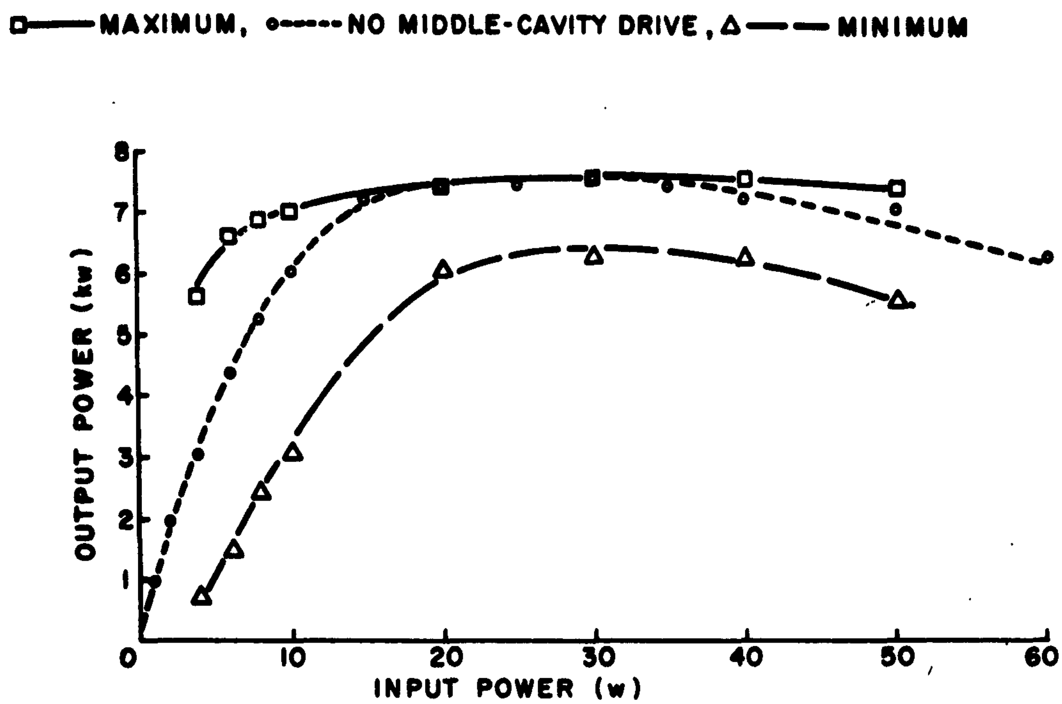

Figure 5. Gain Curve of SAS-61 Klystron with Middle Cavity Tuned for Maximum No-Drive Output at 30-w Drive; 1 kw to Middle Cavity.

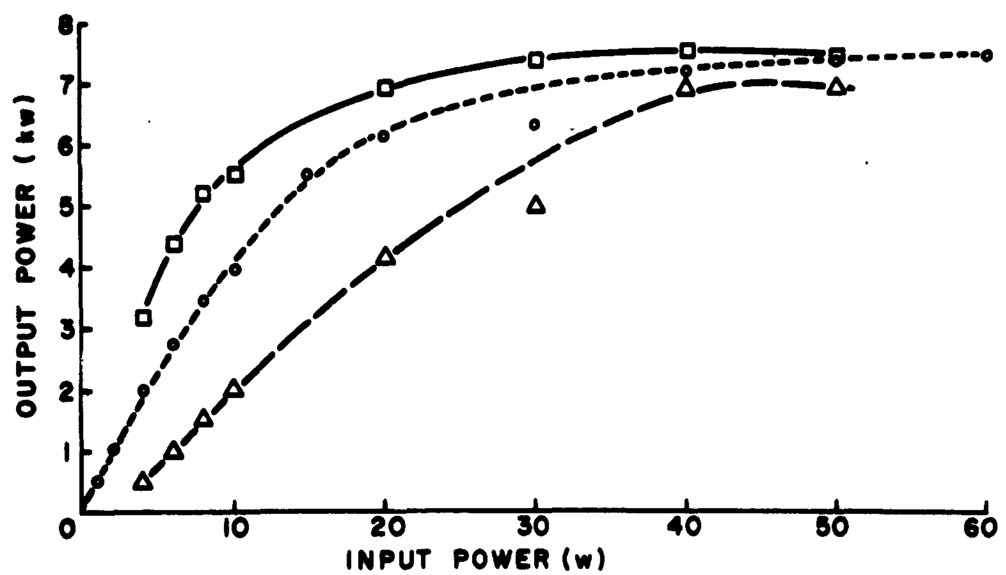

Figure 6. Gain Curve of SAS-61 Klystron with Middle Cavity Tuned for Maximum No-Drive Output at 50-w Drive; 1 kw to Middle Cavity.

is middle-cavity tuning. It will be seen that the effect of driving the middle cavity in favorable phase is to increase the output power whenever the middle cavity is tuned below the frequency at which output power is optimum at that particular level of first-cavity drive power. At no time, however, is the increase greater than the amount which could be obtained at the same drive level by optimum tuning of the middle cavity. Furthermore, the increase in power output over the no-drive case disappears as first-cavity drive power is reduced to the level where maximum output power occurs. At this drive level the effect of middle-cavity drive is apparent only in the unfavorable phase, when it has the effect of reducing output power.

A review of the parameters of the experiment seems in order. Synchronously tuned, the SAS-61 klystron used in this study had a maximum power output of 7.2 kw with 5 w drive at the first cavity and no power applied to the middle cavity. The tube was rated for a maximum power input of 30 w. Measurements were made with peak input powers into the first cavity of up to 100 w, and with the middle cavity up-tuned for maximum output at 10 w, 20 w, 30 w, and 50 w. Observations were also made of the behavior of the tube with middle-cavity drive when the drive at the first cavity was below saturation as the cavity was then tuned. Under these conditions the power output leveled off, and the behavior of the tube can best be described as that of a two-cavity klystron with its gain increased slightly by the initial modulation impressed upon the beam by the first cavity.

THEORETICAL STUDY

The SAS-61 tube has an oxide-coated unipotential cathode, gridded gaps, and an electron beam focused by space charge. There is no magnetic

focusing, and the tube is designed for pulse operation at a maximum pulse width of 10 μsec. Since the nominal perveance of this tube is relatively high, there is a considerable space-charge debunching resulting in variation of the beam diameter as the beam passes from the cathode to the anode. The tuning of the three cavities is accomplished by decreasing their longitudinal dimensions, which thus has the effect of changing the length of the gap when the cavity is tuned. It is necessary, therefore, to introduce some radical simplifying assumptions in arriving at a mathematical model that will enable prediction of the response of the device to middle-cavity drive power.

The model chosen to represent the SAS-61 klystron is a three-gap structure through which an infinitely wide electron beam is passed. A sinusoidal voltage applied across the first gap produces space-charge waves in the first drift space. This results in a set of input conditions of velocity and a-c current at the second gap. Voltage across the second gap is produced both by the input a-c beam current and by external drive power at the middle cavity. The total second-gap voltage is combined with second-gap input conditions to determine the exit velocity from the gap. The beam is then considered to behave ballistically in the second drift space. Standard ballistic analysis[3] is used to determine a-c current in the final gap, and thus, to determine output power from the third gap. Thus, the justification of the assumption of linear space-charge waves in the first drift space is based upon the observations shown in Figure 7. For a range of input powers exceeding those used in experimental measurements, the two-cavity klystron consisting of the first cavity, first drift space, and the second cavity performs as a linear amplifier. This model does not represent a three-cavity klystron over a wide range of variations of α_1, the normalized first-cavity voltage;

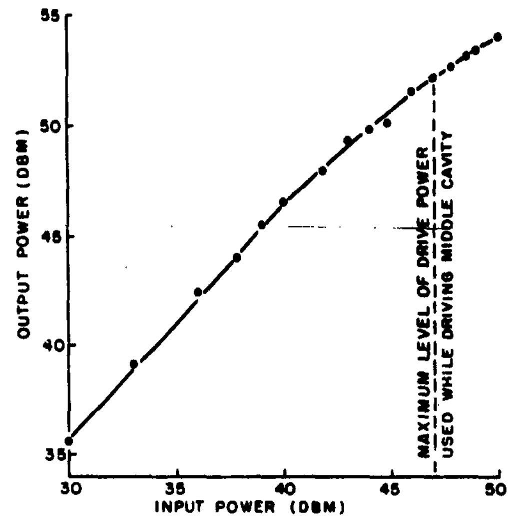

Figure 7. Input Power Gain of SAS-61 Using First and Second Cavities as a Two-Cavity Klystron.

but over the range of operation of this klystron, the first drift space is essentially linear. This is believed to be a valid approximation to the conditions of operation of the typical multiple-cavity klystron. It is emphasized, though, that this condition will not in general be true for a structure in which α_1 varies over a wide range.

The space-charge-wave analysis of the first drift space begins with Maxwell's curl equations, Newton's second law, and the assumption of waves of form $e^{j(\omega t-\gamma z)}$ in a vacuum;

$$\nabla \times \overline{H} = \overline{J} + \frac{\partial \overline{D}}{\partial t} = \overline{J} + \epsilon_o \frac{\partial \overline{E}}{\partial t} , \qquad (1)$$

$$\nabla \times \overline{E} = - \frac{\partial \overline{B}}{\partial t} = -\mu_o \frac{\partial \overline{H}}{\partial t} , \qquad (2)$$

$$m \frac{d}{dt} \overline{u} = -|e| \overline{E} . \qquad (3)$$

It is further assumed that a-c cross products of charge density and velocity are sufficiently small to be neglected, so that

$$\bar{I} = \rho\bar{u} - I_o = -|\rho_o|\bar{u} + \rho_1\bar{u}_o \quad . \tag{4}$$

The Eulerian total time derivative, together with the assumption that the a-c velocity is small compared with the total velocity, results in

$$\frac{d}{dt} = \frac{\partial}{\partial t} + u_{tot}\frac{\partial}{\partial z} \approx j\omega - j\gamma u_o \quad , \tag{5}$$

$$m\left[j\omega - j\gamma u_o\right]\bar{u} = -|e|\bar{E} \quad . \tag{6}$$

The assumption of motion in the z-direction only, i.e., absence of transverse motion, reduces Equation (6) to

$$u = -j\frac{e}{m}\frac{Ez}{u_o}\frac{1}{(\gamma - \beta_e)} \quad . \tag{7}$$

Applying the equation of continuity of charge, and using the resulting statement for a-c current in Equation (4), gives

$$\nabla \cdot i + \frac{\partial \rho}{\partial t} = 0 \quad , \tag{8}$$

where

$$\rho = \frac{\gamma}{\omega} i \quad ;$$

$$i = -|\rho_o|u + \frac{\gamma}{\omega} i\, u_o = -\frac{|\rho_o|\beta_e u}{(\gamma - \beta_e)} \quad , \tag{9}$$

Or, upon substituting the value of u from Equation (7),

$$i = \frac{-j\omega\epsilon_o \beta_\rho^2 E_z}{(\gamma - \beta_e)^2} \quad . \tag{10}$$

Equations (7) and (10) now lend themselves to application to a klystron drift space through the application of the following initial conditions:

$$i_x = 0 = i_y \; , \quad \frac{\partial}{\partial x} = 0 = \frac{\partial}{\partial y} \; , \quad i = i_z \quad . \tag{11}$$

Combination of Equation (1) and the initial conditions (11) leads to

$$i_z + j\omega\epsilon_o E_z = 0 \quad . \tag{12}$$

Substitution of Equation (12) into Equation (10) leads to

$$-j\omega\epsilon_o E_z = \frac{-j\omega\epsilon_o \beta_\rho^2 E_z}{(\gamma - \beta_e)^2} \; ; \quad \gamma = \beta_e \pm \beta_\rho \quad . \tag{13}$$

When an electric field is assumed, which can be described by

$$E_z = Ae^{j(\omega t - \gamma_1 z)} + Be^{j(\omega t - \gamma_2 z)} \quad , \tag{14}$$

and the effect of the first cavity of the model is treated as a velocity jump equal in magnitude to $u_{10}e^{j\omega t}$, one can apply the initial condition,

$$i = 0 \quad \text{when} \quad z = 0 \; , \tag{15}$$

and evaluate and substitute constants A and B to give

$$E_z = u_{10} \frac{m}{e} u_o \beta_\rho \sin(\beta_\rho z) \, e^{j(\omega t - \beta_e z)} , \tag{16}$$

$$i = -j \frac{\beta_e}{\beta_\rho} \left| I_o \right| \frac{u_{10}}{u_o} \sin(\beta_\rho z) \, e^{j(\omega t - \beta_e z)} , \tag{17}$$

$$u = u_{10} \cos \beta_\rho z \, e^{j(\omega t - \beta_e z)} . \tag{18}$$

The initial conditions at the second gap of the model result from the substitution of the length S_1 of the first drift space for z, as follows:

$$i = -j \frac{\beta_e}{\beta_\rho} \left| I_o \right| \frac{u_{10}}{u_o} \sin(\beta_\rho S_1) \, e^{j(\omega t - \beta_e S_1)} , \tag{19}$$

$$u = u_{10} \cos(\beta_\rho S_1) \, e^{j(\omega t - \beta_e S_1)} . \tag{20}$$

These expressions are returned to the form of sinusoids with a driving term equal to $u_{10} \sin\omega t$ by taking the imaginary parts of Equations (19) and (20), resulting in

$$i = A I_o \cos \omega t , \tag{21}$$

$$u = B u_o \sin \omega t , \tag{22}$$

where

$$A = \frac{\beta_e}{\beta_\rho} \frac{u_{10}}{u_o} \sin(\beta_\rho S_1) , \tag{23}$$

$$B = \frac{u_{10}}{u_o} \cos(\beta_\rho S_1) . \tag{24}$$

Having defined the input conditions to the second gap in terms of constants and a parameter (the first-gap voltage) that can be related to power

input to the first gap, we can now assume a sinusoid of voltage at the second gap. In the case of an absence of drive at the middle cavity, this voltage will be simply that induced in the second gap by an a-c beam current. Where there is external drive at the second cavity, the gap voltage resulting from this external drive will add vectorially to the induced voltage. In either case the result is a voltage which can be specified in terms of its magnitude and phase angle, as

$$\overline{V}_2 = |V_2| \cos(\omega t + \phi) \quad , \tag{25}$$

where ϕ is the angle by which V_2 leads i at the center of the second gap. Newton's law is now applied to the motion of electrons in the second gap:

$$\ddot{z} = \frac{e|V_2|}{md_2} \cos(\omega t + \phi) \quad . \tag{26}$$

Integrating this expression between the limits $t_2 - \frac{\theta_2}{2\omega}$ and $t_2 + \frac{\theta_2}{2\omega}$, where t_2 is time referred to the center of the gap, one obtains for exit velocity, the expression,

$$\dot{z} = \frac{e|V_2| M_2}{mu_o} \cos(\omega t_2 + \phi) \quad , \tag{27}$$

$$u_{exit} = u_o + u_1 + \dot{z} = u_o \left[1 + B \sin \omega t_2 + \cos(\omega t_2 + \phi)\right] \quad , \tag{28}$$

where

$$C = \frac{e|V_2| M_2}{mu_o^2} \quad . \tag{29}$$

A useful simplification results from combining terms in Equation (28)

so that

$$u_{exit} = u_o \left[1 + D \sin(\omega t_2 + \gamma)\right] , \tag{30}$$

where

$$D^2 = B^2 + C^2 - 2BC \cos\phi , \tag{31}$$

$$\gamma = \tan^{-1} \frac{C \cos\phi}{C \sin\phi - B} . \tag{32}$$

The length of the second drift space S_2 can be expressed as a product of exit velocity and time difference as follows:

$$S_2 = u_{exit} (t_3 - t_2) . \tag{33}$$

Solving Equation (33) for t_3 gives

$$t_3 = t_2 + \frac{S_2}{u_{exit}} \approx t_2 + \frac{S_2}{u_o} \left[1 - D \sin(\omega t_2 + \gamma)\right] . \tag{34}$$

The Fourier expansion of the a-c current density in the third gap can be expressed as

$$i_3 = \sum_{n=1}^{\infty} a_n \cos n\omega t_3 + b_n \sin n\omega t_3 , \tag{35}$$

where

$$a_n = \frac{1}{\pi} \int_{-\pi}^{\pi} i_3 \cos n\omega t_3 \, d(\omega t_3) , \tag{36}$$

$$b_n = \frac{1}{\pi} \int_{-\pi}^{\pi} i_3 \sin n\omega t_3 \, d(\omega t_3) \quad . \tag{37}$$

Substituting Equation (34) into (37) and making use of the equation of conservation of charge results in

$$i_3 \, dt_3 = i_2 \, dt_2 \quad ; \tag{38}$$

it then follows that

$$a_1 = \frac{1}{\pi} \int_{-\pi}^{\pi} I_o (1 + A \cos \omega t_2) \cos \left[\omega t_2 + \frac{\omega S_2}{u_o} - \frac{\omega S_2 D}{u_o} \sin(\omega t_2 + \gamma)\right] d\omega t_2 \quad , \tag{39}$$

$$b_1 = \frac{1}{\pi} \int_{-\pi}^{\pi} I_o (1 + A \cos \omega t_2) \sin \left[\omega t_2 + \frac{\omega S_2}{u_o} - \frac{\omega S_2 D}{u_o} \sin(\omega t_2 + \gamma)\right] d\omega t_2 \quad . \tag{40}$$

It should again be noted that the d-c current density, I_o, is a negative number as a result of the flow of conventional current from anode to cathode of the model.

Integrating Equations (39) and (40) by parts and making use of various Bessel function identities, it is possible to express the normalized a-c current in the third gap as

$$\left|\frac{I_3}{I_o}\right| = \left| 2 J_1 \left[\frac{\omega S_2 D}{u_o}\right] \cos\left(\omega t + \gamma - \frac{\omega S_2}{u_o}\right) - A J_2 \left[\frac{\omega S_2 D}{u_o}\right] \cos\left(\omega t - \frac{\omega S_2}{u_o}\right) - A J_o \left[\frac{\omega S_2 D}{u_o}\right] \cos\left(\omega t + \partial\gamma - \frac{\omega S_2}{u_o}\right)\right| \quad , \tag{41}$$

where the J's indicate Bessel functions of the first kind, of orders 0,1,and 2.

It is worth noting that if the first-cavity drive is allowed to go to zero, the vanishing of the corresponding A term in Equation (41) causes the expression to reduce to a first-order Bessel function, while the model reduces to a two-cavity klystron consisting of the second and third cavities and the second drift space. This result is thus in accord with that of Webster[3] for the ballistic analysis of the two-cavity klystron.

Before examining the expression for the normalized output current of the three-cavity klystron further, a possible simplification should be examined. It will be noted that Equation (24) contains a multiplier, cos $\beta_\rho S_1$. In a completely general model of a klystron, this term might be allowed to assume any value between -1 and 1. Variations in thi term, however, will be accompanied by complementary variations in Equation (23), which has a multiplier, sin $\beta_\rho S_1$. To maximize current output at the second gap and thus to maximize induced voltage in the second gap, it would be desirable to have term A_1, i.e., Equation (23), equal to unity. If this were the case, term B, i.e., Equation (24), would be equal to zero. This will be true if the length of the first drift space is one-quarter of a plasma wavelength.. An investigation of the parameters of the SAS-61 klystron as operated in this experiment, assuming a beam diameter equal to the diameter of the grids in the middle cavity, shows the following:

$$V_o = 13 \text{ kv} \ ,$$

$$u_o = 6.76 \times 10^7 \text{m/sec} \ ,$$

$$S_1 = 3.03 \times 10^{-2} \text{m} \ ,$$

$$I_o = -3.18 \text{ a/m}^2 \ ,$$

$$\omega_p = 3.05 \times 10^9 \text{ radians/sec} \ ,$$
$$\beta_p S_1 = 1.37 = 78.5^\circ \ ,$$
$$\cos \beta_p S_1 = 0.199 \ .$$

Since the diameter of the grid in the second cavity is an upper bound for the beam diameter, the value calculated for I_o is a lower bound for the current density I_o. This indicates that the true value of $\cos \beta_p S_1$ is less than 0.199 and justifies neglecting it in the application of this model to the SAS-61 tube. This approximation would be further improved by applying a plasma-frequency reduction factor to ω_p. It then follows that

$$B = 0 \ , \qquad D = C \ , \qquad \gamma = \phi + \frac{\pi}{2} \ ; \tag{42}$$

therefore,

$$\left|\frac{I_3}{I_o}\right| = \left| 2 J_1\left[\frac{\omega S_2 C}{u_o}\right] \cos\left(\omega t + \phi + \frac{\pi}{2} - \frac{\omega S_2}{u_o}\right) - A J_2\left[\frac{\omega S_2 C}{u_o}\right] \cos\left(\omega t - \frac{\omega S_2}{u_o}\right) - A J_o\left[\frac{\omega S_2 C}{u_o}\right] \cos\left(\omega t + 2\phi + \pi - \frac{\omega S_2}{u_o}\right)\right| \ . \tag{43}$$

Substituting values for A and C, and shifting the time reference to eliminate the phase angle resulting from drift time in the second drift space gives

$$\left|\frac{I_3}{I_o}\right| = \left| -2 J_1\left[\frac{\omega S_2 M_2 |V_2|}{2 V_o}\right] \sin(\omega t + \phi) - \frac{\beta_e}{\beta_p}\frac{|V_1|}{2 V_o} J_2\left[\frac{\omega S_2 M_2 |V_2|}{2 V_o}\right] \cos \omega t + \frac{\beta_e}{\beta_p}\frac{|V_1|}{2 V_o} J_o\left[\frac{\omega S_2 M_2 |V_2|}{2 V_o}\right] \cos(\omega t + 2\phi)\right| \ . \tag{44}$$

Equation (45) consists of a number of constants and three parameters, which are related to drive at the first and second cavities and to the tuning of the middle cavity. An additional parameter, the length of the final drift space, was fixed in this experiment, but it can be seen from Equation (45) to have the same effect upon output current as the magnitude of middle-cavity voltage. It is planned to evaluate this expression using both the parameters of the experiment and also the length of the final drift space, and to compare the results thus obtained with the experimental results.

CONCLUSIONS

It is apparent from this experiment that middle-cavity drive power has no effect upon the output of a three-cavity klystron above saturation that could not be achieved equally well or better by optimal uptuning of the middle cavity at a given level of first-cavity drive power. Inspection of any of the experimental curves shows that middle-cavity drive power in the most favorable phase reduces the output or produces a negligible change in the output when first-cavity drive power is at the optimum level. It can be seen that certain conditions produce an increase in output power which is greater than the amount of middle-cavity drive. This effect is most noticeable in the curve for a synchronously tuned middle cavity. With a first-cavity input of thirty watts, the application of one kilowatt at the middle cavity produced an increase in output power of 2.9 kilowatts. If the middle cavity is tuned up in frequency to produce a maximum power output at thirty watts input, however, output power increases to 7.6 kilowatts, as compared with the maximum output power of 6.2 kilowatts achieved with synchronous tuning and with one

kilowatt drive at the middle cavity. The same pattern is evident to a lesser degree in the other experimental curves. In no case does the application of power to the middle cavity produce more output above saturation than optimum uptuning of the middle cavity could produce without the use of any additional power.